



**INSTITUTE OF FUNDAMENTAL TECHNOLOGICAL RESEARCH  
POLISH ACADEMY OF SCIENCES**

Doctoral Dissertation

---

**New formulation of the discrete element  
method with deformable particles**

---

**Nikhil Madan**

Supervisor: Prof. Jerzy Rojek, Ph.D., Dr. Habil., Eng.

Co-supervisor : Szymon Nosewicz, Ph.D., Eng.

Warsaw 2019

## **Acknowledgement**

*I would like to express gratitude to my supervisor, Prof. Jerzy Rojek, for introducing me to the concept of the discrete element modelling and for the significant support he had provided me during the research work. I would also like to extend sincere thanks to my co-supervisor Dr. Szymon Nosewicz for his continuous motivation and immense support in shaping this work in the presented form. I am equally indebted to my colleague Dmytro Lumelskyj for helping me with the FEM simulations.*

## Preamble

The work leading to the this thesis was performed within the activities of project funded by the National Science Centre of Poland, awarded through decision number DEC-2015/19/B/ST8/03983.

Part of the results presented here are published in the following peer reviewed articles:

- N. Madan, J. Rojek, and S. Nosewicz. Convergence and stability analysis of the deformable discrete element method. *International Journal for Numerical Methods in Engineering*, 118(6):320–344, 2019.
- J. Rojek, A. Zubelewicz, N. Madan, and S. Nosewicz. The discrete element method with deformable particles. *International Journal for Numerical Methods in Engineering*, 114(8):828–860, 2018.

## Abstract

Discrete element method (DEM) is a state of the art numerical tool which is widely used in industry and academia alike for investigating the mechanics of particulate and non-particulate materials. Interactions between single particles allow to predict the behaviour of bulk solid at the macroscopic scale. Due to this capability of modelling the movement of individual particles, DEM emerges as a natural tool for evaluating the discontinuous systems. Predominantly in discrete element formulation, particles are treated as rigid and overlap between particles is allowed, assuming it to be equivalent to the particle deformation at the contact. This approach is known as *the soft contact approach*. The particle overlap is used in an appropriate contact model which offers an advantage of obtaining the desired macroscopic behaviour. However, despite using the soft-contact approach, assumed particle rigidity makes the accurate representation of macroscopic properties in DEM a great challenge and even impossible in some cases. For instance, the maximum value of Poisson's ratio that can be obtained with discrete element model is 0.25 for bonded spherical elements and 0.33 for bonded disc elements. This inhibits the accurate simulation of elastic deformation and propagation of elastic waves. Additionally, contacts in DEM are independent which is justifiable for relatively low contact forces, however, in the case of particles subjected to high contact forces it leads to incorrect behaviour of the studied system.

In order to mitigate these limitations, a new formulation of discrete element method namely, deformable discrete element method (DDEM) was proposed which takes an appropriate account of particle deformability. Presented doctoral dissertation investigates the formulation of deformable discrete element method in 2D domain i.e. using disc shaped elements.

The new method introduces the concept of global mode of particle deformation resulting from the particle stress which in turn is induced by the contact forces. Uniform stresses and strains are assumed for each particle and inverse elastic constitutive relationship is used to determine global deformation of particle under stress. The global particle deformation leads to the change of overlap in local deformation zone at the contact and formation of new contacts, which affects the macroscopic response of the particle assembly. In particular, it widens the range of Poisson's ratio that can be reproduced in DEM, which is a key parameter in many modelling cases, such as wave propagation.

An accurate computation of the contact forces in the DDEM formulation requires an iterative solution of the implicit relationship between the contact forces and particle displacements. For preserving the efficiency of discrete element methodology, the new formulation has been adapted to the explicit time integration. It has been shown that DDEM algorithm is conditionally stable and there are two restrictions on its stability. Except

for the limitation of the time step as in the standard DEM, the stability in the DDEM is governed by the convergence criterion of the iterative solution of the contact forces. The convergence and stability limits have been determined analytically and numerically for selected regular and irregular configurations of particles assembly.

In order to study the capabilities of DDEM algorithm with respect to standard DEM, the uniaxial compression of a rectangular specimen characterized by the regular configuration of particles has been simulated. The numerical results have been verified using the finite element method and derived analytical solutions of a quasistatic problem. Next, the DDEM algorithm has been applied to the simulation of a uniaxial compression of a square specimen represented with an irregular configuration of nonuniform size particles. A series of simulations have been performed for different sets of microscopic model parameters. This facilitated the establishment of micro-macro relationships between the DDEM parameters and macroscopic elastic constants, the Poisson's ratio and Young's modulus. These relationships have been compared with those obtained with the standard DEM. It has been confirmed that by taking particle deformation into account, greater flexibility in the representation of macroscopic material behaviour is obtained, which improves the current capabilities of standard DEM. It widens the range of macroscopic elastic properties that can be correctly represented using discrete element framework.

After validating and building profound confidence in the formulation, DDEM is extended to numerical investigations of wave propagation problems in elastic solids discretized with disc elements. A 2D bar configuration has been used to simulate longitudinal and shear wave propagation, triggered by initial displacements of selected particles in longitudinal and transverse directions respectively. Longitudinal to shear wave velocity ratio, which depends on the elastic microscopic model parameters has been compared between standard DEM and DDEM models. This study shows that in the problem area of wave propagation as well e.g. impact loading of civil structures or seismology, the DDEM extends the range of problems that can be modelled using standard DEM.

## *”Nowe sformułowanie metody elementów dyskretnych z odkształcalnymi cząstkami”*

### **Streszczenie**

Metoda elementów dyskretnych (MED) jest nowoczesnym narzędziem numerycznym, szeroko stosowanym zarówno w przemyśle, jak i w środowiskach akademickich, do badania mechaniki materiałów rozdrobionych, jak i ciągłych. W MED oddziaływania na poziomie pojedynczych cząstek umożliwiają modelowanie właściwości ciała w skali makroskopowej. Dzięki możliwości modelowania ruchu pojedynczych cząstek, MED jawi się jako naturalne narzędzie do analizy układów nieciągłych. W większości przypadków w zastosowaniach MED, cząstki są traktowane jako ciała sztywne, pomiędzy którymi dozwolone są pewne penetracje, co odwzorowuje deformację cząstek w strefie kontaktu. Podejście to zwane jest modelem ”miękkiego kontaktu” (ang. the soft contact model). Penetracje pomiędzy cząstkami są uwzględniane w modelu kontaktu. Przyjęcie odpowiedniego modelu kontaktu umożliwia uzyskanie pożądanego zachowania makroskopowego. Ze względu na przyjęte założenie dotyczące sztywności cząstki pomimo zastosowania modelu ”miękkiego kontaktu” dokładne odwzorowanie właściwości makroskopowych stanowi wielkie wyzwanie w modelowaniu dyskretnym, a w pewnych przypadkach jest niemożliwe. Dla przykładu, maksymalna wartość współczynnika Poissona, którą można uzyskać za pomocą modelu elementów dyskretnych wynosi 0.25 oraz 0.33, odpowiednio w modelu kohezyjnych elementów dyskretnych o kształcie kuli (3D) oraz walca (2D). Powyższy efekt prowadzi do uzyskania niezupełnie właściwych wyników numerycznych w modelu odkształcenia sprężystego czy propagacji fal sprężystych. Ponadto, kontakty w MED traktowane są jako niezależne, co jest uzasadnione w przypadku stosunkowo małych sił oddziaływania kontaktowego, natomiast w przypadku cząstek poddanych dużym obciążeniom prowadzi do nieprawidłowego odwzorowania analizowanego układu.

W celu zminimalizowania powyższych ograniczeń zaproponowano nowe sformułowanie metody elementów dyskretnych, zwane metodą odkształcalnych elementów dyskretnych, która uwzględnia odkształcalność cząstek. Niniejsza rozprawa doktorska prezentuje badania właściwości nowego sformułowania dla cząstek w postaci dysków (2D). Nowa metoda opiera się na koncepcji globalnego odkształcenia cząstek (elementów dyskretnych) wynikającego z naprężeń generowanych przez siły kontaktowe. Sformułowanie odkształcalnych elementów dyskretnych zakłada jednorodne naprężenie i odkształcenie cząstki. Globalne odkształcenie cząstki wyznacza się z odwrotnej zależności konstytutywnej. Odkształcenie to uwzględnia się w analizie kontaktu. Ma ono wpływ na penetrację między cząstkami (zmiany w lokalnej strefie odkształcenia w miejscu kontaktu) oraz prowadzi do tworzenia się nowych kontaktów. Zastosowanie nowego podejścia poszerza zakres współczynnika Poissona, który można odtworzyć w MED, co stanowi główny czynnik problemów w wielu modelowanych przypadkach, np. w propagacji fal. Do-

kładne obliczenie sił kontaktowych w sformułowaniu metody odkształcalnych elementów dyskretnych wymaga zastosowania niejawnego rozwiązania iteracyjnego niejawnej zależności między siłami kontaktowymi a przemieszczeniem cząstki. Dla zachowania odpowiedniej wydajności obliczeniowej nowe podejście zostało dostosowane do jawnego schematu całkowania. W rozprawie doktorskiej wykazano, że algorytm metody odkształcalnych elementów dyskretnych jest warunkowo stabilny oraz wskazano dwa ograniczenia jego stabilności. Poza ograniczeniem dotyczącym kroku czasowego - jak w standardowym podejściu MED - stabilność w nowej metodzie jest określona poprzez kryterium zbieżności rozwiązania iteracyjnego dla sił kontaktowych. Dla wybranych regularnych i nieregularnych konfiguracji ułożenia elementów dyskretnych zostały wyznaczone oraz zbadane analitycznie i numerycznie granice zbieżności i stabilności rozwiązania.

W celu porównania właściwości nowego algorytmu metody odkształcalnych elementów dyskretnych w odniesieniu do standardowego podejścia MED, przeprowadzono szereg symulacji jednoosiowego ściskania prostokątnych próbek charakteryzujących się regularną konfiguracją ułożenia cząstek. Wyniki numeryczne zostały zweryfikowane za pomocą metody elementów skończonych oraz wyprowadzonego analitycznie rozwiązania problemu quasistatycznego. Podobną analizę numeryczną zastosowano w przypadku symulacji jednoosiowego ściskania kwadratowej próbki o nieregularnej konfiguracji ułożenia cząstek. Przeprowadzono szereg symulacji dla różnych kombinacji parametrów mikroskopowych w celu wyznaczenia zależności pomiędzy wielkościami mikroskopowymi modelu oraz sprężystymi właściwościami makroskopowymi - współczynnikiem Poissona i modułem Younga. Relacje te porównano z analogicznymi wynikami uzyskanymi za pomocą standardowego podejścia MED. Potwierdzono, że dzięki nowemu sformułowaniu wprowadzającemu globalną deformację cząstek uzyskano większą elastyczność w odwzorowaniu makroskopowego zachowania materiału. Poszerzony zostaje zakres makroskopowych właściwości sprężystych, które mogą być uzyskane w ramach modelowania elementami dyskretnymi.

Po dogłębnej analizie oraz weryfikacji, nowe podejście MED zostało zastosowane do badań numerycznych nad propagacją fal w sprężystym ośrodku w kształcie pręta składającego się z dwuwymiarowych dysków. Przeprowadzono symulacje propagacji fal podłużnych oraz poprzecznych generowanych poprzez początkowe przemieszczenia wybranych cząstek, odpowiednio w kierunku wzdłużnym i poprzecznym. W ramach badań numerycznych porównano uzyskany ze standardowego oraz nowego modelu MED stosunek prędkości fali podłużnej do poprzecznej w funkcji mikroskopowych parametrów sprężystych. Powyższa analiza pokazała, że w zagadnieniu dotyczącym propagacji fal, jak również w innych aplikacjach, np. w inżynierii lądowej czy sejsmologii, metoda odkształcalnych elementów dyskretnych zwiększa obszar zagadnień, które można modelować za pomocą standardowego podejścia MED.

# Contents

<b>1</b>	<b>Introduction</b>	<b>13</b>
1.1	Background and motivation . . . . .	13
1.2	State of the art review . . . . .	16
1.3	Objectives and scope of the thesis . . . . .	24
1.4	Outline of the thesis . . . . .	26
<b>2</b>	<b>Formulation of the deformable discrete element model</b>	<b>27</b>
2.1	Standard framework of the discrete element method . . . . .	28
2.1.1	Equations of motion . . . . .	28
2.1.2	Time integration scheme . . . . .	29
2.1.3	Contact modelling . . . . .	31
2.2	Idea and basic assumptions of the deformable discrete element method . . . . .	34
2.3	Evaluation of particles stresses . . . . .	35
2.4	Evaluation of particle strains . . . . .	36
2.5	Particle global deformation mode . . . . .	37
2.6	Contact detection and contact force evaluation . . . . .	38
2.7	Energy balance considerations . . . . .	39
2.8	Theoretical analysis of DDEM model . . . . .	41
2.9	FEM analysis of two particle DDEM model . . . . .	43
<b>3</b>	<b>Convergence and stability analysis of the deformable discrete element model</b>	<b>47</b>
3.1	Implicit relationship for the contact forces in DDEM . . . . .	48
3.2	Iterative procedure of the DDEM . . . . .	48
3.3	Explicit solution algorithm of the DDEM . . . . .	50
3.4	Infinite row of particles . . . . .	51
3.5	Simple cubic configuration . . . . .	56
3.6	A hexagonal closed packing configuration . . . . .	63

---

<b>4</b>	<b>Micro-macro relationships for the deformable discrete element model</b>	<b>73</b>
4.1	Macroscopic stress and strain tensor . . . . .	74
4.2	Dimensionless constitutive relationships . . . . .	75
4.3	Macroscopic constitutive parameters based on the Voigt hypothesis . . . . .	76
4.4	Micro-macro relationships for DDEM model with regular configuration . . . . .	76
4.5	Micro-macro relationships for DDEM model with irregular configuration . . . . .	86
<b>5</b>	<b>Simulation of wave propagation using DDEM model</b>	<b>100</b>
5.1	Fundamentals of wave propagation modelling . . . . .	100
5.2	Numerical example . . . . .	103
<b>6</b>	<b>Concluding remarks</b>	<b>111</b>
6.1	Summary . . . . .	111
6.2	Original contributions of the thesis . . . . .	113
6.3	Suggested future work . . . . .	114
	<b>Bibliography</b>	<b>115</b>

## List of Symbols

- $\mathbf{B}$  : iteration matrix
- $c_n, c_t$  : normal, tangential viscosity (damping) coefficient
- $c_{cr}$  : critical damping for the system of two rigid bodies
- $d_{ij}$  : distance between the particle centres
- $\mathbf{D}_p$  : elastic compliance tensor
- $\tilde{\mathbf{D}}_p$  : elastic compliance matrix
- $e$  : porosity
- $E$  : macroscopic Young's modulus
- $E_p$  : Young's modulus of the particle material
- $\mathbf{f}_i, f$  : resultant force
- $\mathbf{f}_{ij}^c$  : contact force between discrete elements  $i$  and  $j$
- $(\mathbf{f}_n)_{ij}, f_n$  : normal contact force
- $f_n^d$  : viscous (damping) component of the normal contact force
- $f_n^e$  : elastic component of the normal contact force
- $(\mathbf{f}_t)_{ij}, f_t$  : tangential contact force of discrete element
- $\mathbf{F}_i^{\text{ext}}$  : external load applied to the  $i$ -th discrete element
- $\mathbf{F}_i^{\text{damp}}$  : external damping applied to the  $i$ -th discrete element
- $G$  : shear modulus
- $g$  : gap between undeformed particles
- $g^0$  : initial gap between particles
- $g_{max}^0$  : tolerance in the contact verification
- $h$  : overlap between undeformed particles
- $h^0$  : initial overlap between particles
- $h_c$  : overlap between deformed particles
- $h_p$  : deflection of a particle
- $J_{i,j}$  : moment of inertia
- $k_n$  : normal contact stiffness
- $k_n^{\text{eff}}$  : effective normal stiffness
- $k_t$  : tangential contact stiffness
- $\Delta L$  : length change
- $L_0$  : initial length
- $\mathbf{L}^c$  : branch vector
- $m_i$  : mass of the  $i$ -th particle
- $\mathbf{n}$  : normal unit vector
- $n_i^c$  : number of elements being in contact with the  $i$ -th discrete element

- $N_c$  : number of contacts in the particle assembly  
 $N_p$  : number of particles in the particle assembly  
 $R_i$  : radius of  $i$ -th particle  
 $\bar{R}$  : average particle radius in the discrete sample  
 $\mathbf{s}_{ij}^c$  : vector connecting particle centres with contact points  
 $t$  : time  
 $\Delta t$  : time increment (time step)  
 $\Delta t_{cr}$  : critical time step  
 $\mathbf{T}_i$  : resultant moment about the central axes  
 $\mathbf{T}_i^{\text{ext}}$  : external moment applied to the  $i$ -th element  
 $\mathbf{T}_i^{\text{damp}}$  : external damping moment applied to the  $i$ -th element  
 $\mathbf{u}_i, u$  : displacement of a discrete element  
 $\dot{\mathbf{u}}_i, \dot{u}$  : velocity of a discrete element  
 $u_{rn}^e$  : elastic part of the normal relative displacement  
 $u_{rn}^0$  : initial penetration of two particles  
 $u_{rT}$  : relative tangential displacement  
 $\mathbf{u}(\mathbf{x})$  : displacement field of the particle  
 $\mathbf{v}_r$  : relative velocity between two discrete elements  
 $v_{rn}$  : normal relative velocity  
 $v_{rn}^e$  : elastic part of the normal relative velocity  
 $v_{rn}^v$  : viscous part of the normal relative velocity  
 $v_{rT}$  : relative tangential velocity  
 $V$  : bulk volume  
 $\Delta V$  : change of volume  
 $c_L$  : velocity of a longitudinal wave  
 $V_p$  : discrete element volume  
 $c_T$  : velocity of a shear wave  
 $\mathbf{x}_p^{(i)}$  : centroid of a particle  
 $\mathbf{x}$  : inertial coordinate frame  
 $Z$  : coordination number  
 $\alpha^t$  : non-viscous damping factor for translation  
 $\alpha^r$  : non-viscous damping factor for rotation  
 $\alpha$  : safety factor related to the critical time step  
 $\epsilon_p$  : uniform particle strain  
 $\nu$  : macroscopic Poisson's ratio  
 $\nu_p$  : Poisson's ratio of the particle material  
 $\xi$  : fraction of the critical damping (damping ratio)  
 $\phi_n, \phi_t$  : interface strength, normal and tangential

- $\mu$  : Coulomb friction coefficient  
 $\rho_p$  : density of particle material  
 $\bar{\rho}$  : average bulk density  
 $\rho(\mathbf{A})$  : spectral radius of any matrix  $\mathbf{A}$   
 $\sigma_p$  : total average stress in a particle  
 $\omega$  : angular velocity  
 $\otimes$  : outer tensor product

# Chapter 1

## Introduction

### 1.1 Background and motivation

The discrete element method (DEM) belongs to a class of numerical techniques used for studying discontinuous problems of mechanics of materials [121]. It was introduced in the 1970–s and 80–s in the classical works by Cundall [18, 27], Zubelewicz and Mróz [164] and Walton [150, 151]. It was further developed by Williams et al. [155], Bardet and Proubet [5], Moreau [97] and many others. Over the years, DEM has emerged as a robust numerical framework for investigations of scientific and industrial problems involving various materials like soils [113, 153], powders [90], and metals [38], in areas such as agriculture [51, 154], pharmaceuticals [67, 69] and even space [74, 159]. DEM has seen a surge in its popularity (cf. Fig. 1.1) due to an increasing impetus of physically based material modelling and tremendous rise in available computational capability of the hardware and software.

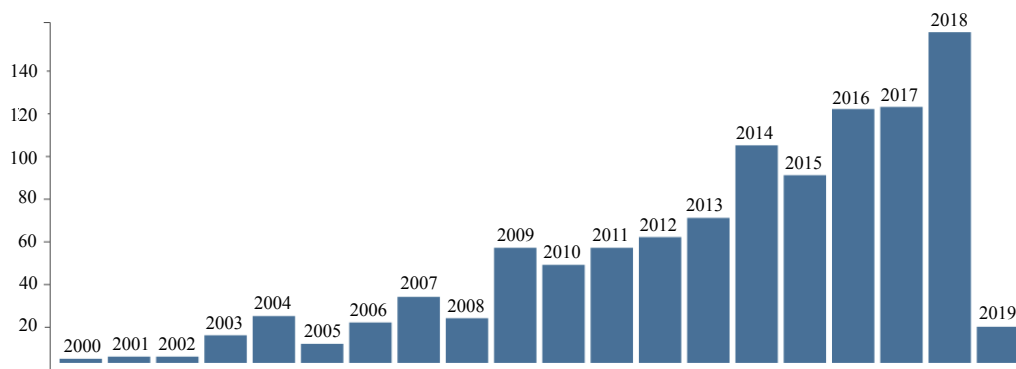


**Figure 1.1.** Total number of articles published on DEM over a span of years 2000 - 2019 (as of January), indexed in Web of Science Core Collection. Keyword: "discrete" + "element" + "method", document types: article, Web of Science categories: Mechanics.

The ability of discrete models to take into account the discontinuities, defects and grain structure has allowed simulating various physical phenomena using DEM, such as granular flows [4, 17, 136], rock fracture [115] and rock burst [164]. DEM has also been adopted for thermal and thermomechanical processes [36], multiphysics problems like coupling DEM with FEM [126], DEM with SPH [119] and DEM with CFD [160]. Special models have also been developed for simulating powder metallurgy processes [76, 86, 91, 106].

Discontinuities of a system are embraced within the discrete element framework by representing the material as a large assembly of particles (discrete elements) interacting with one another by contact cf. Fig.1.2. Although these discrete elements can be of arbitrary shape [23, 129, 140], spherical particles are often a preferable choice [4, 113, 153] because of the simplicity of the formulation and the computational efficiency of contact detection algorithms for spherical objects.

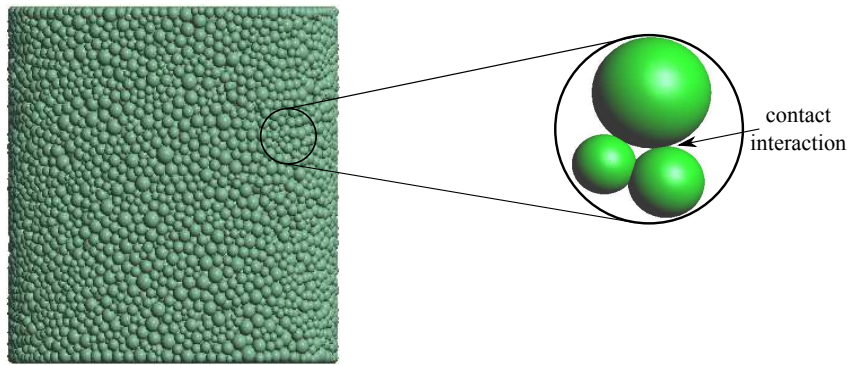


**Figure 1.2.** Assembly of spherical particles in a DEM model with contact interaction details shown in the inset.

It is worth highlighting here that in the DEM, it is the complex cumulative response of the aggregate [75] which determines the macroscopic material properties. It significantly depends on the discrete element assembly characteristics and on the choice of the interparticle contact model [123]. An interparticle contact in the DEM is primarily treated in two different approaches, the soft-contact approach [21, 27, 115] and the hard-contact concept [45, 50, 118]. In the soft-contact formulation, a small overlap of the particles is allowed which is considered as equivalent to the particle deformation at the contact point. The particles are treated as pseudo-rigid bodies with deformation concentrated at the contact points. The contact between the particles is assumed to last much longer than the time step, and the contact force evolution is analysed. In the hard-contact approach, particle penetration is not allowed. The change of the particle momentum due to a collision is determined. The collision time is assumed to be very short and therefore it can be neglected. The contact force variation is not analysed. In the present work, the soft-

contact approach is used. This approach allows to adopt a suitable contact model and thus obtain a required macroscopic behaviour. Contact models for loose and cohesive granular materials are reviewed in depth by Luding in [83] and [84], respectively.

Despite its versatility in simulating a wide variety of engineering problems, an appropriate representation of macroscopic properties in DEM is still a challenge [63]. Some of its major limitations are due to the assumption of the rigidity of discrete elements. Even the soft contact approach is sometimes not sufficient to produce a required deformation behaviour [111]. One of the known drawbacks of the DEM is the incomplete representation of macroscopic properties. For example, in the discrete element models developed for bonded particles (or equivalent lattice models) one cannot obtain the Poisson's ratio greater than 0.25 (0.33 in 2D DEM models) [8], which is also confirmed numerically [78] as shown in Fig. (1.3).

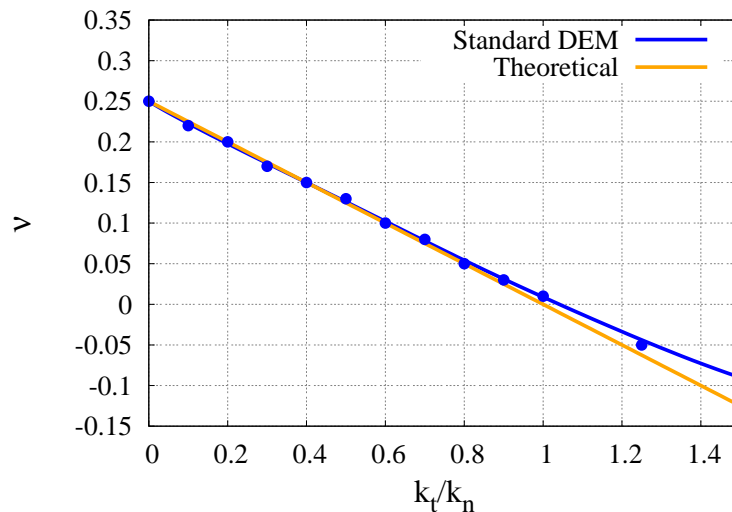


**Figure 1.3.** Limit of the Poisson's ratio in DEM and its numerical verification.

With the unrealistic value of the Poisson's ratio, physical phenomena such as elastic deformation and elastic waves cannot be reproduced accurately. Another troublesome simplification is that the contacts are independent of each other. This assumption is justifiable when the particles are rigid enough such that their deformation is neglected. However, there are applications such as powder compaction where this simplification leads to an erroneous behaviour of such particulate systems at higher relative density [47].

The aforementioned drawbacks can be effectively mitigated in principle if a proper account of element deformations could be taken into consideration. The element deformation will lead to interdependent contact interactions and formation of new contacts. As a result, the macroscopic response of the aggregate will change and the current capabilities of DEM can be enhanced.

## 1.2 State of the art review

The numerical analysis of the engineering problems often require the development of a mathematical model which can most adequately represent the physical aspects of the problem at hand. For some problems, researchers have used the so-called "divide and conquer" strategy, where the model is assumed to consist of the finite number of well-defined elements such that an independent mathematical treatment of each element is possible. The global behaviour of such a system is then evaluated using precise inter-relations between the individual elements. Beams structure is a classic example of such an approach and such a system is known as discrete or discontinuous.

On the other side, some problems instead are comprehensible if treated using the mathematical assumption of an *infinitesimal element*, theoretically implying that an infinite number of smaller elements are used to define a system. Such systems possess infinite degrees of freedom and are termed as continuous. These problems are solved numerically by dividing the systems into sub-domains which must satisfy the governing differential equations and the condition of continuity at the interfaces. In this way, an approximate solution for a continuous system with infinite degrees of freedom is obtained using elements with finite degrees of freedom [61]. It must be noted though that the notion of continuity referred here is a macroscopic concept. It means that if seen from a macroscopic level, there are effectively no voids between any two material points in the problem domain. It is in this context, that systems described earlier are termed as discrete or discontinuous. Currently, the Finite Element Method (FEM) and the Discrete Element Method (DEM) are amongst the main methods for continuum and discontinuum approach, respectively.

Both continuous and discrete numerical methods offer their own advantages and pose some limitations. Standard continuous models, for instance, are not suitable for the problems in which small scale physical processes occur. For modelling the dynamics of processes occurring on a small scale, the discrete models appear to be natural modelling tools. The major drawback of continuous methods emerges for the problems involving strain localization, faults and crack propagation, since the problems in which material weakening occurs, the problem becomes ill-posed and certain regularization in the model becomes essential [120]. Despite regularization, continuous models lack the ability to adequately model non-linear deformations and local yielding. Discrete methods on the other hand can deal with such problems by the very nature in which they are formulated.

However, discontinuous models usually lead to large computational power requirements. High computational cost restricts the use of such models for simpler industrial problems, however with recent advances in the availability of affordable computational resources, this scenario is changing rapidly. Another drawback of discontinuous models is the simplified particle shapes used typically which in a way limits the possibilities

to obtain accurate solutions. Despite such shortcomings, DEM still appears to be most promising numerical tools specially for the problems involving large shear.

Historically, the DEM approaches are found to be rooted within the disciplines of rock and soil mechanics from which the concepts for motion and deformation of block/particles emerged [10, 19, 21, 24, 30]. The discrete fracture network (DFN) approaches which were mainly used to model the flow and transport in fractured rocks led to the development of DEM models for coupled problems later. The use of general principles of the continuum mechanics and numerical framework of the finite element method (FEM) [162] was a common feature of all the theories mentioned above, which are some of the earliest original developments in this scientific domain.

The original work on DEM was presented by Cundall and Strack in a series of papers [26–29]. In their work, Cundall and Strack [27] devised the term *distinct element method* for a specific case of DEM, where contacts are deformable and the motion of circular and rigid particles is resolved using explicit, time domain solution. The numerical implementation of the algorithm of *distinct element method* led to computer program BALL, which was capable of simulating the aggregate response of two dimensional particles. The validity of the method and computer code BALL was demonstrated by comparing simulation results with the results of photoelastic experiments conducted on the assembly of discs. Subsequent extension of the code to 3 dimensional spherical particles [28] led to the code named, TRUBAL. BALL and TRUBAL were the main numerical tools used in the material modeling post 1980's for investigating the features of the method, performance of the underlying algorithm and fundamentals of macroscopic response based on microscopic behaviour, in works such as Walton [150, 151], Thornton and Barnes [142] and Ng [102].

The study of micromechanical aspects of the granular systems emerged as a major research theme in 1980's and early 1990's. Key developments in this direction were made by Rothenburg [128], where idealized granular assemblies of discs and spheres were studied in static equilibrium under external loads. The macroscopic behaviour of idealized bonded granular materials was described by elastic parameters, formulated in terms of microstructural parameters. Thornton and Barnes [142] examined the relationship between the microstructure and the stress tensor for a random assembly of discs with different sizes. Micromechanical analysis of the assembly of discs for a range of diameters with linear contact interactions was presented by Bathurst and Rothenburg in [8]. Whereas in [6], Bathurst and Rothenburg presented key theoretical developments in linking the characteristics of fabric anisotropy to the stress through so-called stress-force-fabric relationship.

By the late 1980's and throughout 1990's DEM achieved widespread use in research of granular materials. This rapid development resulted in a number of new DEM codes

for simulating material behaviour of granular systems comprising 2D elements of different shapes such as circular, elliptical or polygonal. The corresponding 3D element shapes included spheres, ellipsoids and polyhedrons. Some of the examples for such tools may include, DISC by Bathurst and Rothenburg [7], MASOM by Isaa and Nelson [54], SKRUBAL by Trent and Margolin [145], ELLIPSE2 by Ng and Lin [103], ELLIPSE3 by Lin and Ng [80], DEFORM by Saltzer [134], POLY by Mirghasemi et al. [95] etc. Despite the rapid advancements in the DEM research as described above, the high cost and limited availability of computational resources restrained the use of the developed programs for simulation of a few hundred particles only. In order to overcome this limitation, the idea of using parallel computing to solve problems of practical nature could be traced back as early as late 1990's in the work by Kuraoka and Bosscher [77] where a fully parallelized DEM scheme was proposed based on TRUBAL. For simulation of 400 balls, a 900 percent speed up was reported using 16 processor parallel computer. Nowadays, industrial scale problems with multi-million particles can be simulated effectively within a reasonable amount of time and decent computational cost [65].

The abundance of granular material encountered in the engineering problems has resulted in the application of DEM to many different areas such as material processing [40], agriculture [68], soil mechanics [52] and geotechnical [92] engineering etc. The DEM codes developed in earlier days were usually focused on some specific problem area. For instance, the commercial codes UDEC [20] and 3DEC [22, 46] released first in 1980's by Itasca consulting group are specifically oriented towards rock engineering problems. However, the widespread application of DEM led to the development of more general purpose DEM tools, which are available commercially, non-commercially and in open-source domain. At present, the most popular DEM based commercial software products are PFC [55] from Itasca consulting group, EDEM [34] from DEM solution Ltd. and Rocky DEM [31] from ESSS Company. Other open source and non-commercial DEM software packages include YADE [148], MercuryDPM [94], LIGGGHTS [116] and DEMpack [32].

A general DEM model should be able to simulate the physical behaviour of a discrete assembly comprised of arbitrarily shaped particles. However, most of the research efforts in DEM employ circular discs and spheres due to the large savings in computational cost associated with contact detection for a geometry with a single defining parameter, radius. Consequently, a large number of particles can be simulated for a given amount of computational resources with discs and spherical shaped elements. It must be remarked though, that discs and spheres tend to rotate and roll easily and may not reflect the realistic behaviour of materials especially in under large shear. To provide an accurate representation of the material behaviour using DEM, more complex shapes such as ellipses [144] and polygons [37, 54, 93] have been used extensively for problems in 2D domain. In 3D

domain, ellipsoids [80], polyhedra [22, 43, 46] and superquadrics [49, 100] have been reported (cf. Figs. 1.4, 1.5). Greater flexibility in the particle characterization in the DEM is introduced with these complex shapes [96, 157]. However, the contact detection in complex geometries such as polygons and polyhedrons is quite challenging and evaluating forces becomes difficult in cases such as edge-edge, edge-corner or corner-corner contacts. Extension from 2D to 3D and bonding of particles can also become complicated and computationally expensive [152].

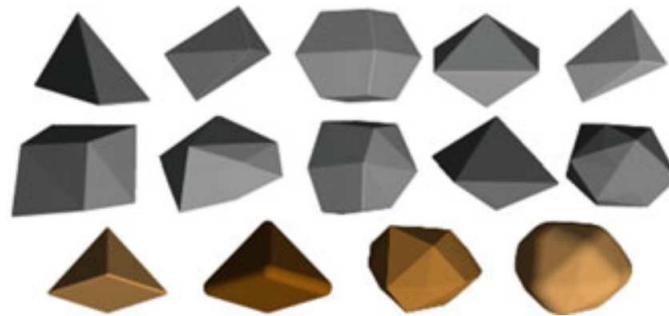


**Figure 1.4.** Basic polyhedra for representing realistic particle shapes in DEM [58].

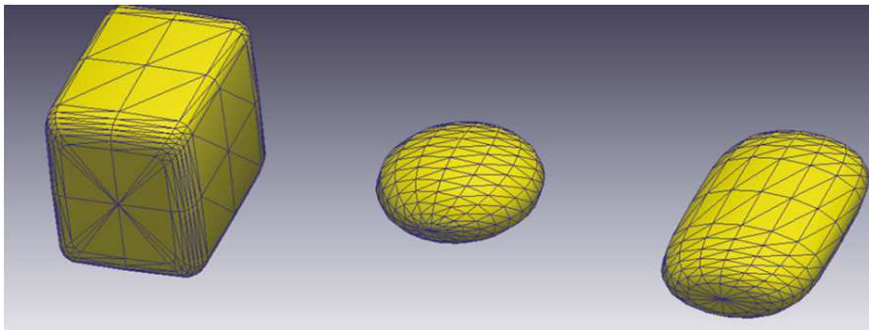


**Figure 1.5.** Superquadric shapes are also used to simulate complex shapes in DEM [114].

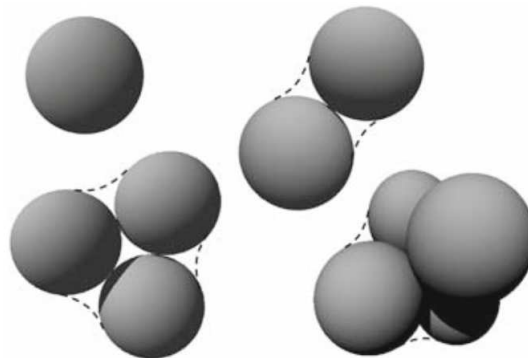


**Figure 1.6.** Clusters of non-penetrating spheres used in DEM simulations for generating complex shapes [133].

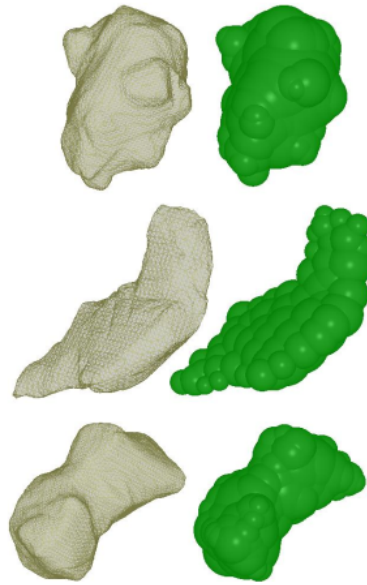


**Figure 1.7.** Coke particles modelled by overlapping spheres for DEM simulation corresponding to 3D scanned shape of particles [89].

As an alternative, the multi-sphere (MS) approach is also used in DEM to represent the shape of real particles (cf. Figs. 1.6, 1.7). The complex shapes of particles in this method are achieved by forming aggregates or clumps of different sized spheres (or discs) bonded together [16, 56, 104, 133]. Even though contact detection in a multi-sphere approach requires much less computational cost w.r.t to polyhedrons, for instance, it becomes difficult to evaluate the contribution of surface roughness.

The shape of particles used in DEM simulation directly determines the packing characteristics of the discrete assembly, which in turn influences the macroscopic response of the system. The parameters like average contacts per element and their orientations are not only dependent on the shape of the particles used but also on the packing algorithm used for given particle shape. The packing algorithms used in DEM currently can be broadly categorized as dynamic methods and geometric methods [57]. The dynamic method basically uses the underlying DEM algorithm itself to trace the particle trajectories and final positions inside a container for instance, which itself might be discretized with bonded discrete elements. Different contact laws can be used for the particle-particle or particle-wall interactions [15, 135]. A variety of dynamic packing algorithms have been reported over the years and use different techniques to generate packings such as gravitational deposition [138], isotropic compaction [139] or even their combination [105]. Flexibility in choosing variety of generation schemes individually or in combination (cf. Fig. 1.8) and selecting different contact laws is a real advantage provided by dynamic packing algorithms. This allows to control the packing properties and generate dense isotropic packings. Nevertheless, drawbacks such as residual overlaps and quite high generation time must be taken into consideration.

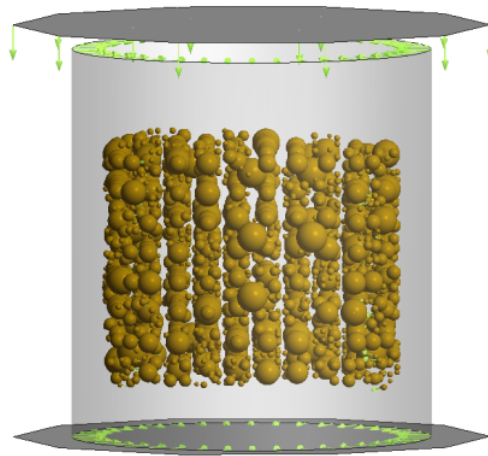


**Figure 1.8.** Example of dynamic packing - combination of gravity deposition and isotropic compression is used in parallel [105].

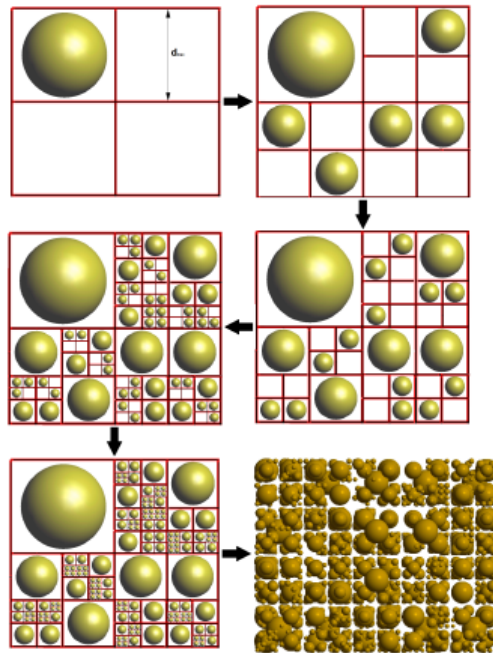


**Figure 1.9.** Example of geometrical packing using sub-grid strategy [105].

The geometrical packing algorithms on the other hand use purely geometric calculations in order to generate a packing, without simulating the dynamics of particle motions, such as shown in Fig. 1.9. Such algorithms generally fall into three basic types [59], namely, ballistic algorithms [147] wherein particles follow a well-defined or definable trajectories to find its static place in the packing. The second type of algorithms belongs to a class known as random placement algorithms, for instance, used by Jodrey and Tory in [62], where particles from a pre-defined size distribution are placed randomly into the container such that no two particles can overlap. After a certain fixed number of iterations, the particle is discarded if the non-overlapping position is not obtained and

the process continues with the next particle. Due to its ease in the implementation, this method is widely used. The third type of algorithms are known as growth algorithms in which initially particles are generated randomly and then allowed to grow until they meet a pre-defined constraint such as inter-particle distances. The lower computation time required in generating dense polydisperse packings is a major advantage of the geometric algorithms over dynamics methods. With an ever increasing demand in simulating problems of granular assemblies at industrial scale, advanced geometrical packing methods using triangulation based have been developed [2, 57]. A good review of recent advances in particle packing algorithms in DEM is published by Recarey et al. [117]. Most of the packing algorithms are typically reported for spheres or spheres aggregates. Only a few algorithms reported are dealing with non-spherical particles for example, in [59], Jia and Williams used digitization of both particle shape and the packing space into pixels, thus overcoming the difficulties suffered by the conventional method. Packing is then achieved by manipulating pixel data on a square lattice, onto which packing space is mapped.

The importance of particle shape and packing algorithms in determining the macroscopic behaviour of a DEM model is reflected by the extensive focus these topics have received over the decades of DEM modelling research. However, the deformability of particles in DEM, which is an equally important aspect for the correct representation of a problem, has received relatively less attention. Deformability of the material inside discrete elements has been taken into account using different ways in earlier works by some of the researchers. Discretization of particles with finite elements [42, 47, 99] presents the simplest method to inculcate deformability in the DEM, however other discretization methods for particle volumes, for instance, the continuum-based Material Point Method (MPM) [101, 149] or the discrete-based Bonded Particle Method (BPM) [33, 101] can equally be employed. On one side, these methods present the flexibility to model particles of arbitrary shapes and different deformation mechanisms assuming the elastic or plastic behaviour of deformable particles with an additional possibility to model the breakage of particles. On the other side, however, the high computational cost associated with these techniques limit their use to a small number of particles.

Adding deformation modes to a rigid motion (translation and rotation) of discrete elements extends an alternative approach to take into account the deformability of discrete elements. The formulation for a discontinuous system of deformable blocks (triangular or quadrilateral prisms) has been put forth by Cundall et al. [25] wherein the block deformation is described by the superposition of independent strain modes. Various solutions to define the deformation of a discrete element has been reviewed by Williams and Mustoe [156] and they proposed the use of eigenmodes obtained from the modal analysis in defining the deformation of the discrete element. Jin et al. [60] also used modal decomposition to define the deformation of a discrete element. Shi [137] described displacement

field within discrete elements in terms of polynomial functions in a method he developed known as discontinuous deformation analysis (DDA). Zubelewicz [163] has developed an original discontinuous model in which the motion of elements comprises element translations and rotations. Each discrete element is described as a rigid core surrounded by a deformable boundary attached to it with a set of springs. The distinct feature of this approach is that though the method belongs to the broad class of discrete element methods, it still retains properties of the finite element method. This method is numerically efficient and allows for a proper description of the elastic and inelastic properties of stressed material.

It must be noted at this point that although the formulations [25, 60, 99, 137, 156] presented earlier deal with deformable elements, they primarily focus on block elements such as polygonal prisms (in 2D) or polyhedra (in 3D). Deformability of cylindrical (in 2D) or spherical (in 3D) discrete elements with the soft contact approach have rather been the focus of only a few works which appeared recently. Multiple-contact discrete element method (MC-DEM) proposed by Brodu et al. [14] is one such work where the interactions between multiple contacts on the same discrete element are taken into account explicitly. The particle deformation under the multi contact forces is evaluated on the basis of different analytical solutions such as an elastic sphere loaded with a point force [12], for the contact between two elastic spheres [44, 161], and for the elastic half-space subjected to a point load [13]. Some experimental adaptation becomes necessary within MC-DEM due to use of the analytical solutions. A similar concept of multiple contacts interactions on individual grains are also proposed in the granular element method (GEM) presented by Karanjgaokar [64]. In GEM, the evaluation of inter-particles forces involves a multi-objective optimization problem. Grain level strain and kinematic data are utilized to determine inter-particle force using two sets of grain level equations viz. conservation of linear and angular momentum, the balance between averaged stress and external (contact) forces within individual grains. These two sets of equations supplemented with constraint equations define a multi-objective optimization problem. A simple approach to modelling deformable particles in the DEM based on the geometrical considerations has been proposed by Haustein et al. [48]. The deformation has been realized by expanding the radius of the spherical particles, depending on their overlap so that the volume of the material is kept constant – the material from the overlapping area has been redistributed on the free surface.

It is worth highlighting that the DDEM formulation investigated in the thesis is original with respect to other formulations discussed above. Even though there are some commonalities which can be identified but there are also comprehensible differences which testify the novelty of the DDEM formulation. In particular it is worth examining the similarities and differences with respect to the MC-DEM proposed by Brodu et al. [14] and

the GEM presented by Karanjgaokar [64]. Similarities between DDEM and MC-DEM:

- contact analysis is conducted by taking into account the overall deformation of the particles due to the contact forces,
- resulting in the evolution of additional contacts and interactions between contact forces acting on each particle, and indirectly between contact forces in the whole particle assembly.

The main difference between DDEM and the MC-DEM:

- in MC-DEM the analytical solutions of similar problems in the theory of elasticity are used in estimating particle deformation,
- whereas, DDEM proposes an evaluation of the particle deformation assuming a uniform strain in the particle induced by the volume averaged stress derived in terms of the contact forces acting on the particle.

Similarities between DDEM and GEM:

- both DDEM and DEM use the volume averaged stress in the particles and the balance of the average stress and contact forces.

The main difference between DDEM and GEM:

- the framework in which the relationship between the average stress and the contact forces are used in the DDEM is entirely different from that of the GEM.
- the problems to be solved and solution algorithms in the DDEM and the GEM which were outlined above are also different.

## 1.3 Objectives and scope of the thesis

The main scientific aim of the proposed thesis is the investigation of deformable discrete element method (DDEM) - a new formulation of DEM which takes into account the particle deformability of the material inside the discrete elements. This work will be limited to 2D domain and focuses on the three specific objectives:

- investigating the potential of DDEM model in improving the current modelling capabilities of standard DEM while preserving its efficiency,
- analysing the convergence and stability of the DDEM formulation,
- verifying the model numerically and analytically by performing the DEM simulations.

The presented research objectives involving numerical and analytical analysis are included in the scope of the thesis are detailed as follows. The dissertation investigates an original formulation of DEM. With an aim to enhance standard DEM's capability in effective representation of elastic deformation of particles, the new formulation introduces the concept of additional (global) deformation mode. The additional (global) deformation in turn changes the particle interaction and consequently the distribution of forces in the discrete element assembly. The contact forces are now evaluated in terms of overlap of the globally deformed particles, which in turn determines the particle deformation, hence implying an implicit relationship for the contact forces. This implicit problem could be solved iteratively, however, in order to retain the advantage of an efficient solution at a single time step associated with the explicit discrete element algorithm, the DDEM algorithm has been adapted to the explicit time integration scheme. Therefore a rigorous analysis of convergence and stability of the DDEM formulation itself has been conducted. The iterative implicit DDEM algorithm as well as its adaptation to the explicit time integration scheme have been presented. A general approach to analyse the convergence of iterative algorithms and the stability of the explicit time integration have been introduced. Analytical evaluation of the convergence criteria for selected problems and numerical studies of the stability of the DDEM solutions have been conducted.

The DDEM formulation has been implemented in DEM/FEM program DEMpack [32] developed and validated by Rojek et al. [123–125]. The theoretical approach and the modified numerical code has been verified with the use of benchmark problems such as unconfined uniaxial compression tests. Furthermore, isotropic biaxial compression and pure shear tests have been carried out for selected cases to check the consistency of the elastic constants obtained in unconfined uniaxial compression tests. The discrete specimens with increasing degree of complexity are used in simulations. The relationships between the constitutive micro- and macroscopic parameters have been further determined and verified in numerical analyses. Additional verification of the implemented solution algorithm has been done using an equivalent finite element model of the discrete sample in some simple cases. Finally, a numerical investigation is conducted to study the potential of DDEM formulation for the correct representation of elastic wave propagation phenomenon in solid materials discretized with bonded disc elements.

The execution of the tasks formulated in the work will allow verification of the following thesis:

**The new formulation of discrete element method with deformable particles is capable of mitigating the limitations of standard formulation and broadening the range of macroscopic properties that can be represented using discrete element method.**

## 1.4 Outline of the thesis

The outline of the thesis is as follows. Chapter 2 presents the main idea behind the DDEM. For completeness, a snapshot version of the formulation for the standard discrete element model has been presented. Next, theoretical developments and the solution algorithm necessary in the implementation of the new formulation i.e. DDEM are discussed. Furthermore, an example of two particles contact model under uniaxial compression has been analysed using DDEM formulation and finite element method (FEM) to support the better understanding of the underlying concept of DDEM.

An elaborate discussion on convergence and stability of the DDEM formulation has been provided in chapter 3. Convergence and stability criterion has been derived analytically and verified numerically for three simple discrete models of equal sized particles – an infinite row, an infinite simple cubic (SC) specimen and an infinite hexagonal close packing (HCP) specimen.

Micro–macro relationships for stresses, strains and constitutive properties in the DEM and DDEM are presented in chapter 4. The macroscopic constitutive parameters based on Voigt hypothesis are presented and energy balance aspects of the problem are discussed. Numerical verification is conducted by applying the DDEM algorithm to the simulation of an unconfined uniaxial compression test, first of a regular rectangular assembly of equal particles. The results of the DDEM simulations for this problem have been verified by simulations of an equivalent FEM model and with an analytical solution. Next, an unconfined uniaxial compression of a square specimen discretized with nonuniform size particles assembled in an irregular configuration has been simulated.

A large number of simulations have been performed taking different sets of model parameters in order to obtain micro-macro relationships which show the range of elastic properties that can be obtained with the DDEM model. Wave propagation characteristics of the DDEM model are studied in chapter 5 in order to show its potential in areas such as seismic studies in geotechnics and impact problems in civil engineering. With chapter 6, this thesis' work is concluded, original elements are discussed and possible future directions have been outlined.

## Chapter 2

# Formulation of the deformable discrete element model

### Introduction

This chapter provides a succinct outline of the underlying concept of the discrete element method with *deformable* particles which is introduced in [127]. This new formulation of the discrete element method is called as the DDEM (deformable discrete element method). The standard formulation of the discrete element method has been outlined first for completeness. Underlying equations of motion are presented, followed by explicit time integration scheme and contact modelling in the standard DEM. A comprehensive description of the DEM can be found in [85, 109, 121]. The idea and basic assumptions of the DDEM has been presented next, followed by the formulation of the additional steps required to evaluate particle deformation within discrete element framework. A better understanding of DDEM concept has been aided by conducting a theoretical analysis of a simple DDEM model. Furthermore, a more precise analysis of particle deformation under uniaxial compression of two particles in contact has been conducted using FEM and results are compared with corresponding DDEM solution.

## 2.1 Standard framework of the discrete element method

### 2.1.1 Equations of motion

In this work, a 2D formulation of the discrete element method is considered employing cylindrical particles (cylindrical discs) following main assumptions of Cundall and Strack [27]. The translational and rotational motion of the discrete elements is described by means of the Newton-Euler equations of rigid body dynamics. For the  $i$ -th element,

$$m_i \ddot{\mathbf{u}}_i = \mathbf{F}_i, \quad (2.1)$$

$$J_i \dot{\boldsymbol{\omega}}_i = \mathbf{T}_i, \quad (2.2)$$

where  $\mathbf{u}_i$  is the element centroid displacement in a fixed (inertial) coordinate frame  $\mathbf{x}$ ,  $\boldsymbol{\omega}_i$  – the angular velocity,  $m_i$  – the element mass,  $J_i$  – the moment of inertia which is given as:

$$J_i = \frac{1}{2} m_i R_i^2, \quad (2.3)$$

for a cylinder and

$$J_i = \frac{2}{5} m_i R_i^2, \quad (2.4)$$

for a sphere.  $\mathbf{F}_i$  is the resultant force and  $\mathbf{T}_i$  is the resultant moment about the central axes. Vectors  $\mathbf{F}_i$  and  $\mathbf{T}_i$  are respectively composed of the forces and moments due to the external load  $\mathbf{F}_i^{\text{ext}}$ , due to the contact interaction with adjacent particles,  $\mathbf{f}_{ij}^c$  and  $\mathbf{t}_{ij}^c$ , and due to the external damping,  $\mathbf{F}_i^{\text{damp}}$  and  $\mathbf{T}_i^{\text{damp}}$ :

$$\mathbf{F}_i = \mathbf{F}_i^{\text{ext}} + \sum_{j=1}^{n_i^c} \mathbf{f}_{ij}^c + \mathbf{F}_i^{\text{damp}}, \quad (2.5)$$

$$\mathbf{T}_i = \sum_{j=1}^{n_i^c} \mathbf{t}_{ij}^c + \sum_{j=1}^{n_i^c} \mathbf{s}_{ij}^c \times \mathbf{f}_{ij}^c + \mathbf{T}_i^{\text{damp}}, \quad (2.6)$$

where  $n_i^c$  is the number of elements in contact with the  $i$ -th discrete element, and  $\mathbf{s}_{ij}^c$  is the vector connecting the centre of mass of the  $i$ -th element with the contact point with the  $j$ -th element (Fig. 2.1). In the present work, only the force-type contact interaction will be considered, resulting in zero values for the interaction moments  $\mathbf{t}_{ij}^c$  of Eq. (2.6). The damping terms  $\mathbf{F}_i^{\text{damp}}$  and  $\mathbf{T}_i^{\text{damp}}$  used in equations (2.5) and (2.6) are of a non-viscous type:

$$\mathbf{F}_i^{\text{damp}} = -\alpha^t \|\mathbf{F}_i^{\text{ext}} + \sum_{j=1}^{n_i^c} \mathbf{f}_{ij}^c\| \frac{\dot{\mathbf{u}}_i}{\|\dot{\mathbf{u}}_i\|}, \quad (2.7)$$

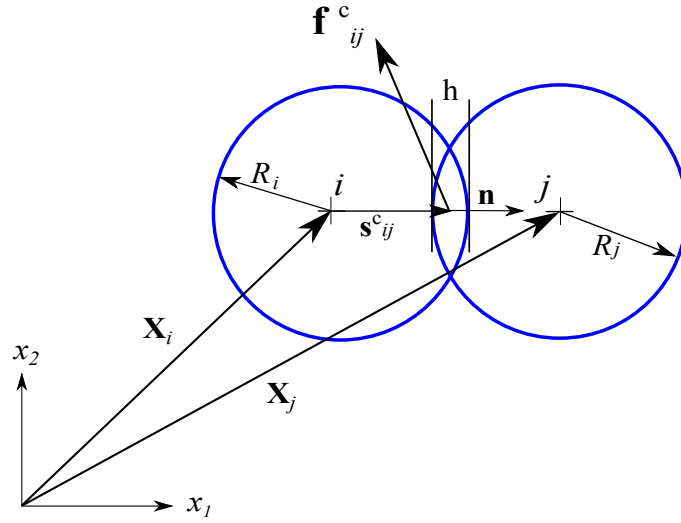


**Figure 2.1.** Definition of the inter-particle interaction.

$$\mathbf{T}_i^{\text{damp}} = -\alpha^r \left\| \sum_{j=1}^{n_i^c} \mathbf{t}_{ij}^c + \sum_{j=1}^{n_i^c} \mathbf{s}_{ij}^c \times \mathbf{f}_{ij}^c \right\| \frac{\boldsymbol{\omega}_i}{\|\boldsymbol{\omega}_i\|}. \quad (2.8)$$

where  $\alpha^t$  and  $\alpha^r$ , are the respective damping factors for translational and rotational motion. The terms given by Eqs. (2.7) and (2.8) represent the so-called background damping working against the existing velocity (linear and angular) with magnitude proportional to the existing force and moment, respectively. An additional damping dependent on the relative velocities at the contact points is included in the contact interaction.

### 2.1.2 Time integration scheme

An explicit central difference scheme is employed to integrate Eqs.(2.1) and (2.2). For translation motion, the time integration operator at the  $n$ -th time step is given as:

$$\ddot{\mathbf{u}}_i^n = \frac{\mathbf{F}_i^n}{m_i}, \quad (2.9)$$

$$\dot{\mathbf{u}}_i^{n+1/2} = \dot{\mathbf{u}}_i^{n-1/2} + \ddot{\mathbf{u}}_i^n \Delta t, \quad (2.10)$$

$$\mathbf{u}_i^{n+1} = \mathbf{u}_i^n + \dot{\mathbf{u}}_i^{n+1/2} \Delta t. \quad (2.11)$$

Similarly, the time integration scheme for the rotational motion is identical to the first two steps given by Eqs. (2.9) and (2.10):

$$\ddot{\boldsymbol{\omega}}_i^n = \frac{\mathbf{T}_i^n}{m_i}, \quad (2.12)$$

$$\dot{\boldsymbol{\omega}}_i^{n+1/2} = \dot{\boldsymbol{\omega}}_i^{n-1/2} + \ddot{\boldsymbol{\omega}}_i^n \Delta t, \quad (2.13)$$

If required the rotational configuration can be determined, however for the disc elements used in this work, the evaluation of rotational configuration is not essential.

The explicit time integration scheme used in DEM imposes a limitation on the time step due to the conditional numerical stability. The time step  $\Delta t$  must not be larger than the critical time step  $\Delta t_{cr}$ ,

$$\Delta t \leq \Delta t_{cr}, \quad (2.14)$$

which is determined by the highest natural frequency of the system,  $\nu_{max}$  as,

$$\Delta t_{cr} = \frac{2}{\nu_{max}}. \quad (2.15)$$

The highest frequency  $\nu_{max}$  can be evaluated by solving the eigenvalue problem defined for the entire system of connected particles, however, this would be computationally expensive. Analogously to the standard simplification proposed for the explicit FEM [11], the maximum frequency of the full system in the DEM can be estimated by natural frequencies of subsets of connected particles surrounding each particle, cf. [110],

$$\nu_{max} \leq \max \nu_{max}^{(i)} \quad (2.16)$$

where  $\nu_{max}^{(i)}$  is the maximum natural frequency of the system of connected particles surrounding the  $i$ -th particle. The problem of the critical time evaluation can be simplified further by considering equivalent single degree mass–spring systems with the natural frequency

$$\nu^{(i)} = \sqrt{\frac{k_{\text{eff}}^{(i)}}{m_i}} \quad (2.17)$$

where  $k_{\text{eff}}^{(i)}$  is the effective stiffness governing the motion of the  $i$ -th particle. Hence, the limit on the time step can be given by

$$\Delta t \leq \min 2 \sqrt{\frac{m_i}{k_{\text{eff}}^{(i)}}} \quad (2.18)$$

The effective stiffness  $k_{\text{eff}}^{(i)}$  depends on the normal and tangential contact stiffnesses, the number of particles connected to the  $i$ -th particle as well as contact directions, cf. [110]. In practice, the time step can be estimated approximately taking, cf. [112]

$$\Delta t \leq \alpha \sqrt{\frac{m_{\min}}{k_{\max}}} \quad (2.19)$$

where  $m_{\min}$  is the minimum mass and  $k_{\max}$  is the largest normal or tangential contact stiffness and  $\alpha$  is the user specified parameter accounting for multiple contacts for each mass. For regular packings of equal particles with the same stiffness for all the contacts the parameter  $\alpha$  can be determined analytically [110]. For irregular packing a safe value of the parameter  $\alpha$  can be based on the results of numerical simulations [112].

### 2.1.3 Contact modelling

The formulation of the contact model employs the decomposition of the contact force between two elements<sup>1</sup>  $\mathbf{f}^c$  into the normal and tangential components,  $\mathbf{f}_n$  and  $\mathbf{f}_t$ , respectively:

$$\mathbf{f}^c = \mathbf{f}_n + \mathbf{f}_t = f_n \mathbf{n} + \mathbf{f}_t, \quad (2.20)$$

where  $\mathbf{n}$  is the unit normal vector at the contact point (Fig. 2.1). The normal and tangential contact forces can be evaluated assuming different models [71, 72]. Granular materials are usually modelled assuming cohesionless frictional contact [39], while rock-like materials, as well as various other materials, require cohesive contact models [84]. The present work has been focused on the elastic behaviour of the materials modelled with bonded particles, therefore a cohesive contact model is presented. Nevertheless, the formulation presented is valid for a cohesionless contact model, as well.

An initial bonding between the neighbouring particles has been assumed as shown in Fig. 2.1. The bonds are established between the particles  $i$  and  $j$  satisfying the condition:

$$g^0 = g(t = 0) = \|\mathbf{x}_j - \mathbf{x}_i\| - R_i - R_j \leq g_{\max}^0 \quad (2.21)$$

where  $R_i$  and  $R_j$  are the particle radii,  $g^0$  is the gap at the contact point at the time  $t = 0$ , and  $g_{\max}^0$  is a tolerance in the contact verification. In the soft contact approach used here, the impenetrability condition is satisfied approximately and a certain overlap between the contact particles  $h$  is allowed such that,

$$h = -g > 0, \quad (2.22)$$

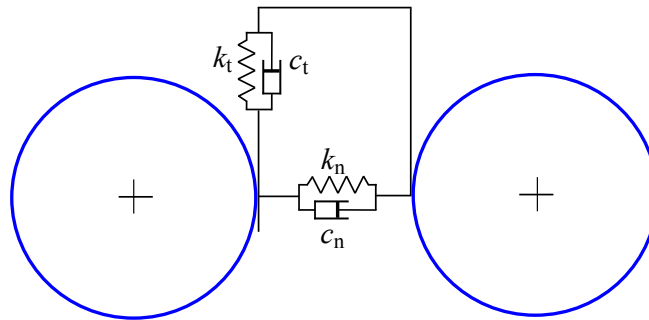


**Figure 2.2.** Rheological scheme of the bonded particle interaction model.

The normal and tangential particle interactions are modelled by linear springs connected in parallel with dashpots (Fig. 2.2) providing an additional mechanism to dissipate contact oscillations. Thus, the normal and tangential contact forces are decomposed into

<sup>1</sup>From this point further on, the indices denoting the elements will be omitted.

the elastic,  $f_{ne}$  and  $\mathbf{f}_{te}$ , and damping parts,  $f_{nd}$  and  $\mathbf{f}_{td}$ , respectively:

$$f_n = f_{ne} + f_{nd} \quad (2.23)$$

$$\mathbf{f}_t = \mathbf{f}_{te} + \mathbf{f}_{td} \quad (2.24)$$

The elastic contact force components are evaluated assuming linear constitutive relationships. The elastic normal force is given by

$$f_{ne} = k_n g \quad \text{if } g < 0, \quad (2.25)$$

or considering Eq. (2.22),

$$f_{ne} = -k_n h, \quad (2.26)$$

where  $k_n$  is the interface stiffness in the normal direction. The tangential elastic force is given by the relationship

$$\mathbf{f}_t = k_t \mathbf{u}_t, \quad (2.27)$$

where  $k_t$  is the interface stiffness in the tangential direction,  $\mathbf{u}_t$  – the relative displacement at the contact point in the tangential direction. The relative tangential displacement  $\mathbf{u}_t$  must be evaluated incrementally, cf. [110]:

$$\mathbf{u}_t = \mathbf{u}_t^{\text{old}} + \Delta \mathbf{u}_t \quad (2.28)$$

where  $\mathbf{u}_t^{\text{old}}$  is the vector of the relative tangential displacement from the previous time step rotated to the present contact plane and  $\Delta \mathbf{u}_t$  is the incremental relative tangential displacement

$$\Delta \mathbf{u}_t = \mathbf{v}_{rt} \Delta t \quad (2.29)$$

with  $\mathbf{v}_t$  being the relative tangential velocity at the contact point determined as

$$\mathbf{v}_{rt} = \mathbf{v}_r^c - v_{rn} \mathbf{n} \quad (2.30)$$

where  $\mathbf{v}_r^c$  is the relative velocity at the contact point and  $v_{rn}$  its projection on the normal direction:

$$v_{rn} = \mathbf{v}_r^c \cdot \mathbf{n} \quad (2.31)$$

The relative velocity at the contact point is evaluated as follows:

$$\mathbf{v}_r^c = (\dot{\mathbf{u}}_j + \boldsymbol{\omega}_j \times \mathbf{s}_{ji}^c) - (\dot{\mathbf{u}}_i + \boldsymbol{\omega}_i \times \mathbf{s}_{ij}^c) \quad (2.32)$$

where  $\dot{\mathbf{u}}_a$  and  $\boldsymbol{\omega}_a$  ( $a = i, j$ ) are the particle translational and angular velocities.

The contact damping forces in the normal and tangential directions are given by

$$f_{nd} = c_n v_{rn} \quad (2.33)$$

$$\mathbf{f}_{td} = c_t \mathbf{v}_{rt} \quad (2.34)$$

respectively, where  $c_n$  and  $c_t$  are the damping coefficients. The damping coefficients,  $c_n$  and  $c_t$ , can be related to the critical damping in the normal and tangential direction,  $c_n^{cr}$  and  $c_t^{cr}$ , by means of certain scaling factors,  $\xi_n$  and  $\xi_t$ :

$$c_n = \xi_n c_n^{cr} \quad (2.35)$$

$$c_t = \xi_t c_t^{cr} \quad (2.36)$$

For the system of two rigid bodies with masses  $m_i$  and  $m_j$ , connected with a spring of the stiffness  $k$ , the critical damping  $c^{cr}$  is given by, cf. [141]

$$c^{cr} = 2\sqrt{\frac{m_i m_j k}{m_i + m_j}} \quad (2.37)$$

By taking  $k = k_n$  or  $k_t$  in Eq. (2.37) the critical damping  $c_n^{cr}$  and  $c_t^{cr}$  is obtained. The critical damping separates the oscillatory (overdamped) and non-oscillatory (underdamped) solutions in the damped mass-spring systems. It ensures the fastest return to equilibrium without oscillations which is important in the solution of quasistatic problems.

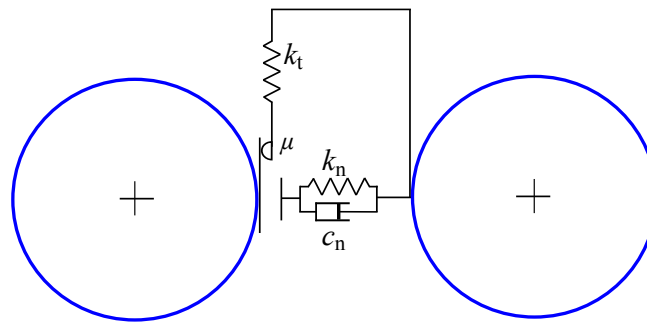


**Figure 2.3.** Rheological scheme of the particle interaction after decohesion.

Cohesive bonds are broken instantaneously when the interface strength is exceeded in the tangential direction by the tangential contact force or in the normal direction by the tensile contact force

$$\|f_n\| \geq \phi_n \quad (2.38)$$

$$\|\mathbf{f}_t\| \geq \phi_t \quad (2.39)$$

where  $\phi_n$  – interface strength in the normal direction,  $\phi_t$  – interface strength in the tangential direction. After decohesion, the contact is treated assuming a standard contact model with Coulomb friction cf. Fig.2.3. The normal contact force can be compressive only ( $f_n \leq 0$ ) and the tangential contact force is limited by  $\mu|f_n|$

$$\|\mathbf{f}_t\| \leq \mu|f_n| \quad (2.40)$$

where  $\mu$  is the Coulomb friction coefficient. The general DEM framework presented here remains equally valid irrespective of rigid or deformable elements. However, some additional steps are required in the DEM algorithm to include deformability of the discrete elements, which is the focus of the following sections.

## 2.2 Idea and basic assumptions of the deformable discrete element method

The new original formulation of DEM in which particles are treated as deformable was introduced by Rojek et al. [127] and is presented here in brief. The new formulation of the discrete element method i.e. DDEM (the deformable discrete element method) is based on the following assumptions [127]:

- The particles are treated as deformable. The particle deformation is composed of the global deformation mode and local deformation modes.
- The global deformation mode of each particle is induced by uniform (homogenous) stresses assumed for the particles. The stresses derived by averaging over the particle volumes in terms of the contact forces acting on each particle are taken as the particle stresses.
- The uniform particle strain is obtained via the inverse constitutive relationship from the uniform averaged particle stress. The linear elastic material model is assumed for the particle global deformation mode.
- The deformed shape (global deformation) of the particle is obtained by integration of the particle strain.
- The local deformation modes are assumed at contact zones and they are represented by the overlaps of the globally deformed particles. The normal contact forces will be determined as functions of the overlaps.

The idea of the DDEM is illustrated with a simple example in Fig. 2.4. Enhancement of the DEM formulation is accomplished by introduction of the additional (global) deformation mode, which in turn changes the particle interaction and the distribution of forces

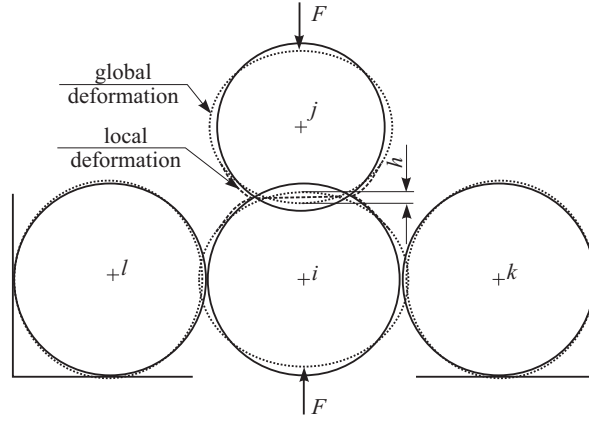


**Figure 2.4.** The idea of the deformable discrete element method [127].

in the discrete element assembly. For example, consider interactions between the particles shown in Fig. 2.4. In the standard DEM formulation, there would be no contact force developing between the particles  $i$  and  $k$  or  $l$  (the circles  $k$  and  $l$  plotted with continuous lines are not in contact with the circle  $i$ ). However, the shape change of the particle  $i$  under compression with forces  $F$  leads to an active contact between the particles  $i$  and  $k$ , and  $i$  and  $l$ . In this way, a nonlocal contact model has been achieved. The contact interaction between the particles  $i$  and  $j$  influences indirectly (through the change of the shape of the particle  $i$ ) the contact between the particle  $i$  and the other particles, and vice versa. As a result, the non-local interactions are expected to affect the macroscopic response of the aggregate, in particular, it should broaden the range of the Poisson's ratio which can be reproduced in the discrete element method. Under the assumptions of the DDEM model listed above, the algorithm of DDEM proceeds as follows.

## 2.3 Evaluation of particles stresses

Particle stresses  $\bar{\sigma}_p$  are derived by averaging over the particle volumes  $V_p$  (Fig. 2.5) in terms of the contact forces  $\mathbf{f}^c$  acting on each particle using the following formula [82]:

$$\bar{\sigma}_p = \frac{1}{V_p} \sum_{c=1}^{n_{pc}} \mathbf{s}^c \otimes \mathbf{f}^c, \quad (2.41)$$

where  $n_{pc}$  is the number of particles being in contact with the  $p$ -th particle,  $\mathbf{s}^c$  – vector connecting the element center with the contact point (see Fig. 2.5),  $\mathbf{f}^c$  – contact force, and the symbol  $\otimes$  denotes the outer (tensor) product. The averaging formula (2.41) should also include reaction forces and other external surface forces, cf. [122]. In the 2D formulation, the stress is represented by the matrix

$$\bar{\sigma}_p = \begin{bmatrix} (\sigma_p)_{xx} & (\sigma_p)_{xy} & 0 \\ (\sigma_p)_{yx} & (\sigma_p)_{yy} & 0 \\ 0 & 0 & (\sigma_p)_{zz} \end{bmatrix} \quad \text{for plane strain,} \quad (2.42)$$

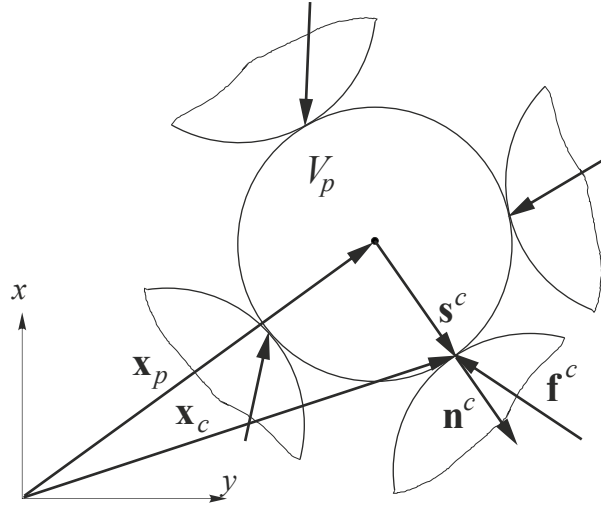


**Figure 2.5.** Vectors used in the particle stress evaluation.

or

$$\bar{\sigma}_p = \begin{bmatrix} (\sigma_p)_{xx} & (\sigma_p)_{xy} \\ (\sigma_p)_{yx} & (\sigma_p)_{yy} \end{bmatrix} \quad \text{for plane stress.} \quad (2.43)$$

It must be noted that the stress tensor given by Eq. (2.41) is derived under the assumption that particle is in equilibrium and the forces acting on it are taken into consideration. However, because this assumption of the equilibrium is usually satisfied only approximately, stress tensor can be unsymmetrical. It can be made symmetric by taking arithmetic mean of the tensor evaluated by Eq.(2.41) and its transpose. The symmetric tensor will be then given as:

$$\sigma_p = \frac{1}{2} (\bar{\sigma}_p + \bar{\sigma}_p^T), \quad (2.44)$$

or

$$(\sigma_p)_{ij} = \frac{1}{2V_p} (s_i^c f_j^c + f_j^c s_i^c). \quad (2.45)$$

## 2.4 Evaluation of particle strains

The uniform particle strain  $\epsilon_p$  is obtained from the uniform averaged particle stress  $\sigma_p$  via the inverse constitutive relationship:

$$\epsilon_p = \mathbf{D}_p : \sigma_p \quad (2.46)$$

where  $\mathbf{D}_p$  is the elastic compliance tensor. In the matrix notation formula (2.46) can be rewritten as

$$\tilde{\epsilon}_p = \tilde{\mathbf{D}}_p \tilde{\sigma}_p \quad (2.47)$$

where, in 2D, the strain and stress tensors are represented by the vectors  $\tilde{\epsilon}_p = [(\epsilon_p)_{xx}, (\epsilon_p)_{yy}, 2(\epsilon_p)_{xy}]^T$ ,  $\tilde{\sigma}_p = [(\sigma_p)_{xx}, (\sigma_p)_{yy}, (\sigma_p)_{xy}]^T$  respectively, and  $\tilde{\mathbf{D}}_p$  is the matrix representation of the elastic compliance tensor. Two dimensional DEM models can

be assumed to represent either plane stress or plane strain conditions [35, 158]. For plane strain conditions, the elastic compliance matrix becomes

$$\tilde{\mathbf{D}}_p = \frac{1 + \nu_p}{E_p} \begin{bmatrix} 1 - \nu_p & -\nu_p & 0 \\ -\nu_p & 1 - \nu_p & 0 \\ 0 & 0 & 2 \end{bmatrix} \quad (2.48)$$

and for plane stress the compliance matrix takes following form,

$$\tilde{\mathbf{D}}_p = \frac{1}{E_p} \begin{bmatrix} 1 & -\nu_p & 0 \\ -\nu_p & 1 & 0 \\ 0 & 0 & 2(1 + \nu_p) \end{bmatrix} \quad (2.49)$$

where  $\nu_p$  is particle Poisson's ratio and  $E_p$  is particle Young's modulus.

## 2.5 Particle global deformation mode

The deformed shape (global deformation) of the particle can be determined using the displacement field  $\mathbf{u}(\mathbf{x})$ , where  $\mathbf{x} \in V_p$ , obtained by integration of the particle strain. The displacement field, however, can be determined up to rigid modes. Assuming zero rotations and fixing zero displacements at the particle centre  $\mathbf{x}_p$  one can get the solution for the displacement of an arbitrary point  $\mathbf{x}$  of the particle as

$$\mathbf{u}(\mathbf{x}) = \boldsymbol{\varepsilon}_p(\mathbf{x} - \mathbf{x}_p) \quad (2.50)$$

where  $\boldsymbol{\varepsilon}_p$  is strain matrix

$$\boldsymbol{\varepsilon}_p = \begin{bmatrix} (\varepsilon_p)_{xx} & (\varepsilon_p)_{xy} \\ (\varepsilon_p)_{yx} & (\varepsilon_p)_{yy} \end{bmatrix} \quad (2.51)$$

The calculations according to Eq. (2.50) can be performed for the contact points, only. Taking  $\mathbf{x} = \mathbf{x}_C$ , see Fig. 2.5,

$$\mathbf{u}_c = \boldsymbol{\varepsilon}_p(\mathbf{x}_c - \mathbf{x}_p) = \boldsymbol{\varepsilon}_p \mathbf{s}^c \quad (2.52)$$

## 2.6 Contact detection and contact force evaluation

The overlap  $h_c$  between the deformed particles  $i$  and  $j$  (Fig. 2.6) can be evaluated as follows:

$$h_c \approx h + \mathbf{u}_c^i \cdot \mathbf{n}_c^i + \mathbf{u}_c^j \cdot \mathbf{n}_c^j \quad (2.53)$$

where the overlap  $h$  between the circular particles in the standard DEM is modified by projecting the vectors of displacements of the contact points of both particles  $\mathbf{u}_c^i$  and  $\mathbf{u}_c^j$ , evaluated according to Eq. (2.52), on the outward normal unit vectors  $\mathbf{n}_c^i$  and  $\mathbf{n}_c^j$  (see Fig. 2.6), having in mind that  $\mathbf{n}_c^i = -\mathbf{n}_c^j = \mathbf{n}_c$ .

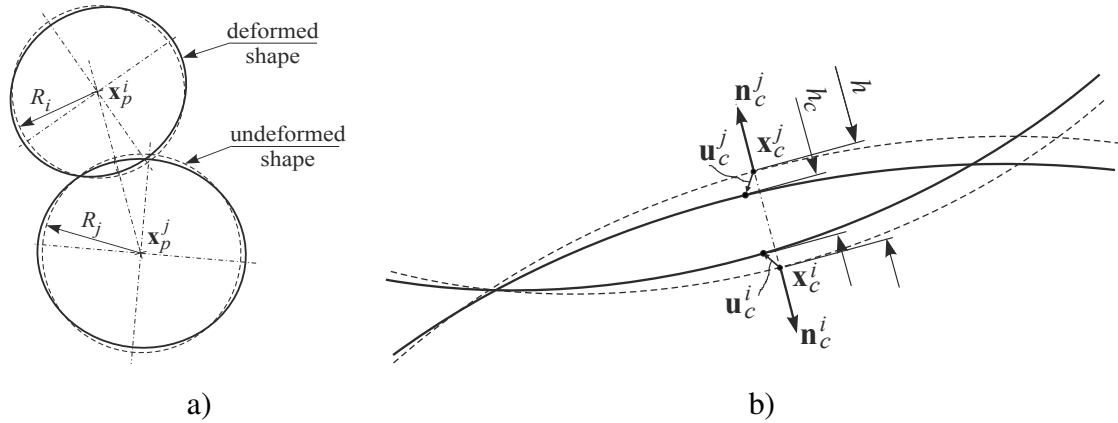


**Figure 2.6.** Contact of two deformable particles a) overview b) detail.

A more exact evaluation of the overlap between deformed particles can be performed using an algorithm to determine the contact between the elliptical bodies, cf. [103, 143]. Here, an approximate formula according to Eq. (2.53) has been used assuming a relatively small deformation of the two particles in contact. Furthermore, it has been assumed that the contact point between the deformed particles is close to the contact point between the undeformed circles and the normal and tangential directions at the contact are unaffected by the deformation.

Now that, the overlap between the deformed particles is evaluated, the normal contact force  $f_n$  can be calculated as:

$$f_n = -k_n h_c, \quad (2.54)$$

where  $k_n$  is the normal contact stiffness. The normal force  $f_n$  combines with the tangential contact force  $f_t$  yielding the total contact force between the considered pair of particles  $\mathbf{f}^c$  cf. Eq. (2.20).

Figure 2.7 shows the flowchart of the DDEM algorithm. The tasks written in bold are either new or extended tasks with respect to the standard DEM algorithm. It must be noted though that the tangential contact force is assumed here to be unaffected by the particle deformation and it is calculated taking any model used in the standard DEM.

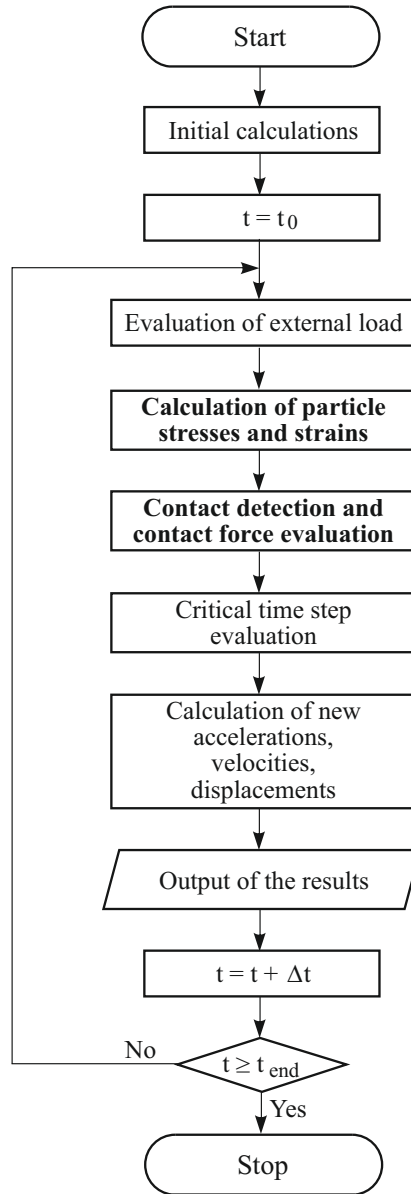


**Figure 2.7.** Flowchart of the DDEM algorithm.

## 2.7 Energy balance considerations

According to the principle of conservation of mechanical energy, the total work done by the external forces  $W_{ext}$  during a certain interval from 0 to  $t$  acting on particles should be equal the change in kinetic energy of the particles  $E_k$ , the strain (elastic) energy  $E_{el}$  of the particle system and the dissipated energy  $E_{diss}$  [146]:

$$W_{ext}^t = \Delta E_k + \Delta E_{el} + E_{diss}. \quad (2.55)$$

The change of the kinetic and elastic energies

$$\Delta E_k = E_k^t - E_k^0, \quad (2.56)$$

$$\Delta E_{el} = E_{el}^t - E_{el}^0, \quad (2.57)$$

are considered with respect to the initial energies  $E_k^0$  and  $E_{el}^0$  due to the initial velocities and initial interparticle interactions, respectively. The kinetic energy of the system of  $N_p$  particles at the time instant  $\tau \in \langle 0, t \rangle$  can be expressed as the sum of the translational and rotational parts [70, 146]:

$$E_k^\tau = \sum_{i=1}^{N_p} \left( \frac{m_i (v_i^\tau)^2}{2} + \frac{J_i (\omega_i^\tau)^2}{2} \right), \quad (2.58)$$

where  $m_i$  is the particle mass,  $J_i$  – the moment of inertia,  $v_i$  and  $\omega_i$  – the translational and rotational particle velocities, respectively. In the standard DEM, the strain energy is equal to the energy stored at the contacts due to the work of the elastic components of the normal and tangential contact forces,  $f_{ne}$  and  $\mathbf{f}_{te}$ , respectively [70]:

$$E_{el}^\tau = \sum_{i=1}^{N_c} \left( \frac{(f_{ne})_i^2}{k_n} + \frac{(\|\mathbf{f}_{te}\|)_i^2}{k_t} \right), \quad (2.59)$$

where  $N_c$  is the number of contacting pairs of particles. The dissipated energy  $E_{diss}$  represents the work of non-conservative forces, the friction and the damping ones.

In the DDEM formulation, the elastic deformation of particles provides a new contribution to the strain energy:

$$E_{el}^\tau = E_{el,c}^\tau + E_{el,p}^\tau, \quad (2.60)$$

where  $E_{el,c}^\tau$  represents the elastic energy stored at the contacts given by Eq. (2.59) and  $E_{el,p}^\tau$  denotes the elastic energy of the deformed particles calculated in terms of the average particle stresses and strains

$$E_{el,p}^\tau = \frac{1}{2} \sum_{i=1}^{N_p} V_p (\sigma_p)_{ij} (\varepsilon_p)_{ij}. \quad (2.61)$$

The deformability of the particles does not contribute to the kinetic or dissipated energy, because there is no inertial term associated with the deformation of particles, nor are there any dissipative properties assumed for the deformation of the particles. The energy balance criteria described here will be used further as an additional measure of model correctness for DDEM formulation, using a selected case of particle configuration.

## 2.8 Theoretical analysis of DDEM model

Consider a row of  $N$  equal sized, disc shaped discrete elements in contact under uniaxial compression. Assuming that the particles are constrained in the lateral direction such that no buckling occurs, the column of particles is compressed with constant load  $f$  from right and left cf. Fig. 2.8.

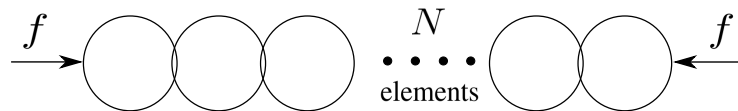


**Figure 2.8.** A row of  $N$  same sized disc elements under uniaxial compression.

The problem of the static equilibrium of this system can be solved analytically. In accordance with the illustration of contact between two deformable particles presented in Fig. 2.6, the overlap  $h$  can be decomposed into the deflection of the particles  $2h_p$  and the overlap of the deformed particles  $h_c$  :

$$h = h_c + 2h_p \quad (2.62)$$

Consistently with this decomposition, the system of two deformable particles in contact can be modelled by three springs connected in series as shown in Fig. 2.9.

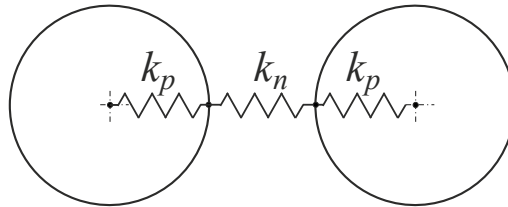


**Figure 2.9.** Equivalent rheological model for two deformable particles in contact.

The force transmitted through the elastic elements connected in series can be expressed as:

$$f = -k_n h_c \quad (2.63)$$

or

$$f = -k_p h_p \quad (2.64)$$

where  $k_p$  is the equivalent stiffness for the elastic particle subjected to compression along the diameter. The force  $f$  transferred through the row of the particles can also be given in terms of the effective stiffness  $k$  and the overlap  $h$ :

$$f = -kh \quad (2.65)$$

Substituting relationships (2.63)–(2.65) into Eq. (2.62), factoring out and cancelling  $-1$  from both the sides,

$$\frac{1}{k} = \frac{1}{k_n} + \frac{2}{k_p} \quad (2.66)$$

Finally, the effective stiffness can be expressed as follows:

$$k = \frac{k_n k_p}{2k_n + k_p} = \frac{k_n}{2k_n/k_p + 1} = \frac{k_p}{2 + k_p/k_n}. \quad (2.67)$$

It can be seen from Eq. (2.67) that if one of the stiffness parameters,  $k_n$  or  $k_p$  becomes much larger than its counterpart, the effective stiffness is determined by the smaller of the two stiffness parameters, if  $k_p \rightarrow \infty$ , then  $k \rightarrow k_n$ , and if  $k_n \rightarrow \infty$ , then  $k \rightarrow k_p/2$ , respectively. Knowing the effective stiffness  $k$ , the contact force  $f$  can be obtained from Eq. (2.65), however, in order to calculate the effective stiffness  $k$  the knowledge of the stiffness  $k_p$  is necessary. This can be determined from the strain–displacement relationship for the particle under plane strain or plane stress condition. For instance, under plane strain, using Eqs. (2.47), (2.48) for the considered problem:

$$\begin{bmatrix} \varepsilon_{xx} \\ \varepsilon_{yy} \\ 0 \end{bmatrix} = \frac{1 + \nu_p}{E_p} \begin{bmatrix} 1 - \nu_p & -\nu_p & 0 \\ -\nu_p & 1 - \nu_p & 0 \\ 0 & 0 & 2 \end{bmatrix} \begin{bmatrix} \sigma_{xx} \\ 0 \\ 0 \end{bmatrix} \quad (2.68)$$

Calculating the stress from Eq. (2.41)

$$\sigma_{xx} = \frac{2f}{\pi Rl} \quad (2.69)$$

$l$  being the depth of the sample ( $l = 1$  m), and taking

$$\varepsilon_{xx} = -\frac{h_p}{R} \quad (2.70)$$

one gets

$$f = -\frac{\pi E_p l}{2(1 - \nu_p^2)} h_p. \quad (2.71)$$

Hence, by comparison of equations (2.64) and (2.71),

$$k_p = \frac{\pi E_p l}{2(1 - \nu_p^2)}. \quad (2.72)$$

Substituting relationships (2.72) and (2.67) into Eq. (2.65) one can obtain the analytical solution for the contact force in the problem under consideration. Using Eq. (2.68), particle strains in the axial and lateral direction will be given as:

$$\varepsilon_{xx} = \frac{(1 - \nu_p^2)}{E_p} \sigma_{xx}, \quad (2.73)$$

$$\varepsilon_{yy} = \frac{-\nu_p(1 + \nu_p)}{E_p} \sigma_{xx}. \quad (2.74)$$

For the  $N$  no. particles considered in this problem, the total no. of contacts will be given as  $(N - 1)$ , which means that the row of particles shown in Fig. 2.8 can be viewed as  $(N - 1)$  elastic springs each of stiffness  $k$  under uniaxial compression. Therefore, the total displacement  $\Delta H$  of the row assembly of  $N$  particles can be determined as:

$$\Delta H = \frac{(N - 1)f}{k} \quad (2.75)$$

The analytical expressions derived here will be used further in the verification of numerical results for selected DDEM models.

## 2.9 FEM analysis of two particle DDEM model

The purpose of this test is to investigate the relation of the DDEM model to that in which deformability of the particles is treated more precisely using the finite element method. Assuming that two halves of cylindrical discs with dimensions and properties,  $R = 1$  mm, Young's modulus  $E_p = 2 \cdot 10^{11}$  Pa, Poisson's ratio  $\nu_p = 0.35$  have been subjected to a uniaxial compression along the  $y$  axis cf. Fig. 2.10a. The loading has

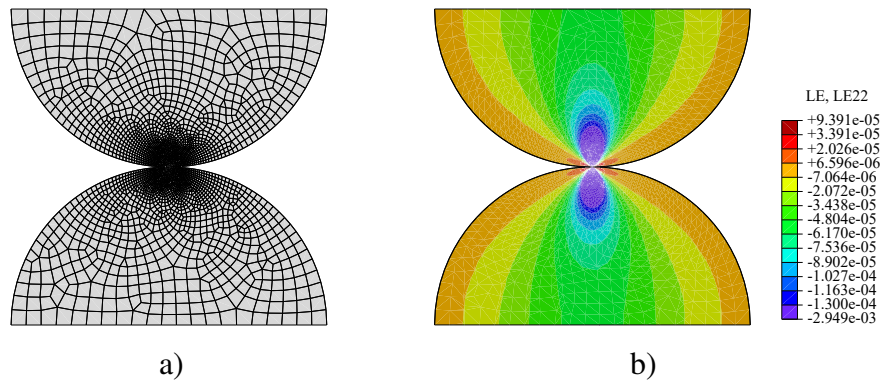


**Figure 2.10.** FEM simulation of uniaxial compression of two particles: a) FEM model, b) simulation results – distribution of strain  $\varepsilon_{yy}$  for contact force of 10 kN.

been applied kinematically by prescribing equal and opposite velocities 0.125 m/s in the  $y$  direction for the nodes in the top and bottom planes. The motion in the direction transverse to the loading has not been restrained. Frictionless contact conditions have been assumed. The problem has been analysed for plane stress and quasistatic conditions using the Abaqus/Explicit software.

The contact force between the cylinders (per 1 m) is plotted in Figure 2.11 as a function of the relative displacement of the top and bottom planes  $h$ . The spatial distribution

of the strain component  $\varepsilon_{yy}$  in the cylinders for the contact force 10 kN is shown in Figure 2.10b. The distribution of the strain  $\varepsilon_{yy}$  along the  $y$  axis (taking  $y = 0$  at the cylinder centre) is plotted in Figure 2.12. Figures 2.10b and 2.12 demonstrate a significant concentration of deformation near the contact zone while most of the particle volume is much less deformed. This effect in a certain manner supports the idea of the DDEM, in which a global deformation due to average uniform stress and local deformation concentrated at the contact zone represented by the overlap of globally deformed particles has been assumed.

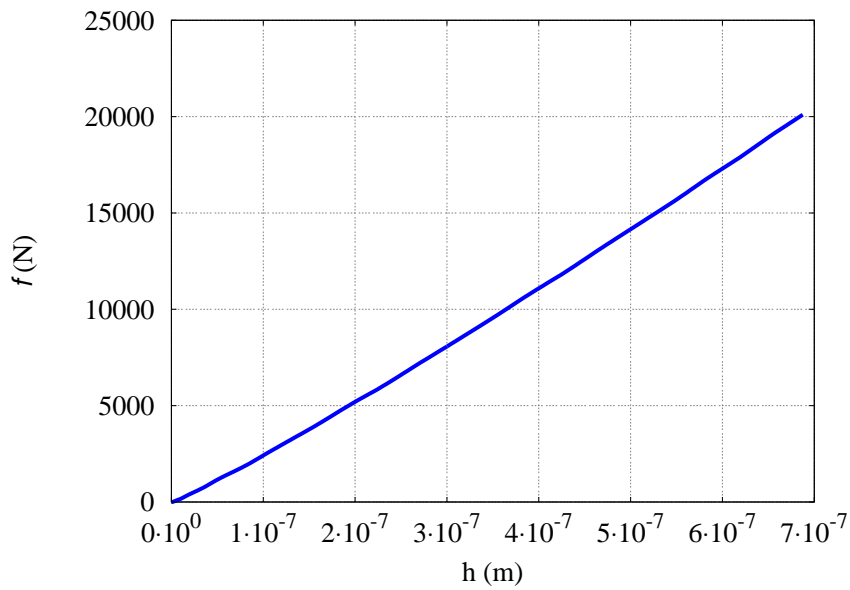


**Figure 2.11.** Contact force as a function of relative displacement.

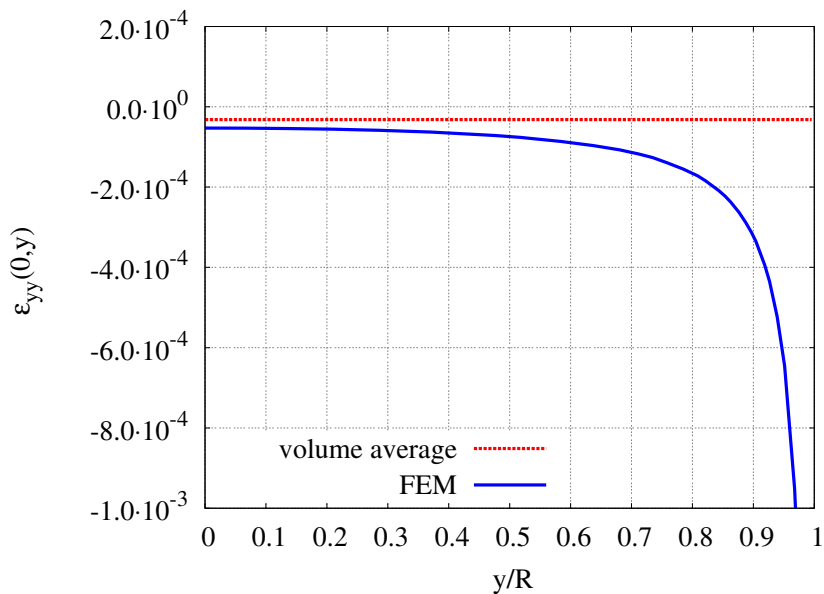


**Figure 2.12.** Distribution of strain  $\varepsilon_{yy}$  along the  $y$  axis at contact force of 10 kN.

A quantitative relationship between the DDEM model and the FEM solution has been investigated. This study has been illustrated graphically in Figure 2.13. Figure 2.13a presents the initial configuration of the two halves of discs, and Figure 2.13b shows schematically the deformed configuration obtained in the FEM simulation where the distance between the disc centres has been decreased by  $h$  (for 10 kN  $h = -3.65 \cdot 10^{-07}$  m). The approach of the disc centres  $h$  is used in the standard DEM contact models as equal to the particle overlap. It should be mentioned that the contact in the FEM analysis has been enforced by the penalty method, however, the penalty parameter was sufficiently high so that the particle penetration was negligible with respect to the displacements of cylinder centres.

Figure 2.13c shows a hypothetical configuration of the discs deformed under averaged strains without any overlap. The approach of the centres  $2h_p$  for this case can be evaluated using the relationships presented earlier in this chapter. Using Eq. (2.41) for the whole cylinder (together with the symmetrical half not considered explicitly in the model) the stress  $\sigma_{yy}^{avg}$  for the compressive contact force of magnitude  $f = 10$  kN is obtained as

$$\sigma_{yy}^{avg} = -\frac{2fR}{\pi R^2 L} = -\frac{20000}{\pi \cdot 0.001 \cdot 1} \text{ Pa} = -6.37 \text{ MPa}$$

Then, the average strain component is evaluated as

$$\epsilon_{yy}^{avg} = \frac{\sigma_{yy}^{avg}}{E_p} = \frac{-6.37 \cdot 10^6}{2 \cdot 10^{11}} = -3.18 \cdot 10^{-05},$$

The averaged strain  $\epsilon_{yy}^{avg}$  has been plotted for comparison in Figure 2.12. The change of the distance between the particle centres is equal to the change of the particle diameter

$$2h_p = 2R\epsilon_{yy}^{avg} = -2 \cdot 0.001 \cdot 3.18 \cdot 10^{-05} \text{ m} = -6.37 \cdot 10^{-08} \text{ m}$$

The absolute value of this approach without any particle overlap is smaller than that obtained in the FEM analysis, the difference being

$$h_c = h - 2h_p = -3.65 \cdot 10^{-07} \text{ m} - (-6.37 \cdot 10^{-08}) \text{ m} = -3.01 \cdot 10^{-07} \text{ m}.$$

Assuming now that the overlap  $h_c$  between the uniformly deformed particles (Figure 2.13d) is allowed by introducing a spring at the contact points with such stiffness  $k_n$  that the contact force will be unchanged

$$k_n = \frac{f}{h_c} = \frac{-10000}{-3.01 \cdot 10^{-07}} = 3.32 \cdot 10^{10} \text{ N/m}$$

In this way, it has been shown that the DDEM model with an appropriate contact stiffness yields an equivalent response in the loading direction to that obtained in the FEM analysis.

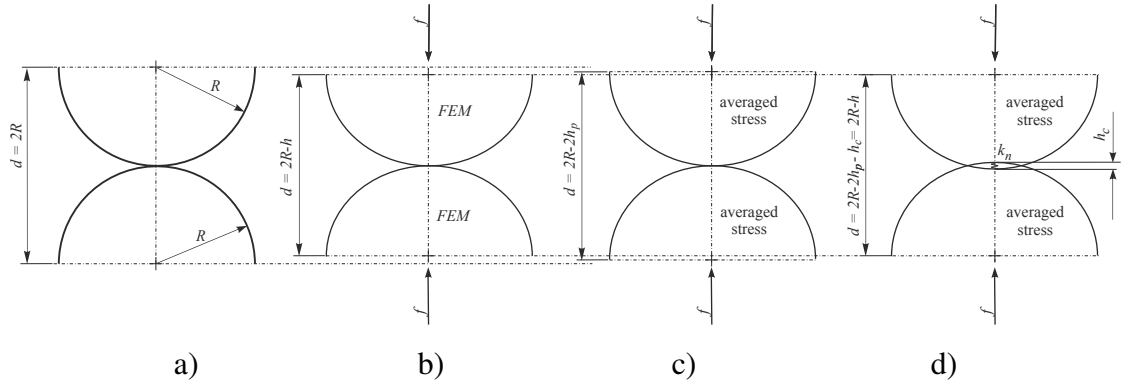


**Figure 2.13.** Equivalence between the FEM and DDEM solution for the contact of two particles compressed uniaxially: a) initial configuration without loading, b) deformed configuration in the FEM solution, c) deformed configuration under averaged stress, d) deformed configuration in the DDEM.

Additionally, the particle deformation in the lateral direction in both models can be compared. The averaged strain component  $\epsilon_{xx}^{avg}$  and the corresponding change of the particle diameter in the  $x$  direction  $h_x^{avg}$  can be obtained as follows

$$\epsilon_{xx}^{avg} = \frac{-\nu \sigma_{yy}^{avg}}{E_p} = \frac{0.35 \cdot 6.37 \cdot 10^6}{2 \cdot 10^{11}} = 1.11 \cdot 10^{-5}.$$

$$h_x^{avg} = 2R \epsilon_{xx}^{avg} = 2 \cdot 0.001 \cdot 1.11 \cdot 10^{-5} \text{ m} = 2.23 \cdot 10^{-8} \text{ m}$$

There is a certain difference with the FEM solution  $3.11 \cdot 10^{-8}$  m. This relatively small difference can be eliminated by taking slightly different value of the Poisson's ratio for the particle in the DDEM.

## Summary

The underlying concept for the deformable discrete element model has been presented. By introducing the concept of global deformation, it has been illustrated that in DDEM the non-locality of the particle deformation results in new additional contacts in contrast to the standard formulation of DEM. The simplified way used in DDEM for contact detection has been described. The standard algorithmic structure of DEM remains intact in DDEM formulation. DDEM model of a row of  $N$  equal sized discrete elements has been examined theoretically. The results obtained with the theoretical analysis will be useful in verification of numerical results of DDEM model for selected cases. It has been shown that by using appropriate contact parameters in DDEM model, an equivalent FEM response can be obtained in loading direction for two particle model.

# Chapter 3

## Convergence and stability analysis of the deformable discrete element model

### Introduction

This chapter delves into the study of numerical properties of the solution scheme employed in the DDEM which is detailed in [127] and outlined in Chapter 2. As described previously, in the DDEM formulation the volume averaged stress derived in terms of contact forces is taken as particle stress from which strains are evaluated using the inverse constitutive relationship. The contact forces are evaluated in terms of overlap of the globally deformed particles, which in turn determines the particle deformation, hence implying an implicit relationship for the contact forces. This implicit problem could be solved iteratively, however, this would be inconsistent with an efficient time step solution of the standard DEM. Therefore, the DDEM algorithm has been adapted to the explicit time integration scheme. In the present chapter, the stability of the explicit DDEM algorithm has been investigated. Firstly, the stability requirements for the micromechanical parameters related to the convergence criterion of the iterative solution of the implicit DDEM formulation has been studied. Secondly, the stability limits on the time step in the DDEM have been investigated and compared with the critical time step in the standard DEM.

The convergence criteria of the iterative solution scheme have been determined analytically for three simple regular geometries of equal size particles, namely, an infinite row of discs, infinite arrays of discs arranged in simple cubic (SC) and a hexagonal closed packing (HCP) configurations. The convergence criterion for the infinite row of particles has been verified by the numerical iterative solution of the row of particles under the step compressive loading. The analytical convergence criteria for the SC and HCP arrays have been used to establish relationships between the convergence of the iterative

DDEM scheme and the stability of the explicit DDEM solution. Numerical studies have comprised simulations of uniaxial compression of rectangular samples discretized with particles arranged in the regular SC and HCP configurations. The results have allowed to establish the criteria for choosing microscopic parameters in the calibration of the DDEM models, cf. [127], ensuring a stable solution. The results presented in this chapter are some of the major achievements of this thesis and published in [88].

### 3.1 Implicit relationship for the contact forces in DDEM

Analysing the procedure of the contact force evaluation in the DDEM defined by Eqs. (2.41)–(2.54) one can easily notice that the contact force for any interacting pair of particles depend on the positions of contacting particles and their deformation. This in turn depends on the contact forces acting on these particles as well as indirectly on all the contact forces in the particle assembly since the contact forces depend on the deformation of all the particles. Such a dependence can be written in the form of a general implicit relationship for all the contact forces in the particle system

$$\mathbf{F}_c = \mathcal{F}(\mathbf{X}, \mathbf{E}(\mathbf{F}_c)), \quad (3.1)$$

where  $\mathbf{F}_c$ ,  $\mathbf{X}$  and  $\mathbf{E}$  are the global vectors containing all the contact forces  $\mathbf{f}_c^j$ , particle positions  $\mathbf{x}_p^i$  and particle strains  $\tilde{\boldsymbol{\epsilon}}_p^i$ :

$$\mathbf{F}_c = \{\mathbf{f}_c^1, \dots, \mathbf{f}_c^{N_c}\}^T, \quad (3.2)$$

$$\mathbf{X} = \{\mathbf{x}_p^1, \dots, \mathbf{x}_p^{N_p}\}^T, \quad (3.3)$$

$$\mathbf{E} = \{\tilde{\boldsymbol{\epsilon}}_p^1, \dots, \tilde{\boldsymbol{\epsilon}}_p^{N_p}\}^T, \quad (3.4)$$

where  $N_p$  is the number of particles, and  $N_c$  is the number of contacts in the particle assembly.

### 3.2 Iterative procedure of the DDEM

Evaluation of the contact forces using the implicit relationship given by Eq. (3.1) would require an iterative solution at each time step

$$\mathbf{F}_c^{(n,k+1)} = \mathcal{F}(\mathbf{X}^{(n)}, \mathbf{E}(\mathbf{F}_c^{(n,k)})) \quad (3.5)$$

where the superscript  $n$  denotes the  $n$ -th time step, and the superscripts  $k$  and  $k + 1$  subsequent iterations. Given the particle positions  $\mathbf{X}^{(n)}$  obtained for the  $n$ -th time step

from the explicit time integration of the equations of motion, the iterative solution scheme to determine the interparticle contact forces  $\mathbf{F}_c^{(n)}$  can be outlined as follows:

1. For the  $k$ -th iteration, taking the contact forces from the previous iteration  $\mathbf{F}_c^{(n,k-1)}$  calculate the particle stresses  $\boldsymbol{\sigma}_p^{(n,k)}$  according to Eq. (2.41). The contact forces for the first iteration ( $k = 1$ ) can be taken from the previous time step

$$\mathbf{F}_c^{(n,0)} = \mathbf{F}_c^{(n-1)}. \quad (3.6)$$

2. Calculate the particle strains  $\boldsymbol{\epsilon}_p^{(n,k)}$  using the constitutive relationship (2.47).
3. Evaluate the particle deformation at the contact points due to the strains  $\boldsymbol{\epsilon}_p^{(n,k)}$  according to Eq. (2.52).
4. Calculate the overlap between the deformed particles according to Eq. (2.53). Determine the contact between the deformed particles for given particle positions  $\mathbf{x}^{(n)}$ .
5. Calculate new values of the contact forces  $\mathbf{F}_c^{(n,k)}$  with the normal components evaluated according to Eq. (2.20)
6. Check the convergence of the solution. The convergence criterion can be defined in terms of a difference of contact forces from the present and previous iterations. If the convergence criterion is satisfied

$$\mathbf{F}_c^{(n)} = \mathbf{F}_c^{(n,k)}, \quad (3.7)$$

otherwise, repeat the steps 1–6 until the convergence is reached.

Assuming a linear constitutive contact model as given by Eq. (2.54), it is possible to construct for the whole discrete system the following recursive relationship corresponding to the above iterative scheme:

$$\mathbf{F}_c^{(n,k)} = \mathbf{A}\mathbf{X}^{(n)} + \mathbf{B}\mathbf{F}_c^{(n,k-1)}, \quad k \geq 1, \quad (3.8)$$

where  $\mathbf{A}$  and  $\mathbf{B}$  are certain matrices. Rewriting the formula (3.8) replacing  $k$  by  $k + 1$ :

$$\mathbf{F}_c^{(n,k+1)} = \mathbf{A}\mathbf{X}^{(n)} + \mathbf{B}\mathbf{F}_c^{(n,k)}, \quad k \geq 0. \quad (3.9)$$

Subtracting Eq. (3.8) from Eq. (3.9) the recursive relationship for the successive differences is obtained

$$\mathbf{F}_c^{(n,k+1)} - \mathbf{F}_c^{(n,k)} = \mathbf{B}(\mathbf{F}_c^{(n,k)} - \mathbf{F}_c^{(n,k-1)}), \quad k \geq 1. \quad (3.10)$$

The iterative solution may not always converge. In general, the convergence requires that for a certain matrix norm  $\|\cdot\|$ , cf. [66]:

$$\|\mathbf{B}\| < 1 \quad (3.11)$$

then the ratio of the norms of successive differences

$$\frac{\|\mathbf{F}_c^{(n,k+1)} - \mathbf{F}_c^{(n,k)}\|}{\|\mathbf{F}_c^{(n,k)} - \mathbf{F}_c^{(n,k-1)}\|} < 1, \quad (3.12)$$

which indicates that the iterative error decreases. However, the norm of  $\mathbf{B}$  could be small in some norms and quite large in others. A more stringent convergence condition can be expressed in terms of the matrix spectral radius  $\rho(\mathbf{B})$ , cf. [66]:

$$\rho(\mathbf{B}) < 1 \quad (3.13)$$

The spectral radius of the iteration matrix  $\mathbf{B}$  is defined as

$$\rho(\mathbf{B}) = \max_{\lambda \in \Phi(\mathbf{B})} |\lambda| \quad (3.14)$$

with  $\lambda$  being the eigenvalue of  $\mathbf{B}$  and  $\Phi(\mathbf{B})$  denoting the set of eigenvalues of  $\mathbf{B}$ . For a symmetric matrix  $\mathbf{B}$  the spectral radius  $\rho(\mathbf{B})$  is equivalent to the 2-norm  $\|\mathbf{B}\|_2$ , cf. [1]:

$$\rho(\mathbf{B}) = \|\mathbf{B}\|_2, \quad (3.15)$$

with the 2-norm defined as:

$$\|\mathbf{B}\|_2 = (\mu_{\max})^{1/2}, \quad (3.16)$$

where  $\mu_{\max}$  is the largest eigenvalue of  $\mathbf{B}^T \mathbf{B}$ .

The explicit forms of the iterative relationship (3.10) and of the iteration matrix  $\mathbf{B}$  will be obtained for simple cases further on. This will allow to estimate theoretically the convergence of the iterative scheme and compare it with the convergence limit obtained in numerical simulations.

### 3.3 Explicit solution algorithm of the DDEM

The iterative solution within the explicit time integration which is used in the discrete element method would spoil its major advantage of yielding an efficient solution for a single time step. Therefore the solution algorithm proposed in [127] employs an explicit dependence which can be written generally as follows:

$$\mathbf{F}_c^{(n)} = \mathcal{F}(\mathbf{X}^{(n)}, \mathbf{E}(\mathbf{F}_c^{(n-1)})) \quad (3.17)$$

The contact forces at the  $n$ -th time step are evaluated taking the strains obtained for the contact forces from the previous time step. The algorithm for the deformable discrete elements is incorporated into the explicit time integration solution. No iterations are performed at time steps, convergence is achieved along with time stepping.

The 2D DDEM algorithm has been implemented in the discrete element program DEMPack validated earlier in different applications, cf. [123, 125]. With respect to the standard DEM formulation, the new algorithm additionally requires calculation of the particle stresses and strains. Before the contact detection, the particle stresses  $\sigma_p^{(n)}$  are evaluated according to Eq. (2.41) taking the contact forces from the previous time step  $F_c^{(n-1)}$ . Then, the particle strains  $\epsilon_p^{(n)}$  are calculated using the constitutive relationship (2.47). The contact detection and contact force evaluation in the new algorithm is modified with respect to the standard DEM. The contact between the particles is established accounting for the particle deformation under the uniform strain  $\epsilon_p^{(n)}$  induced by the contact forces. The overlap (or in the case of the cohesive contact, it may be also a gap) between the deformed particles is taken for the contact evaluation.

In this chapter, the stability of the solution scheme in the DDEM will be investigated. The critical time step will be evaluated and compared with that of the standard DEM. One may expect that owing to the added global deformation mode, the effective contact stiffness in the normal direction in DDEM decreases w.r.t. standard DEM and as a consequence, the critical time step can be decreased as predicted by Eq. (2.18) or (2.19). On the other hand, the stability of the explicit solution scheme can be affected by the limitations established for the iterative solution. These questions will be investigated through the analytical derivations and numerical simulations presented in the following sections.

### 3.4 Infinite row of particles

An infinite row of particles (discs) subjected to compression, as shown in Figure 3.1, has been studied in order to verify the convergence criterion of the iterative solution. Equal particles of radii  $R = 1$  mm under the plane strain conditions have been assumed. The local contact stiffness  $k_n = 7 \cdot 10^{10}$  N/m has been taken.

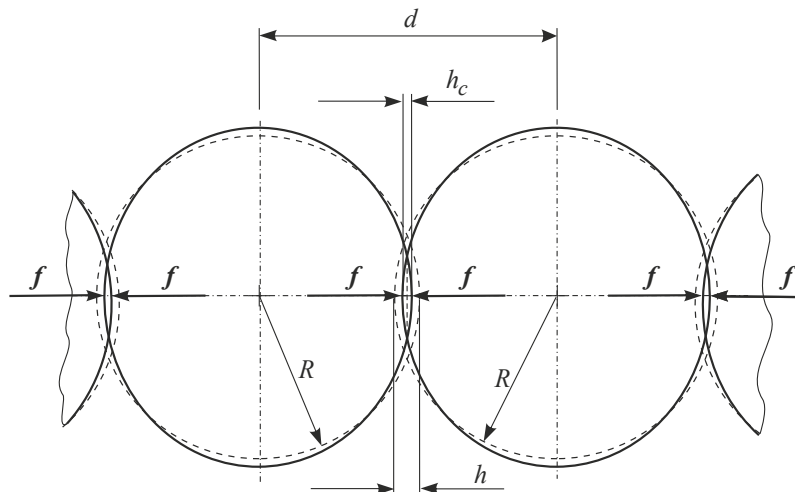


**Figure 3.1.** Compression of an infinite row of particles.

The kinematically controlled step loading has been introduced. The distance between the particle centres  $d = 1.99$  mm has been prescribed. Thus, the overlap between the undeformed particles  $h = 2R - d$  amounts to 0.01 mm. The solution is aimed to determine the deformation of the particles and the contact force between the deformed particles. The system of the connected particles has been studied for different ratios of the local (contact) and global (particle) stiffness. The global particle stiffness has been given in terms of the elastic moduli,  $E_p$  and  $\nu_p$ .

It can be seen that the analytical solution for the contact force in the problem under consideration can be obtained on the basis of the theoretical analysis presented in Sec. 2.8. The numerical solution should converge to the value obtained by substituting relationships (2.72) and (2.67) into Eq. (2.65). Since the positions of the particles do not change during the analysed period the solution is equivalent to the iterative procedure presented in Section. 3.2. Rewriting it here for the problem under consideration:

1. Calculate the particle stress for the  $k$ -the iteration  $\sigma_{xx}^{(k)}$  taking the contact force from the previous iteration  $f^{(k-1)}$

$$\sigma_{xx}^{(k)} = \frac{2f^{(k-1)}}{\pi Rl} \quad (3.18)$$

2. Calculate the particle strain

$$\varepsilon_{xx}^{(k)} = \frac{1 - \nu_p^2}{E_p} \sigma_{xx}^{(k)} \quad (3.19)$$

3. The semiaxis of the deformed particle is given by

$$a^{(k)} = R(1 + \varepsilon_{xx}^{(k)}) \quad (3.20)$$

4. The particle overlap is calculated as follows

$$h_c^{(k)} = 2R(1 + \varepsilon_{xx}^{(k)}) - d = h + 2R\varepsilon_{xx}^{(k)} \quad (3.21)$$

5. The new value of the contact force is calculated as

$$f^{(k)} = -k_n h_c^{(k)} \quad (3.22)$$

Substituting Eqs. (3.19) and (3.21) into Eq. (3.22) the following relationship is obtained

$$f^{(k)} = -k_n h_c^{(k)} = -k_n (h + 2R\varepsilon_{xx}^{(k)}) = -k_n h - 2k_n R \frac{1 - \nu_p^2}{E_p} \sigma_{xx}^{(k)} \quad (3.23)$$

and taking into account (3.18)

$$f^{(k)} = -k_n h - 2k_n \frac{2(1 - \nu_p^2)}{\pi E_p l} f^{(k-1)} = k_n h - \frac{2k_n}{k_p} f^{(k-1)} \quad (3.24)$$

The recursive relationship (3.24) is a specific form of the relationship (3.8). The relationship between successive differences corresponding to the relationship (3.10) can be easily obtained as:

$$f^{(k+1)} - f^{(k)} = -\frac{2k_n}{k_p}(f^{(k)} - f^{(k-1)}) \quad (3.25)$$

The respective convergence criterion corresponding to the inequality (3.11) takes the form:

$$\left| -\frac{2k_n}{k_p} \right| < 1 \quad (3.26)$$

which gives

$$\frac{2k_n}{k_p} < 1 \quad (3.27)$$

The convergence criterion limits the use of the DDEM algorithm to the particles, whose global stiffness is sufficiently large with respect to the local contact stiffness, nevertheless this corresponds to many real applications in which local deformations due to the contact are quite large and the global deformations are relatively small.

The studies have been performed for the Poisson's ratio  $\nu_p = 0.35$  and selected values of the Young's modulus  $E_p$  in the range limited by the criterion (3.27). The results of the analytical calculations are given in Table 3.1. Having assumed the Young's modulus  $E_p$ , the particle stiffness  $k_p$  has been obtained from Eq. (2.72). The ratio  $2k_n/k_p$  allows to verify the criterion given by Eq. (3.27). It can be noted that the lowest considered value of the Young's modulus gives the ratio  $2k_n/k_p$  close to unity. Further on, the effective

**Table 3.1.** Analytical predictions for the infinite row of particles

No.	$E_p$ (Pa)	$k_p$ (N/m)	$2k_n/k_p$	$k$ (N/m)	$f$ (kN)
1	$5.00 \cdot 10^{11}$	$8.946 \cdot 10^{11}$	0.16	$6.053 \cdot 10^{10}$	$6.053 \cdot 10^2$
2	$4.00 \cdot 10^{11}$	$7.157 \cdot 10^{11}$	0.19	$5.855 \cdot 10^{10}$	$5.855 \cdot 10^2$
3	$3.00 \cdot 10^{11}$	$5.368 \cdot 10^{11}$	0.26	$5.552 \cdot 10^{10}$	$5.552 \cdot 10^2$
4	$2.00 \cdot 10^{11}$	$3.578 \cdot 10^{11}$	0.39	$5.031 \cdot 10^{10}$	$5.031 \cdot 10^2$
5	$1.00 \cdot 10^{11}$	$1.789 \cdot 10^{11}$	0.78	$3.927 \cdot 10^{10}$	$3.927 \cdot 10^2$
6	$8.00 \cdot 10^{10}$	$1.431 \cdot 10^{11}$	0.98	$3.539 \cdot 10^{10}$	$3.539 \cdot 10^2$

stiffness  $k$  and the force  $f$  have been calculated from Eqs. (2.67) and (2.65), respectively. The effective stiffness  $k$  has been plotted as a function of the ratio  $2k_n/k_p$  in Fig. 3.2.

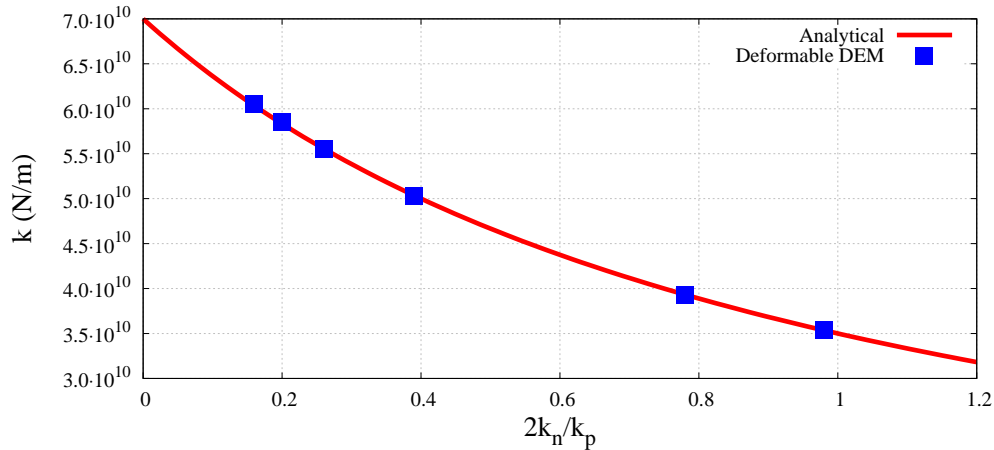


**Figure 3.2.** Effective stiffness as a function of the contact–particle stiffness ratio.

Numerical simulations have been performed using a model consisting of a pair of particles with fixed positions yielding the prescribed initial overlap  $h = 0.01$  mm. The interaction with the other particle neighbours has been taken into account assuming the same contact force as that determined between the two considered particles. Thus, the particle stresses have been calculated correctly.

Iterative solutions for the contact force in 4 selected cases are shown in Fig. 3.3. The plots show that the solution converges to the theoretical values of the contact force if  $2k_n/k_p < 1$  (Fig. 3.3a-c). The numerical values of the forces  $f$  are exactly the same as those given in Table 3.1, which confirms the correct behaviour of the algorithm.

The rate of convergence depends on the value of the stiffness ratio  $2k_n/k_p$ . The solution converges very fast for lower values of the ratio  $2k_n/k_p$  (Fig. 3.3a) and the convergence is quite slow for the ratio  $2k_n/k_p$  close to 1 (Fig. 3.3c). When  $2k_n/k_p \geq 1$  the solution does not converge (Fig. 3.3d). Thus, the tests have confirmed the convergence criterion (3.27) which has been derived theoretically.

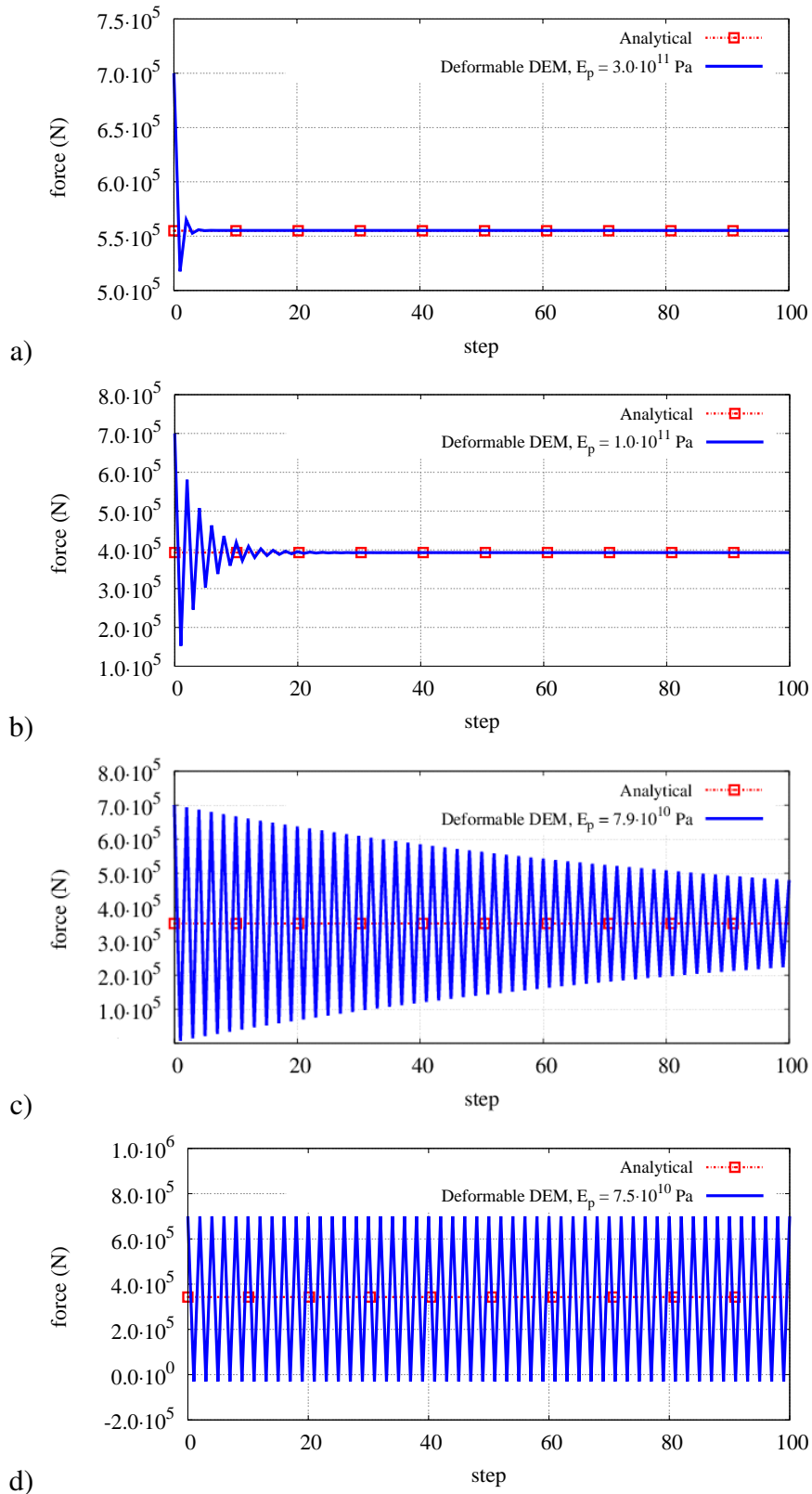


**Figure 3.3.** Iterative solution for the contact force in the row of spheres under compression for different stiffness of spheres: a)  $E_p = 3 \cdot 10^{11}$  Pa ( $2k_n/k_p = 0.260$ ), b)  $E_p = 1 \cdot 10^{11}$  Pa ( $2k_n/k_p = 0.782$ ), c)  $E_p = 7.9 \cdot 10^{10}$  Pa ( $2k_n/k_p = 0.992$ ) d)  $E_p = 7.5 \cdot 10^{10}$  Pa ( $2k_n/k_p = 1.043$ ).

### 3.5 Simple cubic configuration

Convergence and stability of the DDEM applied to a regular simple cubic (SC) configuration of particles have been investigated analytically and numerically. Numerical simulations have been performed for the uniaxial compression of the rectangular sample shown in Fig. 3.4a. The theoretical convergence analysis has been carried considering a unit SC cell shown in 3.4b.

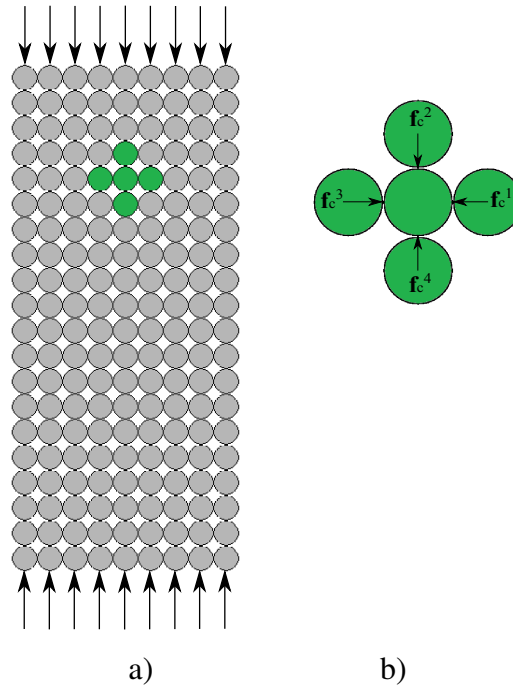


**Figure 3.4.** Unconfined uniaxial compression of a simple cubic specimen – a) DEM model b) a unit cell.

Assuming that the SC unit cell belongs to an infinite grid of equal particles of radii  $R$  with prescribed spacing between the columns and rows,  $d_x$  and  $d_y$ , respectively, inducing the interparticle interaction due to initial overlaps:

$$h_x = 2R - d_x \quad (3.28)$$

$$h_y = 2R - d_y \quad (3.29)$$

where  $h_x, h_y > 0$ . Let the contact forces acting on a particle be represented as  $\mathbf{f}_c^i$ ,  $i = 1, \dots, 4$ . In terms of their magnitudes  $f_i$ ,  $i = 1, \dots, 4$ , contact force vectors are given as,  $\mathbf{f}_c^1 = [-f_1 \ 0]^T$ ,  $\mathbf{f}_c^2 = [0 \ -f_2]^T$ ,  $\mathbf{f}_c^3 = [f_3 \ 0]^T$ ,  $\mathbf{f}_c^4 = [0 \ f_4]^T$ . Making use of the symmetry of the pattern and loading with respect to the  $x$  and  $y$  axes,  $f_1 = f_3 = f_x$  and  $f_2 = f_4 = f_y$ .

To obtain a relationship for convergence, the iterative procedure presented in section 3.2 for the SC contact configuration shall be rewritten. Analogous to the procedure for compression of an infinite row of particles as presented in section 3.4 iterative procedure is as follows (superscript  $n$  denotes the time step and  $k-1, k, k+1$  represent the successive iterations):

1. Calculate the stress components at  $n$ -th time step and  $k$ -th iteration in terms of corresponding force components at the same time step  $n$  and previous iteration  $k-1$

$$\begin{bmatrix} \sigma_{xx}^{(n,k)} \\ \sigma_{yy}^{(n,k)} \end{bmatrix} = -\frac{2}{\pi Rl} \begin{bmatrix} f_x^{(n,k-1)} \\ f_y^{(n,k-1)} \end{bmatrix} \quad (3.30)$$

where  $l$  is the length of particle in a direction perpendicular to its plane assumed to have a unit dimension ( $l = 1$  m).

2. Calculate the particle strain components at time step  $n$  and  $k$ -th iteration for the assumed plane-strain condition

$$\begin{bmatrix} \varepsilon_{xx}^{(n,k)} \\ \varepsilon_{yy}^{(n,k)} \end{bmatrix} = \frac{1 + \nu_p}{E_p} \begin{bmatrix} (1 - \nu_p) & -\nu_p \\ -\nu_p & (1 - \nu_p) \end{bmatrix} \begin{bmatrix} \sigma_{xx}^{(n,k)} \\ \sigma_{yy}^{(n,k)} \end{bmatrix} \quad (3.31)$$

3. The semiaxes of the deformed particle are given by

$$\begin{bmatrix} a_{xx}^{(n,k)} \\ a_{yy}^{(n,k)} \end{bmatrix} = R \begin{bmatrix} 1 + \varepsilon_{xx}^{(n,k)} \\ 1 + \varepsilon_{yy}^{(n,k)} \end{bmatrix} \quad (3.32)$$

4. The particle overlaps in  $x$  and  $y$  direction are determined as follows

$$\begin{bmatrix} h_{cx}^{(n,k)} \\ h_{cy}^{(n,k)} \end{bmatrix} = 2R \begin{bmatrix} 1 + \varepsilon_{xx}^{(n,k)} \\ 1 + \varepsilon_{yy}^{(n,k)} \end{bmatrix} - \begin{bmatrix} d_x \\ d_y \end{bmatrix} = \begin{bmatrix} h_x \\ h_y \end{bmatrix} + 2R \begin{bmatrix} \varepsilon_{xx}^{(n,k)} \\ \varepsilon_{yy}^{(n,k)} \end{bmatrix} \quad (3.33)$$

5. The new values of contact force components is calculated as follows

$$\begin{bmatrix} f_x^{(n,k)} \\ f_y^{(n,k)} \end{bmatrix} = -k_n \begin{bmatrix} h_{cx}^{(n,k)} \\ h_{cy}^{(n,k)} \end{bmatrix} \quad (3.34)$$

Substituting Eqs. (3.33) and (3.31) into Eq. (3.34) one obtains

$$\begin{bmatrix} f_x^{(n,k)} \\ f_y^{(n,k)} \end{bmatrix} = -k_n \begin{bmatrix} h_x \\ h_y \end{bmatrix} - \frac{2Rk_n(1 + \nu_p)}{E_p} \begin{bmatrix} (1 - \nu_p) & -\nu_p \\ -\nu_p & (1 - \nu_p) \end{bmatrix} \begin{bmatrix} \sigma_{xx}^{(n,k)} \\ \sigma_{yy}^{(n,k)} \end{bmatrix} \quad (3.35)$$

and taking into account (3.30)

$$\begin{bmatrix} f_x^{(n,k)} \\ f_y^{(n,k)} \end{bmatrix} = -k_n \begin{bmatrix} h_x \\ h_y \end{bmatrix} + \frac{4k_n(1+\nu_p)}{\pi E_p l} \begin{bmatrix} (1-\nu_p) & -\nu_p \\ -\nu_p & (1-\nu_p) \end{bmatrix} \begin{bmatrix} f_x^{(k-1)} \\ f_y^{(k-1)} \end{bmatrix} \quad (3.36)$$

The recursive relationship (3.36) is a particular form of the relationship (3.8). The relationship between successive differences corresponding to the relationship (3.10) can be easily obtained as:

$$\begin{bmatrix} f_x^{(n,k+1)} - f_x^{(n,k)} \\ f_y^{(n,k+1)} - f_y^{(n,k)} \end{bmatrix} = \frac{4k_n(1+\nu_p)}{\pi E_p l} \begin{bmatrix} (1-\nu_p) & -\nu_p \\ -\nu_p & (1-\nu_p) \end{bmatrix} \begin{bmatrix} f_x^{(n,k)} - f_x^{(n,k-1)} \\ f_y^{(n,k)} - f_y^{(n,k-1)} \end{bmatrix} \quad (3.37)$$

The iteration matrix  $\mathbf{B}$  now takes the form:

$$\mathbf{B} = \frac{4k_n(1+\nu_p)}{\pi E_p l} \begin{bmatrix} (1-\nu_p) & -\nu_p \\ -\nu_p & (1-\nu_p) \end{bmatrix} \quad (3.38)$$

6. In order to evaluate the convergence criterion (3.13), calculate the spectral radius of matrix  $\mathbf{B}$  using Eq. (3.14):

$$\rho(\mathbf{B}) = \max_{\lambda \in \Phi(\mathbf{B})} |\lambda| \quad (3.39)$$

where  $\Phi(\mathbf{B})$  is the set of eigenvalues of iteration matrix  $\mathbf{B}$ , cf. Eq.(3.38), which is evaluated as

$$\Phi(\mathbf{B}) = \left\{ \frac{4k_n(1+\nu_p)}{\pi E_p l}, \frac{4k_n(1+\nu_p)(1-2\nu_p)}{\pi E_p l} \right\} \quad (3.40)$$

Since  $\nu_p > 0$ , the absolute maximum eigenvalue is represented by the first element of the set  $\Phi(\mathbf{B})$

$$\rho(\mathbf{B}) = \max_{\lambda \in \Phi(\mathbf{B})} |\lambda| = \frac{4k_n(1+\nu_p)}{\pi E_p l} \quad (3.41)$$

Hence, it can be concluded that the convergence criterion for the iterative scheme is:

$$\frac{4k_n(1+\nu_p)}{\pi E_p l} < 1 \quad (3.42)$$

Inserting  $l = 1m$  in Eq. (3.42) and rewriting, a relationship for the particle Poisson's ratio  $\nu_p$  in terms of the ratio  $k_n/E_p$  is obtained in the following form:

$$\nu_p < \frac{\pi/4}{k_n/E_p} - 1 \quad (3.43)$$

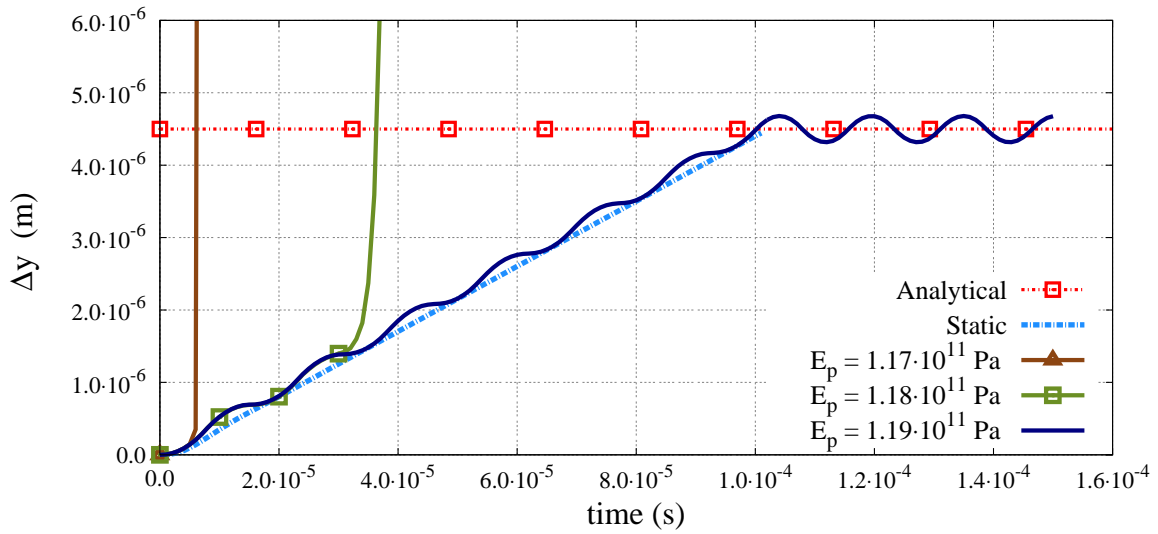


**Figure 3.5.** Comparison of displacement time curves for the unconfined uniaxial compression of SC specimen for a stable solution:  $E_p = 1.19 \cdot 10^{11}$  Pa ( $k_n/E_p = 0.588$ ) and unstable solutions:  $E_p = 1.18 \cdot 10^{11}$  Pa ( $k_n/E_p = 0.593$ ) and  $E_p = 1.17 \cdot 10^{11}$  Pa ( $k_n/E_p = 0.598$ ).

The relationship between the convergence of the iterative scheme and stability of the explicit solution scheme have been investigated by simulating unconfined uniaxial compression of a rectangular specimen discretized with bonded discs as it is shown in Fig. 3.4a. The rectangular sample contained total 180 (20 by 9) disc elements each of radius  $R = 1$  mm, resulting in a total height  $H = 40$  mm and a width  $A = 18$  mm. Microscopic properties are as follows: density  $\rho = 2000$  kg/m<sup>3</sup>, normal contact stiffness  $k_n = 7 \cdot 10^{10}$  N/m. Numerical studies have been carried out for different values of the particle Poisson's ratio  $\nu_p$  and the particle Young's modulus  $E_p$  aiming to determine their effect on the stability of the solution.

The sample has been uniaxially compressed under a uniform load represented by equal forces applied at the particles in the top and bottom row as shown in Fig. 3.4a. The particles in the middle column have been constrained horizontally to avoid any buckling effects. The loading has been applied by increasing each force linearly from 0 to 10 kN during  $0.1 \mu\text{s}$ . The total maximum force  $F$  is 90 kN.

Numerical stability has been investigated assuming a certain value of the particle Poisson's ratio  $\nu_p$  and studying the solutions for different values of the particle Young's modulus  $E_p$ . The solutions for  $\nu_p = 0.35$  and three values of  $E_p$  have been presented in Fig. 3.5 by the displacement vs. time curves. The stable solution corresponding to the particle Young's modulus  $E_p = 1.19 \cdot 10^{11}$  Pa is close to the linear quasistatic solution. It is characterized by small oscillations around the quasistatic solution since no damping has been used. The theoretical quasistatic change of the sample height for the DDEM model has been obtained using the theoretical relationship for the row of particles presented in Sec.

**Table 3.2.** Comparison between analytical predictions and numerical results for the convergence and stability limits for SC configuration with different particle Poisson's ratio  $\nu_p$  and a constant normal contact stiffness  $k_n = 7 \cdot 10^{10}$  N/m.

$\nu_p$	$k_n/E_p$ (analytical)	$k_n/E_p$ (numerical)
0.05	0.748	0.761
0.10	0.714	0.722
0.15	0.683	0.693
0.20	0.654	0.667
0.25	0.628	0.636
0.30	0.604	0.614
0.35	0.582	0.588
0.40	0.561	0.569
0.45	0.542	0.551

2.8. It can be clearly seen in Fig. 3.5 that the particle Young's moduli  $E_p = 1.17 \cdot 10^{11}$  and  $E_p = 1.18 \cdot 10^{11}$  Pa lead to unstable solutions. Therefore, for the particle Poisson's ratio  $\nu_p = 0.35$ , the particle Young's modulus  $E_p = 1.19 \cdot 10^{11}$  Pa ( $k_n/E_p = 0.588$ ) determines the numerical stability limit. In the same way, the numerical stability limits have been evaluated for the Poisson's ratio values from 0.05 to 0.45. The results are given in Table 3.2 in comparison to the theoretical convergence limits for the iterative solution scheme determined according to Eq. (3.42).

The numerical stability limit and analytical convergence limit for the SC configuration are compared graphically in Fig. 3.6. It can be observed that the stability limits achieved in the numerical simulations for different values of the particle Poisson's ratio are in a close agreement with the theoretical predictions for the convergence limit. It can be deduced that the convergence criterion for the iterative scheme also controls the stability of the explicit transient solution.

The stability of the explicit dynamic solution is also limited by the critical time step, cf. Eq. (2.14). The critical step in the DDEM solution for the SC configuration has been investigated empirically by numerical simulations and compared with the critical time step obtained in the standard DEM simulations. Both stability limits have been compared to the critical time step predicted theoretically.

The theoretical evaluation of the critical time step has been based on the assumption that the behaviour of each column of the model in the  $y$  direction is equivalent to that of the chain of particles. The eigenfrequencies of the chain of  $N$  masses  $m$  connected with

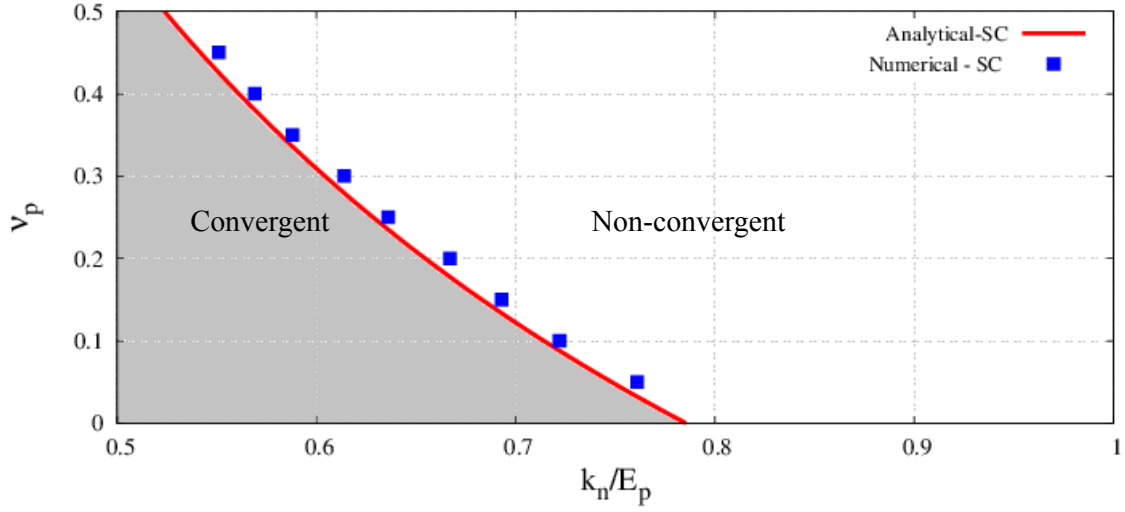


**Figure 3.6.** Comparison of the numerical stability and analytical convergence limits for SC configuration for constant normal stiffness  $k_n = 7 \cdot 10^{10}$  N/m.

springs of stiffness  $k$  are given as [130]:

$$\nu_i = 2\sqrt{\frac{k}{m}} \sin \frac{\pi i}{2(N+1)}, \quad (3.44)$$

where  $i$  is the mode number. The maximum eigenfrequency in the chain of 20 particles is obtained taking  $i = 20$  as

$$\nu_{\max} = \nu_{20} = 2\sqrt{\frac{k}{m}} \sin \frac{20\pi}{42} \approx 2\sqrt{\frac{k}{m}} \quad (3.45)$$

Hence, introducing Eq. (3.45) into Eq. (2.15) the critical time step is estimated as

$$\Delta t_{\text{cr}} \approx \sqrt{\frac{m}{k}}. \quad (3.46)$$

Taking the contact stiffness  $k = k_n = 7 \cdot 10^{10}$  N/m and the particle mass  $m = \rho\pi R^2 l = 6.283 \cdot 10^{-3}$  kg for assumed particle density  $\rho = 2000$  kg/m<sup>3</sup> and radius  $R = 1$  mm, the critical time step for the standard DEM is obtained as,

$$\Delta t_{\text{cr}} \approx \sqrt{\frac{6.283 \cdot 10^{-3}}{7 \cdot 10^{10}}} = 2.9959 \cdot 10^{-7} \text{ s} \quad (3.47)$$

The stability limits on the time step in the DEM and DDEM have been investigated by simulating an unconfined uniaxial compression under the loading conditions defined previously. Axial displacement of the discrete sample w.r.t. time obtained using the standard DEM and DDEM models has been plotted to observe the behaviour of the system for two different time steps in Fig. 3.7. The standard DEM and DDEM results have been obtained for the time step  $\Delta t$  equal to the analytically obtained value of the critical time step and a value 2% higher. For DDEM model, particle Young's moduli  $E_p = 2 \cdot 10^{11}$  Pa, particle

Poisson ratio  $\nu_p = 0.35$  is used. It can be clearly seen in Fig. 3.7 that in the standard DEM case time step  $\Delta t = 2.9959 \cdot 10^{-7}$  s leads to a stable solution converging to the analytical one. With even slightly higher time step  $\Delta t = 3.0559 \cdot 10^{-7}$  s, the simulation rapidly goes into an unstable mode. It can be observed in Fig. 3.7 that the stable solution in the DDEM can also be obtained with the time step  $\Delta t = 2.9959 \cdot 10^{-7}$  s. Similarly to the standard DEM, even a slightly higher value of time step  $\Delta t = 3.0559 \cdot 10^{-7}$  s leads to unstable simulation. Hence, it can be concluded that the critical time step remains the same for standard and deformable DEM models. This can be attributed to the fact that incremental force evaluation in the DDEM algorithm is dependent on the normal stiffness at the contact  $k_n$  and the overlap increment  $\Delta h$ , which imposes the same stability limit as in the standard DEM.

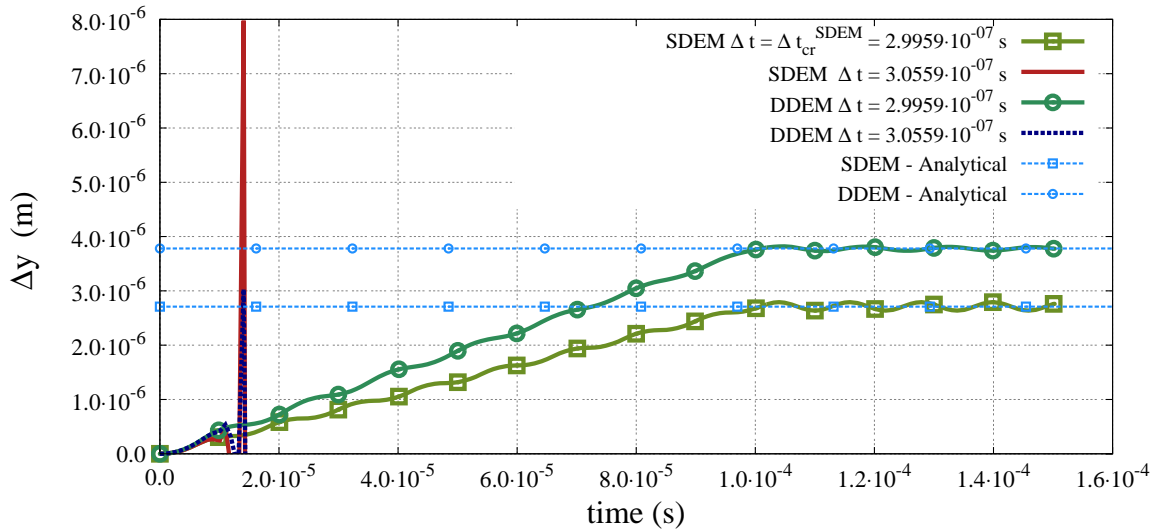


**Figure 3.7.** Comparison of displacement–time curves for the unconfined uniaxial compression of SC specimen for standard DEM and DDEM and different time steps.

### 3.6 A hexagonal closed packing configuration

The methodology used above to study the SC configuration has been applied to a hexagonal close packing (HCP) configuration. Convergence and stability of the DDEM applied to the HCP configuration of particles have been investigated analytically and numerically. Numerical simulations have been performed for the uniaxial compression of the rectangular sample shown in Fig. 3.8a. The theoretical convergence analysis has been carried considering a unit HCP cell shown in 3.8b.

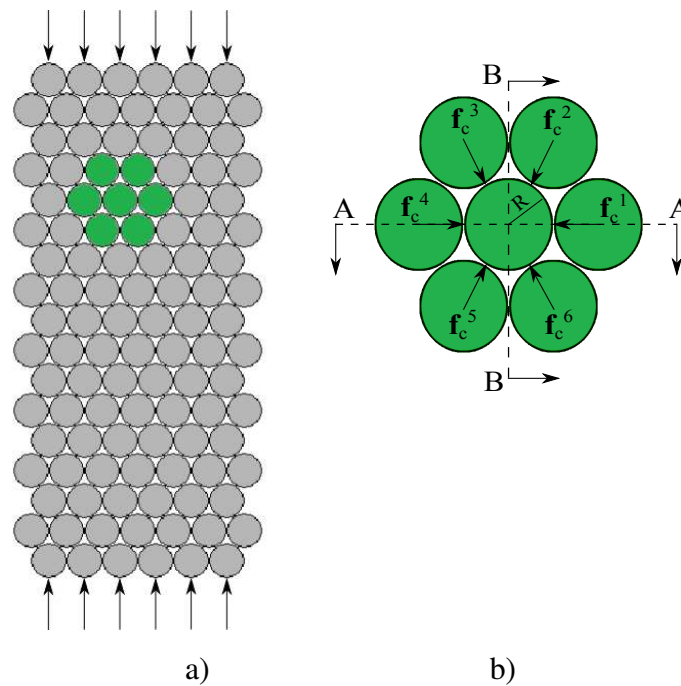


**Figure 3.8.** Unconfined uniaxial compression of an HCP specimen – a) DEM model b) a unit cell.

Assuming that the HCP unit cell belongs to an infinite lattice of equal particles of radii  $R$  with prescribed initial displacements inducing interparticle interaction. The contact forces acting on the central particle are denoted by  $\mathbf{f}_c^i$ ,  $i = 1, \dots, 6$ . It is assumed that the lattice is uniformly contracted along  $x$  and  $y$  axes. The contractions in  $x$  and  $y$  directions can be different. Such deformation imposed on the pattern with geometrical symmetry leads to the symmetry of the overlaps between contacting particles and contact forces with respect to the planes A–A and B–B (Fig. 3.8b).

The system is analysed under plane strain conditions with previously defined parameters and tangential contact stiffness,  $k_t = 0$  N/m. The iterative scheme defined in previous sections is now rewritten for the HCP configuration as below. Superscript  $n$  denotes the time step and  $k - 1$ ,  $k$ ,  $k + 1$  represent the successive iterations as before. Magnitudes of contact force vectors are denoted as  $f_i$  for  $i = 1, \dots, 6$ .

1. Calculate the stress components at time step  $n$  and  $k$ -th iteration in terms of corresponding force components at the same time step  $n$  and previous iteration  $k - 1$ .

Consider an arbitrary unit cell as shown in Fig. 3.9 from an infinite HCP lattice of 2D particles of equal radius  $R$ . As mentioned above, the geometry pattern and particle displacements are symmetrical with respect to the planes A–A and B–B aligned along the  $x$  and  $y$  axes. The vectors of contact forces acting on the central particle are denoted as  $\mathbf{f}_c^i$  and their magnitudes as  $f_i, i = 1, \dots, 6$ . The interaction is in the

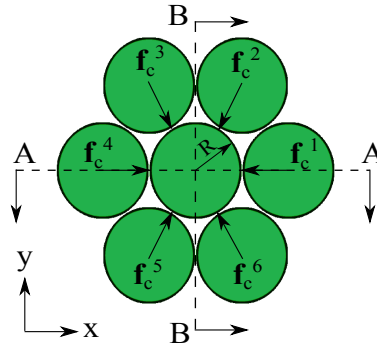


**Figure 3.9.** An HCP unit cell with contact forces and planes of symmetry AA and BB.

normal direction, only, therefore the contact force vectors can be defined in terms of their components as follows:  $\mathbf{f}_c^1 = \begin{bmatrix} -f_1 & 0 \end{bmatrix}^T$ ,  $\mathbf{f}_c^2 = \begin{bmatrix} -f_2/2 & -\sqrt{3}f_2/2 \end{bmatrix}^T$ ,  $\mathbf{f}_c^3 = \begin{bmatrix} f_3/2 & -\sqrt{3}f_3/2 \end{bmatrix}^T$ ,  $\mathbf{f}_c^4 = \begin{bmatrix} f_4 & 0 \end{bmatrix}^T$ ,  $\mathbf{f}_c^5 = \begin{bmatrix} f_5/2 & \sqrt{3}f_5/2 \end{bmatrix}^T$  and  $\mathbf{f}_c^6 = \begin{bmatrix} -f_6/2 & -\sqrt{3}f_6/2 \end{bmatrix}^T$ .

Using Eq. (2.41) determine the volume averaged stress in the central particle under the action of contact forces as follows, first the outer (tensor) product of branch vector  $\mathbf{s}^i$  and force vector  $\mathbf{f}_c^i$  for each particle in contact with the particle at centre is calculated,

$$\mathbf{s}^1 \otimes \mathbf{f}_c^1 = \begin{bmatrix} R \\ 0 \end{bmatrix} \cdot \begin{bmatrix} -f_1 & 0 \end{bmatrix} = \begin{bmatrix} -Rf_1 & 0 \\ 0 & 0 \end{bmatrix} \quad (3.48)$$

$$\mathbf{s}^2 \otimes \mathbf{f}_c^2 = \begin{bmatrix} R/2 \\ \sqrt{3}/2 \end{bmatrix} \cdot \begin{bmatrix} -f_2/2 & -\sqrt{3}f_2/2 \end{bmatrix} = \frac{R}{4} \begin{bmatrix} -f_2 & -\sqrt{3}f_2 \\ -\sqrt{3}f_2 & -3f_2 \end{bmatrix} \quad (3.49)$$

$$\mathbf{s}^3 \otimes \mathbf{f}_c^3 = \begin{bmatrix} -R/2 \\ \sqrt{3}/2 \end{bmatrix} \cdot \begin{bmatrix} f_3/2 & -\sqrt{3}f_3/2 \end{bmatrix} = \frac{R}{4} \begin{bmatrix} -f_3 & \sqrt{3}f_3 \\ \sqrt{3}f_3 & -3f_3 \end{bmatrix} \quad (3.50)$$

$$\mathbf{s}^4 \otimes \mathbf{f}_c^4 = \begin{bmatrix} -R \\ 0 \end{bmatrix} \cdot \begin{bmatrix} f_4 & 0 \end{bmatrix} = \begin{bmatrix} -Rf_4 & 0 \\ 0 & 0 \end{bmatrix} \quad (3.51)$$

$$\mathbf{s}^5 \otimes \mathbf{f}_c^5 = \begin{bmatrix} -R/2 \\ -\sqrt{3}/2 \end{bmatrix} \cdot \begin{bmatrix} f_5/2 & \sqrt{3}f_5/2 \end{bmatrix} = \frac{R}{4} \begin{bmatrix} -f_5 & -\sqrt{3}f_5 \\ -\sqrt{3}f_5 & -3f_5 \end{bmatrix} \quad (3.52)$$

$$\mathbf{s}^6 \otimes \mathbf{f}_c^6 = \begin{bmatrix} R/2 \\ -\sqrt{3}/2 \end{bmatrix} \cdot \begin{bmatrix} -f_6/2 & -\sqrt{3}f_6/2 \end{bmatrix} = \frac{R}{4} \begin{bmatrix} -f_6 & \sqrt{3}f_6 \\ \sqrt{3}f_6 & -3f_6 \end{bmatrix} \quad (3.53)$$

due to symmetry along plane B–B,  $f_1 = f_4, f_2 = f_3, f_5 = f_6$  and along plane A–A,  $f_2 = f_6, f_5 = f_3$ . Therefore, it can be implied that Eqs. (3.48), (3.51) can be written in terms of force magnitude  $f_1$  and Eqs. (3.49), (3.50), (3.52) and (3.53) can be written in terms of force magnitude  $f_2$ . After rewriting and substituting the summation of Eqs. (3.48) – (3.53) in Eq. (2.41),

$$\boldsymbol{\sigma}_p = \frac{1}{V_p} \sum_{i=1}^{n_p} \mathbf{s}^i \otimes \mathbf{f}_c^i = -\frac{1}{\pi Rl} \begin{bmatrix} 2f_1 + f_2 & 0 \\ 0 & 3f_2 \end{bmatrix} \quad (3.54)$$

where,  $V_p = \pi R^2 l$ , is the volume of a 2D disc particle with  $l$  being its depth. Hence, the stress tensor  $\tilde{\boldsymbol{\sigma}}_p$  in vector form (cf. Eq. (2.47)) for this case becomes,

$$\tilde{\boldsymbol{\sigma}}_p = \begin{bmatrix} \sigma_{xx} \\ \sigma_{yy} \end{bmatrix} = -\frac{1}{\pi Rl} \begin{bmatrix} 2f_1 + f_2 \\ 3f_2 \end{bmatrix} \quad (3.55)$$

and rewriting in a simplified form,

$$\tilde{\boldsymbol{\sigma}}_p = \begin{bmatrix} \sigma_{xx} \\ \sigma_{yy} \end{bmatrix} = -\frac{1}{\pi Rl} \begin{bmatrix} 2 & 1 \\ 0 & 3 \end{bmatrix} \begin{bmatrix} f_1 \\ f_2 \end{bmatrix} \quad (3.56)$$

which relates the stress components  $\sigma_{xx}, \sigma_{yy}$  in current time step  $n$  and current iteration  $k$  to the contact forces  $f_1, f_2$  from the current time step  $n$  and previous iteration  $k - 1$ , i.e.

$$\begin{bmatrix} \sigma_{xx}^{(n,k)} \\ \sigma_{yy}^{(n,k)} \end{bmatrix} = -\frac{1}{\pi Rl} \begin{bmatrix} 2 & 1 \\ 0 & 3 \end{bmatrix} \begin{bmatrix} f_1^{(n,k-1)} \\ f_2^{(n,k-1)} \end{bmatrix} \quad (3.57)$$

2. Calculate the particle strain components at time step  $n$  and  $k$ -th iteration for the assumed plane-strain condition

$$\begin{bmatrix} \varepsilon_{xx}^{(n,k)} \\ \varepsilon_{yy}^{(n,k)} \end{bmatrix} = \frac{1 + \nu_p}{E_p} \begin{bmatrix} (1 - \nu_p) & -\nu_p \\ -\nu_p & (1 - \nu_p) \end{bmatrix} \begin{bmatrix} \sigma_{xx}^{(n,k)} \\ \sigma_{yy}^{(n,k)} \end{bmatrix} \quad (3.58)$$

3. The particle overlaps in direction of contact forces  $\mathbf{f}_c^1$  and  $\mathbf{f}_c^2$  are evaluated by considering an HCP unit cell from an infinite lattice of disc particles with equal radii  $R$  as in the previous step. The individual particles of HCP unit cell are now numbered  $0, \dots, 6$  as shown in Fig. 3.10 and assumed to be in plane strain condition. The 2D strains in the particle at the centre, i.e. particle no. 0, are represented by the components  $\varepsilon_{xx}$  and  $\varepsilon_{yy}$ . The initial (standard DEM) overlap between circular disks is denoted by  $h_i$  for contact interaction  $0 - i$ , where  $i = 1, \dots, 6$ . The aim is to determine the overlaps  $h_{ci}$  between the particles deformed under the known contact forces  $\mathbf{f}_c^i$ . Since, due to symmetry, the particle stresses have been expressed in terms of the magnitudes of two contact forces,  $\mathbf{f}_c^1$  and  $\mathbf{f}_c^2$ , it will be necessary to determine the corresponding overlaps  $h_{c1}$  and  $h_{c2}$ , only. The overlaps are determined as follows,

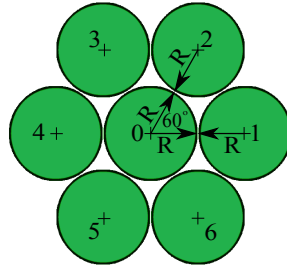


**Figure 3.10.** An HCP unit cell with individual particles numbered 0 – 6.

For the contact between particles 0 and 1 as shown in Fig. 3.10, the unit normal vector  $\mathbf{n}_c^1$  is given as,

$$\mathbf{n}_c^1 = [1, 0]^T \quad (3.59)$$

The branch vector  $\mathbf{s}^1$  i.e. the vector connecting centre of the particle 0 and contact point becomes,

$$\mathbf{s}^1 = \mathbf{n}_c^1 R = [R, 0]^T \quad (3.60)$$

Displacement vector for particle 0 at the contact point due to force  $\mathbf{f}_c^i$  in accordance with Eq. (2.52) can be written as,

$$\mathbf{u}_c = \boldsymbol{\varepsilon}_p \mathbf{s}^1 \quad (3.61)$$

or in matrix form,

$$\mathbf{u}_c = \begin{bmatrix} \varepsilon_{xx} & 0 \\ 0 & \varepsilon_{yy} \end{bmatrix} \begin{bmatrix} R \\ 0 \end{bmatrix} \quad (3.62)$$

The modified overlap  $h_{c1}$  between particles 0 and 1 is given as follows, cf. Eq.(2.53),

$$h_{c1} = h_1 + 2R\epsilon_{xx} \quad (3.63)$$

Similarly, for the contact between particles 0 and 2 as shown in Fig. 3.10, the unit normal vector takes the form,

$$\mathbf{n}_c^2 = \left[ 1/2, \sqrt{3}/2 \right]^T \quad (3.64)$$

resulting in branch vector,

$$\mathbf{s}^2 = \mathbf{n}_c^2 R = \left[ R/2, R\sqrt{3}/2 \right]^T \quad (3.65)$$

and displacement vector,

$$\mathbf{u}_c = \begin{bmatrix} \epsilon_{xx} & 0 \\ 0 & \epsilon_{yy} \end{bmatrix} \begin{bmatrix} R/2 \\ R\sqrt{3}/2 \end{bmatrix} \quad (3.66)$$

hence, the modified overlap  $h_{c2}$  between particles 0 and 2 is as follows cf. Eq. (2.53),

$$h_{c2} = h_2 + \frac{R}{2}(\epsilon_{xx} + 3\epsilon_{yy}) \quad (3.67)$$

Therefore, the modified normal overlaps in vector form can be written as follows,

$$\begin{bmatrix} h_{c1} \\ h_{c2} \end{bmatrix} = \begin{bmatrix} h_1 \\ h_2 \end{bmatrix} + R \begin{bmatrix} 2\epsilon_{xx} \\ (\epsilon_{xx} + 3\epsilon_{yy})/2 \end{bmatrix} \quad (3.68)$$

$$= \begin{bmatrix} h_1 \\ h_2 \end{bmatrix} + R \begin{bmatrix} 2 & 0 \\ 1/2 & 3/2 \end{bmatrix} \begin{bmatrix} \epsilon_{xx} \\ \epsilon_{yy} \end{bmatrix} \quad (3.69)$$

$$= \begin{bmatrix} h_1 \\ h_2 \end{bmatrix} + \frac{R}{2} \begin{bmatrix} 4 & 0 \\ 1 & 3 \end{bmatrix} \begin{bmatrix} \epsilon_{xx} \\ \epsilon_{yy} \end{bmatrix} \quad (3.70)$$

which relates the modified overlaps  $h_{c1}$ ,  $h_{c2}$  in current time step  $n$  and current iteration  $k$  to the strains  $\epsilon_{xx}$ ,  $\epsilon_{yy}$  from the current time step  $n$  and previous iteration  $k - 1$ , i.e.

$$\begin{bmatrix} h_{c1}^{(n,k)} \\ h_{c2}^{(n,k)} \end{bmatrix} = \begin{bmatrix} h_1 \\ h_2 \end{bmatrix} + \frac{R}{2} \begin{bmatrix} 4 & 0 \\ 1 & 3 \end{bmatrix} \begin{bmatrix} \epsilon_{xx}^{(n,k)} \\ \epsilon_{yy}^{(n,k)} \end{bmatrix} \quad (3.71)$$

4. The new values for magnitudes of contact forces are calculated as follows

$$\begin{bmatrix} f_1^{(n,k)} \\ f_2^{(n,k)} \end{bmatrix} = -k_n \begin{bmatrix} h_{c1}^{(n,k)} \\ h_{c2}^{(n,k)} \end{bmatrix} \quad (3.72)$$

Substituting Eqs. (3.71) and (3.58) into Eq. (3.72) and taking into account (3.57) one obtains

$$\begin{bmatrix} f_1^{(n,k)} \\ f_2^{(n,k)} \end{bmatrix} = -k_n \begin{bmatrix} h_1 \\ h_2 \end{bmatrix} + \frac{k_n(1+\nu_p)}{\pi E_p l} \begin{bmatrix} 4(1-\nu_p) & 2(1-4\nu_p) \\ (1-4\nu_p) & (5-8\nu_p) \end{bmatrix} \begin{bmatrix} f_1^{(n,k-1)} \\ f_2^{(n,k-1)} \end{bmatrix} \quad (3.73)$$

The recursive relationship (3.73) is a particular form of the relationship (3.8). The relationship between successive differences corresponding to the relationship (3.10) can be easily obtained as:

$$\begin{bmatrix} f_1^{(n,k+1)} - f_1^{(n,k)} \\ f_2^{(n,k+1)} - f_2^{(n,k)} \end{bmatrix} = \frac{k_n(1+\nu_p)}{\pi E_p l} \begin{bmatrix} 4(1-\nu_p) & 2(1-4\nu_p) \\ (1-4\nu_p) & (5-8\nu_p) \end{bmatrix} \begin{bmatrix} f_1^{(n,k)} - f_1^{(n,k-1)} \\ f_2^{(n,k)} - f_2^{(n,k-1)} \end{bmatrix} \quad (3.74)$$

The iteration matrix  $\mathbf{B}$  now takes the form:

$$\mathbf{B} = \frac{k_n(1+\nu_p)}{\pi E_p l} \begin{bmatrix} 4(1-\nu_p) & 2(1-4\nu_p) \\ (1-4\nu_p) & (5-8\nu_p) \end{bmatrix} \quad (3.75)$$

5. In order to evaluate the convergence criterion (3.13) the spectral radius of matrix  $\mathbf{B}$  is calculated using Eq. (3.14), for which the set of eigenvalues  $\Phi(\mathbf{B})$  of the iteration matrix  $\mathbf{B}$  given by Eq. (3.75) is obtained as:

$$\Phi(\mathbf{B}) = \left\{ \frac{3k_n(1+\nu_p)}{\pi E_p l}, \frac{6k_n(1+\nu_p)(1-2\nu_p)}{\pi E_p l} \right\} \quad (3.76)$$

Now, it can be noticed that the maximum absolute eigenvalue,  $\max |\lambda|$ , within the set of eigenvalues in Eq.(3.76) depends upon the particle Poisson's ratio  $\nu_p$ . Therefore,

$$\rho(\mathbf{B}) = \max_{\lambda \in \Phi(\mathbf{B})} |\lambda| = \begin{cases} \frac{3k_n(1+\nu_p)}{\pi E_p l} & \text{for } \nu_p \geq 0.25 \\ \frac{6k_n(1+\nu_p)(1-2\nu_p)}{\pi E_p l} & \text{for } \nu_p < 0.25 \end{cases} \quad (3.77)$$

Hence it can be concluded that the convergence criterion for the iterative scheme is:

$$\begin{cases} \frac{3k_n(1 + \nu_p)}{\pi E_p l} < 1 & \text{for } \nu_p \geq 0.25 \\ \frac{6k_n(1 + \nu_p)(1 - 2\nu_p)}{\pi E_p l} < 1 & \text{for } \nu_p < 0.25 \end{cases} \quad (3.78)$$

The convergence criteria obtained for the HCP configuration, i.e. Eq. (3.78), have been used for comparison with the stability limit estimated in numerical simulations. Numerical studies of the stability limit for the HCP configuration has been conducted in a manner similar to the SC configuration as described in section 3.5. An unconfined uniaxial compression of a rectangular sample has been simulated using the DDEM formulation. A total of 110 same sized, bonded disc particles are arranged in the HCP pattern to discretize the rectangular specimen as shown in Fig. 3.8a. Each particle is assumed to have radius  $R = 1$  mm, which results in sample size, height  $H = 27.71$  mm by width  $A = 12$  mm. Microscopic properties and loading conditions are kept same as that for the SC configuration in section 3.5. The total maximum value force  $F$  has achieved is 60 kN in this case, cf. Fig. 3.8a.

The numerical limit value of particle Young's modulus  $E_p$  for a given particle Poisson's ratio  $\nu_p$  has been obtained in a manner similar to that for the simple cubic configuration – analysing the response of the specimen. The analysis of the selected case is presented in Fig. 3.11, showing the plots of the total displacement in loading direction ( $y$  axis) with respect to time for a fixed particle Poisson's ratio  $\nu_p = 0.35$  and three different

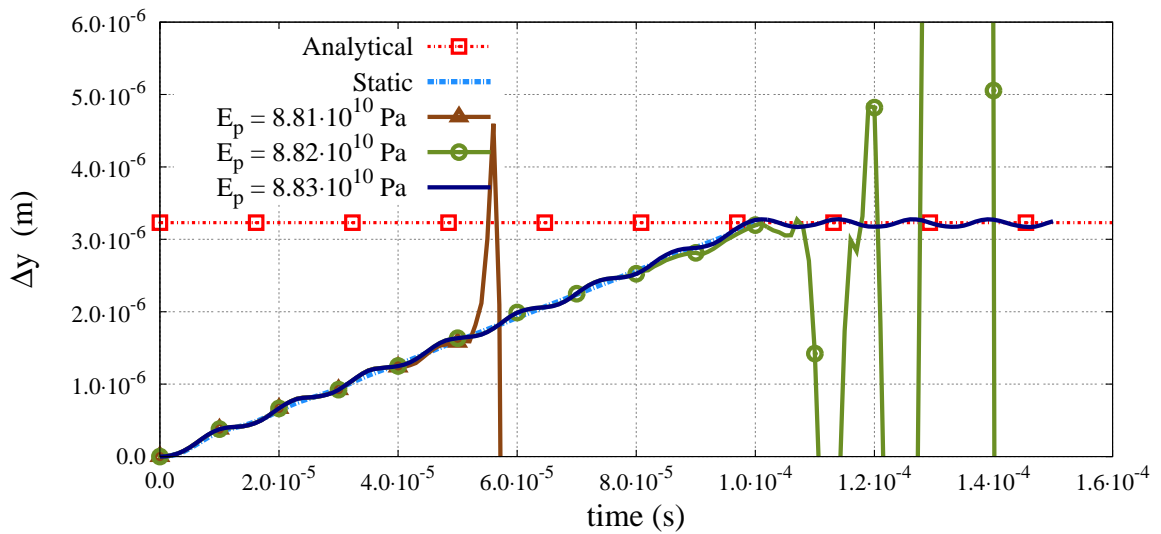


**Figure 3.11.** Comparison of displacement time curves for the unconfined uniaxial compression of HCP specimen for a stable solution:  $E_p = 8.83 \cdot 10^{10}$  Pa ( $k_n/E_p = 0.792$ ) and unstable solutions:  $E_p = 8.82 \cdot 10^{10}$  Pa ( $k_n/E_p = 0.793$ ) and  $E_p = 8.81 \cdot 10^{10}$  Pa ( $k_n/E_p = 0.795$ ).

Young's moduli,  $E_p = 8.81 \cdot 10^{10}$  Pa,  $E_p = 8.82 \cdot 10^{10}$  Pa and  $8.83 \cdot 10^{10}$  Pa. As it can be observed in Fig. 3.11 the particle Young's modulus  $E_p = 8.83 \cdot 10^{10}$  Pa leads to a stable numerical solution characterized by small oscillations (no damping has been used) about the static solution. The theoretical value of total displacement is evaluated considering an equivalent HCP lattice with the effective normal contact stiffness  $k$  between the particles in contact obtained from Eq. (2.67). Contrary to the case of  $E_p = 8.83 \cdot 10^{10}$  Pa, an unstable behaviour is obtained with the particle Young's moduli  $E_p = 8.81 \cdot 10^{10}$  Pa and  $E_p = 8.82 \cdot 10^{10}$  Pa. Hence, the particle Young's modulus  $E_p = 8.83 \cdot 10^{10}$  Pa or  $k_n/E_p = 0.793$  can be considered as the stability limit for the particle Poisson's ratio  $\nu_p = 0.35$ . Similarly, the stability limit in terms of microscopic elastic parameters has been determined for other values of particle Poisson's ratios.

**Table 3.3.** Comparison between analytical predictions and numerical results for the HCP configuration with different particle Poisson's ratio  $\nu_p$  and a constant normal contact stiffness  $k_n = 7 \cdot 10^{10}$  N/m.

$\nu_p$	$E_p$ (Pa)	$k_n/E_p$ (analytical)	$k_n/E_p$ (numerical)
0.05	$1.23 \cdot 10^{11}$	0.554	0.569
0.10	$1.14 \cdot 10^{11}$	0.595	0.614
0.15	$1.04 \cdot 10^{11}$	0.650	0.673
0.20	$9.32 \cdot 10^{10}$	0.727	0.751
0.22	$8.85 \cdot 10^{10}$	0.766	0.791
0.25	$8.24 \cdot 10^{10}$	0.838	0.850
0.30	$8.51 \cdot 10^{10}$	0.806	0.823
0.35	$8.83 \cdot 10^{10}$	0.776	0.793
0.40	$9.16 \cdot 10^{10}$	0.748	0.764
0.45	$9.48 \cdot 10^{10}$	0.722	0.738

The results of the numerical stability analysis are given in Table 3.3 in comparison with the theoretical predictions of the convergence limit according to Eq. (3.78). It can be noticed that the respective results are very close to each other. A graphical representation of the stable (convergent) and unstable (non-convergent) zones in terms of microscopic properties is shown in Fig. 3.12. A very good agreement between the analytical numerical results can be observed. This proves that the convergence criterion for the iterative solution determines also the stability of the explicit DDEM algorithm.

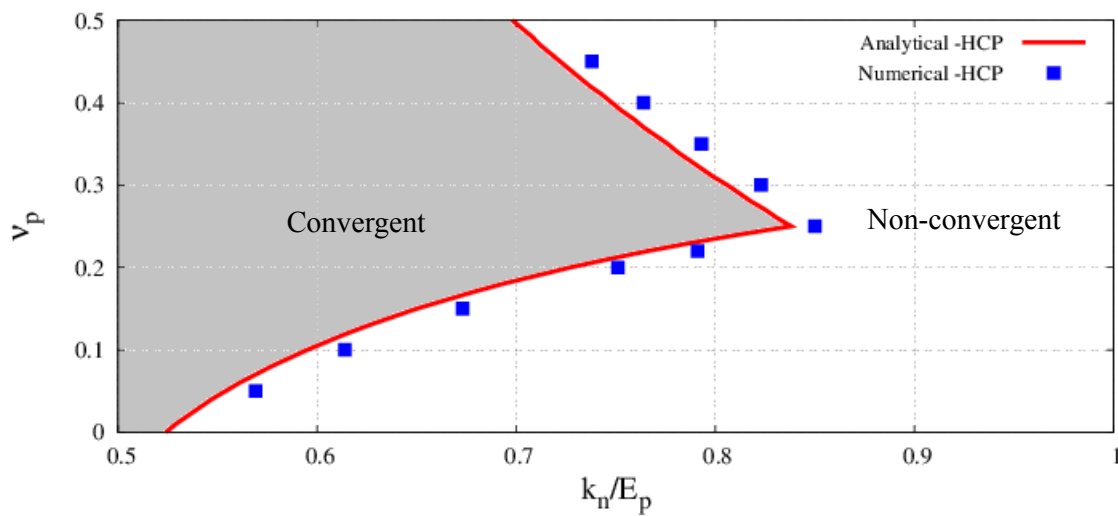


**Figure 3.12.** Comparison of the numerical stability and analytical convergence limits for HCP configuration for constant normal stiffness  $k_n = 7 \cdot 10^{10}$  N/m.

Similarly to the SC configuration, stability limit on the time step in the standard DEM and DDEM has been studied by numerical simulations. The critical time step for the HCP configuration has been determined to analyse the stability of the solution changing the time step. Figure 3.13 shows the plots of the axial displacement w.r.t. time obtained in the standard DEM and DDEM simulations with two different but close time steps,  $\Delta t = 2.4567 \cdot 10^{-7}$  s and  $\Delta t = 2.5166 \cdot 10^{-7}$ . It can be clearly seen in Fig. 3.13 that in both standard and deformable DEM case time step  $\Delta t = 2.4567 \cdot 10^{-7}$  s leads to a stable solution converging to the corresponding analytical one. With even a slightly higher time step  $\Delta t = 2.5166 \cdot 10^{-7}$  s, the simulations rapidly goes into the unstable mode. Hence, as observed previously in SC configuration case, also in HCP configuration the critical time step in the deformable DEM model remains the same as in the standard DEM model.

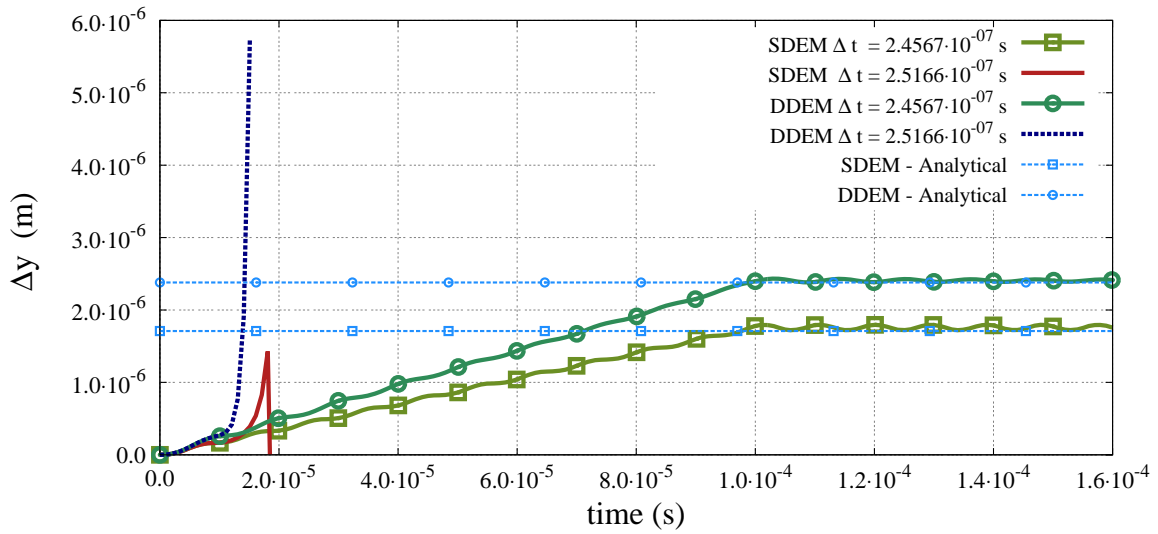


**Figure 3.13.** Comparison of displacement–time curves for the unconfined uniaxial compression of HCP specimen for standard DEM and DDEM stable ( $\Delta t = 2.4567 \cdot 10^{-7}$  s) and unstable ( $\Delta t = 2.5166 \cdot 10^{-7}$  s) solutions. For DDEM model, particle Young’s moduli  $E_p = 2 \cdot 10^{11}$  Pa, particle Poisson ratio  $\nu_p = 0.35$  is used.

## Summary

The investigations presented in this chapter have shown that there are two restrictions on the stability of the DDEM algorithm implemented in the explicit dynamics framework. Except for the limit imposed on the time step in the explicit time integration, the stability of the DDEM is controlled by the convergence limit of the iterative solution of an implicit relationship between contact forces and particle displacements. The stability limits obtained in numerical simulations for problems with regular SC and HCP coincide very well with the convergence limits deduced theoretically.

The convergence criterion and consequently the stability limits for the DDEM are given in terms of microscopic properties, namely, the particle Poisson’s ratio, the particle Young’s modulus and the normal contact stiffness. The respective limiting relationships should be taken into account in the DDEM model calibration based on the micro-macro relationships presented in [127]. The other restriction on the stability of the DDEM, the critical time step of the explicit time integration scheme has been shown to remain the same as in the standard DEM formulation. The studies have shown that the DDEM algorithm is robust and stable provided the stability limits are respected. The stability limits can be assessed very well using the theoretical criteria derived in this chapter.

# Chapter 4

## Micro-macro relationships for the deformable discrete element model

### Introduction

Microscopic quantities and relationships used in the discrete element method can be transferred to the macroscopic scale giving an equivalent macroscopic material model. In the macroscale, we deal with equivalent continuous medium characterized by fields of macroscopic variables, the stress tensor  $\bar{\sigma}_{ij}$  and the strain tensor  $\bar{\varepsilon}_{ij}$ . The macroscopic stress and strain tensors are related to microscopic quantities with a certain constitutive relationship. The present chapter is aimed to establish equivalent constitutive relationships for the DDEM in the elastic range. Firstly, the averaging procedures adopted in this work to determine macroscopic stress and strain tensor for a particulate sample has been described. Next, the constitutive relationship between microscopic material parameters and macroscopic elastic parameters obtained via averaging procedures has been established using the dimensionless analysis. Further on, constitutive parameters based on Voigt hypothesis has been described for analytical verification of the dimensionless relationships. Subsequently, energy balance equations for a discrete particle assembly has been framed, which provides an additional method to verify the DDEM. First a simple test case namely, a rectangular configuration with simple cubic particle arrangement, have been used to compare the numerical results with derived analytical results and those obtained with finite element method (FEM) simulations. Upon verification of DDEM model, the dimensionless constitutive relationships between macroscopic and microscopic elastic parameters have been established. Next, the constitutive relationships are established for a more representative packing with particles of non-uniform size distribution. The results presented within this chapter have been published in [127].

## 4.1 Macroscopic stress and strain tensor

Macroscopic average stress  $\bar{\sigma}_{ij}$  in the specimen can be calculated by averaging particle stresses  $(\sigma_p)_{ij}$  calculated according to Eq. (2.45) in the specimen volume  $V$ , cf. [82]:

$$\bar{\sigma} = \frac{1}{V} \sum_{p \in V} V_p (\sigma_p)_{ij}. \quad (4.1)$$

where  $V_p$  is the particle volume. Inserting Eq. (2.45) into Eq. (4.1) one gets

$$\bar{\sigma} = \frac{1}{2V} \sum_{p \in V} \sum_{c=1}^{n_{pc}} (s_i^c F_j^c + F_i^c s_j^c), \quad (4.2)$$

which can be presented in an equivalent form as [73]:

$$\bar{\sigma} = \frac{1}{2V} \sum_{c=1}^{N_c} (L_i^c F_j^c + F_i^c L_j^c), \quad (4.3)$$

where the summation is over the number of all the contacts  $N_c$  in the volume  $V$ , and  $L_i^c$  is the so called branch vector connecting the centres of two particles in the contact  $c$ .

The macroscopic strain tensor for the discrete element assembly has been calculated using the procedure proposed by Bagi [3]. Averaging is performed over a triangular (in 3D tetrahedra would be used) mesh generated over the centres of the particles forming the specimen. This is a two level averaging procedure. First, a constant strain  $\varepsilon_{ij}^k$  in all the triangles are determined using the formula derived from the averaging equation:

$$\varepsilon_{ij}^k = \frac{1}{S_k} \int_{S_k} \varepsilon_{ij} dS, \quad (4.4)$$

where  $S_k$  is the area of an elementary cell.

Applying the divergence theorem the surface integral in Eq. (4.4) can be transformed into the line integral

$$\int_{S_k} \varepsilon_{ij} dS = \frac{1}{2} \int_{L_k} (u_i n_j + n_i u_j) dL, \quad (4.5)$$

where  $L_k$  is the closed boundary of the triangular element,  $u_i$  – the displacement field and  $n_i$  – the unit normal vector outward to the element. The line integral in Eq. (4.5) is evaluated in terms of nodal displacements and geometric parameters characterizing the triangular element. The details of this procedure can be found in [3]. Having determined the strain  $\varepsilon_{ij}^k$  in each element the average strain tensor in the whole specimen is obtained by the weighted averaging

$$\bar{\varepsilon}_{ij} = \frac{1}{S} \sum_k S_k \varepsilon_{ij}^k. \quad (4.6)$$

## 4.2 Dimensionless constitutive relationships

A suitable framework for the analysis of micro-macro constitutive relationships in the DEM is provided by the dimensional analysis [35, 53, 158]. The dimensionless functional relationships for the Young's modulus  $E$  and the Poisson's ratio  $\nu$  in the standard DEM can be assumed in the following form, cf. [53, 158]:

$$E = k_n \Phi_E \left( \frac{k_t}{k_n}, n \right), \quad (4.7)$$

$$\nu = \Phi_\nu \left( \frac{k_t}{k_n}, n \right), \quad (4.8)$$

The elastic constants are assumed to be functions of the ratio of the contact tangential and normal stiffness  $k_t/k_n$  and the porosity  $n$ . In the deformable DEM two additional parameters, namely, the particle Poisson's ratio  $\nu_p$  and the particle Young's modulus  $E_p$  should be included in the dimensional analysis. Now, the dimensionless relationships can be written as follows:

$$E = k_n \Phi_E \left( \frac{k_t}{k_n}, \frac{k_n}{E_p}, \nu_p, n \right), \quad (4.9)$$

$$\nu = \Phi_\nu \left( \frac{k_t}{k_n}, \frac{k_n}{E_p}, \nu_p, n \right), \quad (4.10)$$

The specific form of the relationships (4.9) and (4.10) will be obtained further on by performing numerical simulations of the unconfined uniaxial compression test.

Elastic properties can be defined alternatively in terms of the bulk and shear moduli,  $K$  and  $G$ , respectively, related to the Poisson's ratio  $\nu$  and the Young's modulus  $E$  by

$$K = \frac{E}{3(1 - 2\nu)}, \quad (4.11)$$

$$G = \frac{E}{2(1 + \nu)}. \quad (4.12)$$

The respective dimensionless relationships for the bulk and shear moduli can be written analogously to Eqs. (4.9) and (4.10) as follows

$$K = k_n \Phi_K \left( \frac{k_t}{k_n}, \frac{k_n}{E_p}, \nu_p, n \right), \quad (4.13)$$

$$G = k_n \Phi_G \left( \frac{k_t}{k_n}, \frac{k_n}{E_p}, \nu_p, n \right), \quad (4.14)$$

The new formulation is expected to manifest its advantages in the enhancement of the Poisson's effect, therefore the results will be presented mainly in terms of the Poisson's ratio  $\nu$  and the Young's modulus  $E$ , however, the consistency of the elastic constants

will be verified for selected cases by a comparison of the bulk and shear moduli,  $K$  and  $G$ , obtained from the relationships (4.9) and (4.10) by means of Eqs. (4.12) and (4.11) with the relationships (4.13) and (4.14) determined directly by simulation of the biaxial isotropic compression and shear tests.

### 4.3 Macroscopic constitutive parameters based on the Voigt hypothesis

Using the uniform strain Voigt's hypothesis for the assembly of cylindrical discs of the same size and same material properties with isotropic packing structure the analytical formulae for the elastic moduli can be obtained in the following form [8, 79]:

$$E = \frac{4N_c R^2 k_n}{V} \cdot \frac{k_n + k_t}{3k_n + k_t} \quad (4.15)$$

$$\nu = \frac{k_n - k_t}{3k_n + k_t} \quad (4.16)$$

$$K = \frac{N_c R^2}{V} k_n \quad (4.17)$$

$$G = \frac{N_c R^2 (k_n + k_t)}{2V} \quad (4.18)$$

where  $N_c$  is the total number of inter-particle contacts in the volume  $V$ ,  $R$  is the particle radius,  $k_n$  and  $k_t$  are the contact stiffness in the normal and tangential direction, respectively. The relationships (4.15)–(4.18) will be used to verify respective dimensionless relationships obtained numerically by means of the standard DEM.

### 4.4 Micro-macro relationships for DDEM model with regular configuration

An unconfined uniaxial compression of a rectangular specimen discretized with bonded discs as it is shown in Fig. 4.1a has been simulated using the standard DEM and DDEM formulation. It has been assumed that the discrete model represents an elastic solid material. The rectangular sample contained 180 (9 by 20) disc elements each of radius  $R = 1$  mm, resulting in a total height  $H = 40$  mm and a width  $A = 18$  mm. Microscopic properties are as follows: density  $\rho = 2000$  kg/m<sup>3</sup>, normal contact stiffness  $k_n = 7 \cdot 10^{10}$  N/m. The problem has been investigated for different values of the particle Poisson's ratio  $\nu_p$  and the particle Young's modulus  $E_p$ . A comparison with the FEM model (Fig. 4.1b) for an equivalent continuous body is also provided in order to verify the original formulation of the discrete element methods with deformable particles.

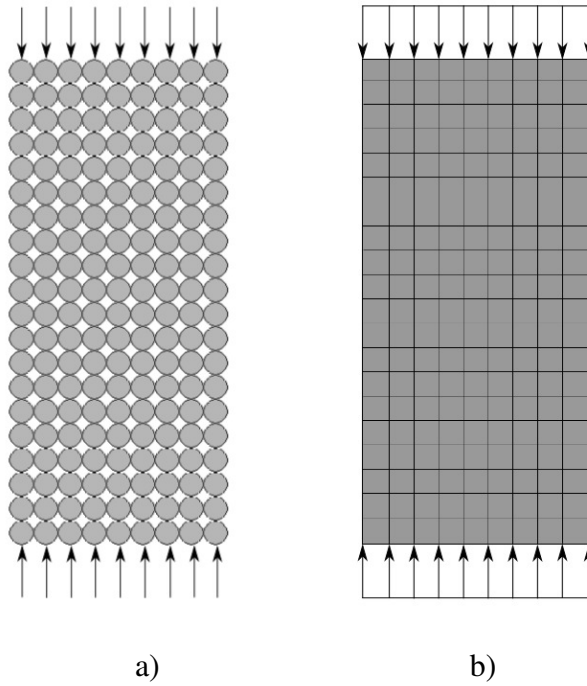


**Figure 4.1.** Unconfined uniaxial compression of a rectangular specimen – a) DEM model b) equivalent FEM model.

Additionally, comparisons are made with an analytical solution of a quasistatic problem obtained on the basis of the theoretical analysis presented in Sec. 2.8.

In simulations, the sample has been uniaxially compressed under a uniform load represented by equal forces applied at the particles in the top and bottom row as shown in Fig. 4.1a. The particles in the middle column have been constrained horizontally to avoid any buckling effects. The loading has been applied by increasing each force linearly from 0 to 10 kN during 0.1 ms and then kept constant during 0.05 ms. The total maximum force  $f$  of 90 kN has been achieved.

Figure 4.1b shows a 2D FEM model of an equivalent continuous body (a bar) with the same dimensions as those of the standard DEM model,  $H = 40$  mm by  $A = 18$  mm. A regular mesh of 9 by 20 elements is used to discretize the continuous body. Taking porosity of the DEM model into account the equivalent density for the FEM model is  $\rho_{FEM} = 1570.8$  kg/m<sup>3</sup>. The total load of 90 kN distributed over an area of 0.018 m<sup>2</sup> in DEM model is applied in terms of pressure 5 MPa on both the ends in the FEM model. The FEM simulations have been performed using the ANSYS software.

Figure 4.2 shows the results of the simulations for the standard DEM and equivalent FEM models. The specimen response has been characterized by the average axial strain  $\varepsilon_{yy}$  evaluated as the ratio  $\Delta H/H$ , where  $\Delta H$  is the change of the sample height. The axial strain has been plotted as a function of time for the undamped and damped models. The solution without damping is characterized by vibrations which are attenuated when

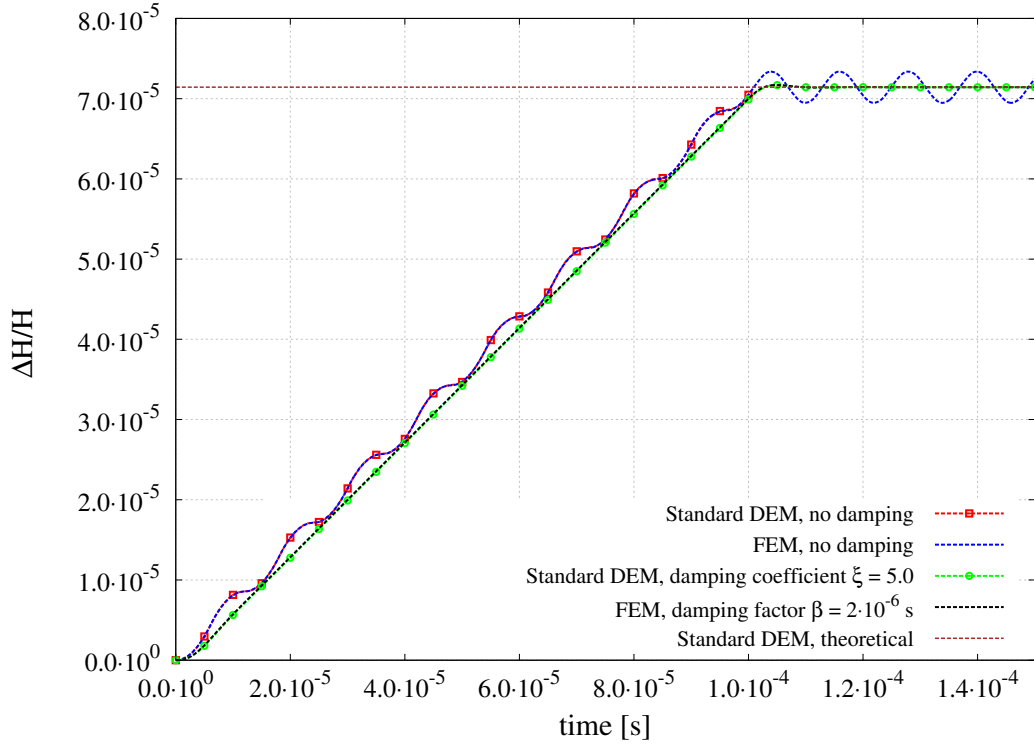


**Figure 4.2.** Axial strain as a function of time for undamped and damped models – comparison of the standard DEM solution with the equivalent FEM solution.

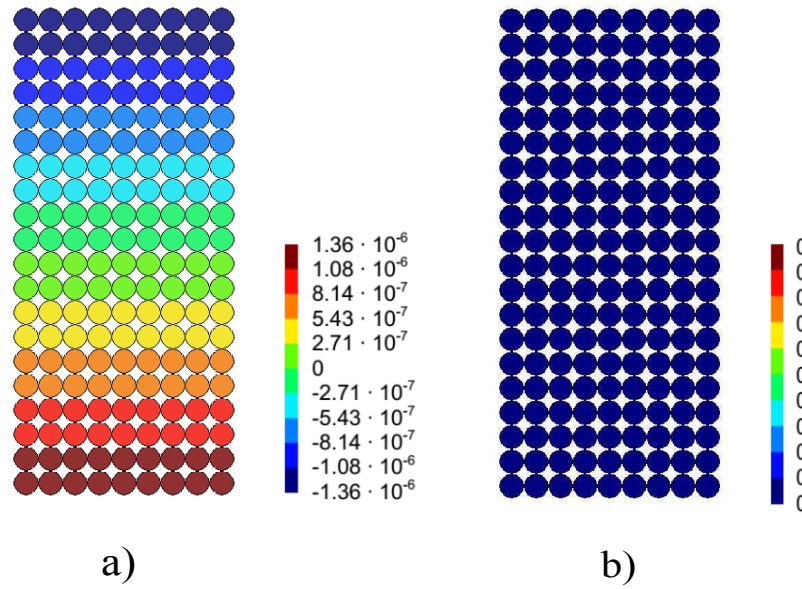
adequate damping is introduced. Different damping values have been tried in order to find the damping which ensures quasistatic loading conditions and a linear response. The standard DEM damped solution presented in Fig. 4.2 has been obtained with the damping coefficient  $\xi^n = 5$ . The damping coefficient  $\xi^n$  introduced in Eq. (2.35) defines the damping parameter  $c_n$  with respect to the critical damping  $c_n^{cr}$  for a pair of particles given by Eq. (2.37). The applied damping allows obtaining the steady state solution. The axial deformation corresponding to the steady state solution in Fig. 4.2 agrees very well with the theoretical prediction based on the methodology presented above for obtaining the analytical solution of the quasistatic problem.

Figure 4.3 shows the results obtained with the standard DEM formulation in the form of the contours of displacements along the  $y$  and  $x$  axes at the final stage. It can be seen that all the elements have zero  $x$  displacements. This means that the macroscopic effective Poisson's ratio is zero in this model under the loading along the  $y$  axis. The zero Poisson's ratio has been assumed for the FEM model equivalent to the standard DEM model. The equivalent Young's modulus assumed for the FEM model has been evaluated as the ratio

$$E_{FEM} = E_{DEM} = \frac{\Delta\sigma_{yy}}{\Delta\varepsilon_{yy}} \quad (4.19)$$

where the stress and strain increments

$$\Delta\sigma_{yy} = \frac{\Delta f}{AL}, \quad \Delta\varepsilon_{yy} = \frac{\Delta H}{H} \quad (4.20)$$



**Figure 4.3.** Simulation results obtained with the damped model using the standard DEM formulation – contours of displacements (in meters) along: a) the  $y$ -axis, b) the  $x$ -axis at  $t = 0.15$  ms.

have been calculated for the range of the load producing a linear response, namely from 0.4 to 0.8 of the maximum load  $f = 90$  kN. The stresses have been obtained taking  $A = 0.018$  m and  $L = 1$  m. The equivalent Young's modulus obtained is  $E_{DEM} = 69.995$  GPa. The FEM simulations have been performed without and with damping. The damping in the FEM code is of Rayleigh type:

$$\mathbf{C} = \alpha \mathbf{M} + \beta \mathbf{K} \quad (4.21)$$

where  $\mathbf{C}$  is the damping matrix,  $\mathbf{M}$  – the mass matrix,  $\mathbf{K}$  – the stiffness matrix and  $\alpha$  and  $\beta$  – Rayleigh damping coefficients. The response obtained with the FEM model has been compared with the standard DEM solution in Fig. 4.2. A perfect agreement between the two numerical models for both the undamped and damped solutions can be easily noticed. The damped FEM solution has been obtained with the Rayleigh damping coefficients  $\alpha = 0$  and  $\beta = 2 \cdot 10^{-6}$  s. The damping coefficients ensuring quasistatic response in the DEM and FEM models have been used in further simulations.

Further simulations have comprised selected cases of the DDEM models with different particle elastic properties and the FEM models with the properties equivalent to the analysed DDEM models. Figure 4.4 shows the results of the simulations for the undamped and damped DDEM models with the elastic particle properties defined by the Young's modulus  $E_p = 2 \cdot 10^{11}$  Pa and Poisson's ratio  $\nu_p = 0.35$ . The solution with zero damping is characterized by vibrations with a period longer than that of the standard DEM model in Fig. 4.2 which indicates a lower stiffness. This is also confirmed by a higher axial strain achieved under the same loading. The response of the damped model

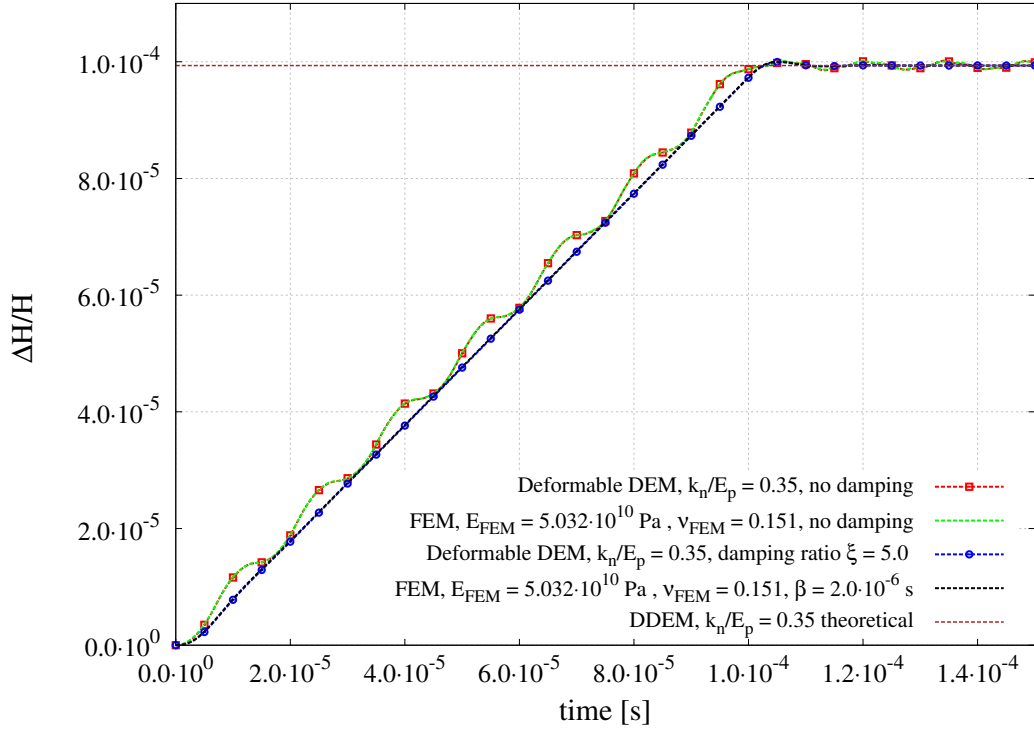


**Figure 4.4.** Axial strain as a function of time for undamped and damped models – comparison of the DDEM solution (elastic properties:  $\nu_p = 0.35$ ,  $E_p = 2 \cdot 10^{11}$  Pa) with the equivalent FEM solution.

is close to linear which indicates that the quasistatic conditions have been reproduced correctly. The steady solution for the damped model is in a very good agreement with the theoretical prediction according to the analytical solution presented before. Figures 4.5a and 4.5b present the contours of  $x$  and  $y$  displacements at the steady state obtained for this case. One can notice non-zero displacements in the  $x$  direction which implies a non-zero Poisson's ratio. This shows that the new formulation allows capturing the Poisson's effect even in such configuration of discs. This confirms new capabilities of the DDEM formulation with respect to the standard DEM.

The results obtained with the DDEM model have been used to determine the equivalent effective macroscopic properties of the FEM model. The effective Young's modulus  $E_{FEM}$  has been evaluated according to Eqs. (4.19) and (4.20). The effective Poisson's ratio has been determined as

$$\nu_{DDEM} = \nu_{FEM} = -\frac{\Delta\varepsilon_{xx}}{\Delta\varepsilon_{yy}} \quad (4.22)$$

where  $\Delta\varepsilon_{xx}$  has been determined from the lateral displacements of the particles on the sides of the sample. The results of the FEM simulations with the elastic constants  $E_{FEM} = 50.32$  GPa and  $\nu_{FEM} = 0.151$  evaluated in this way have been shown in Figs. 4.4 and 4.5c, d. The response of the equivalent FEM model agrees perfectly with the DDEM solution presented in Fig. 4.4 for both the undamped and damped case.

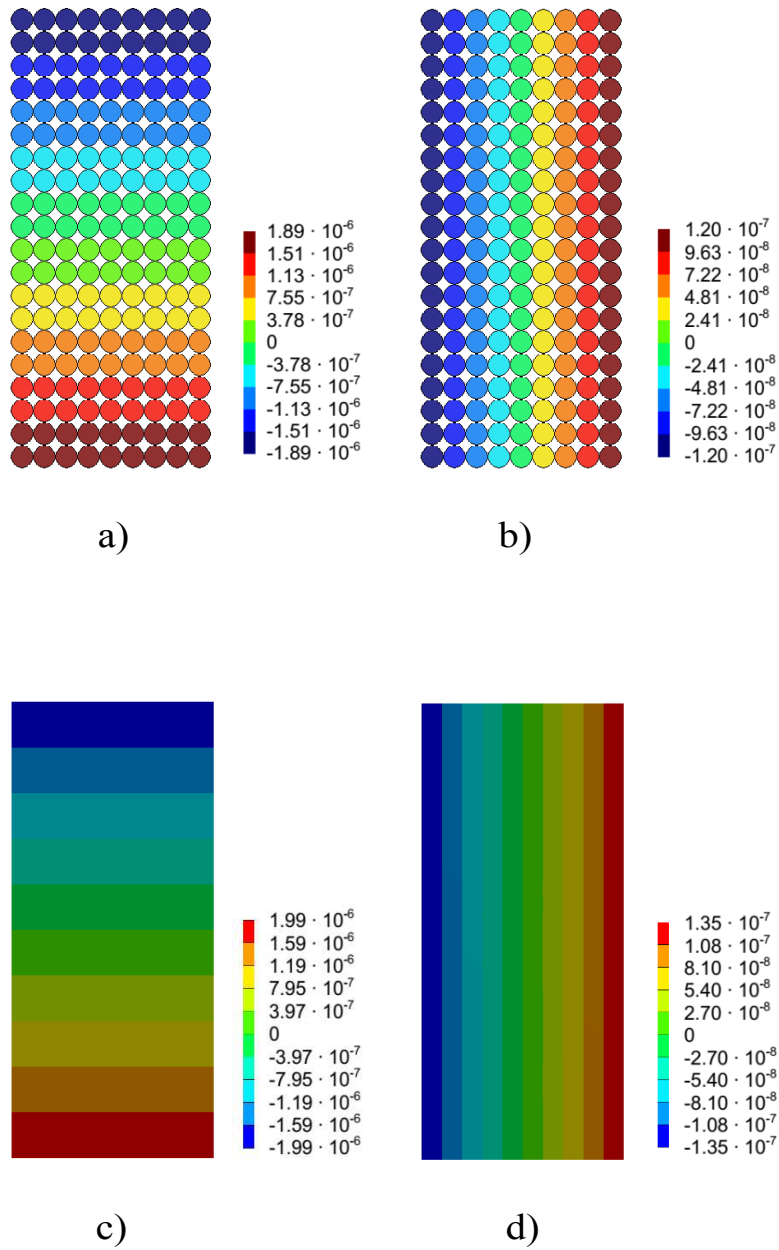


**Figure 4.5.** Displacement contours Simulation results obtained with: new DEM formulation ( $E_p = 2 \cdot 10^{11}$  Pa,  $\nu_p = 0.35$ ,  $k_n = 7 \cdot 10^{10}$  N/m,  $\xi_n = 5$ ) – contours of displacements (in meters) along: a) the  $y$ -axis, b) the  $x$ -axis at  $t = 0.15$  ms; equivalent FEM model ( $E_{FEM} = 50.32GPa$ ,  $\nu_{FEM} = 0.151$ ,  $\beta = 2 \cdot 10^{-6}$  s) at  $t = 0.15$  ms.

The quasistatic response of the DDEM has been investigated and compared with the FEM solution for other particle properties as well. Figure 4.6 compares the response of the specimen for different values of the particle Young's modulus  $E_p = 2 \cdot 10^{11}$  N/m<sup>2</sup>,  $4 \cdot 10^{11}$  N/m<sup>2</sup>,  $8 \cdot 10^{11}$  N/m<sup>2</sup> ( $k_n/E_p = 0.350, 0.175, 0.0875$ ) with a fixed particle Poisson's ratio  $\nu_p = 0.35$ . The response obtained with the standard DEM has also been shown. The axial deformation obtained numerically at the maximum loading again agrees very well with the theoretical predictions.

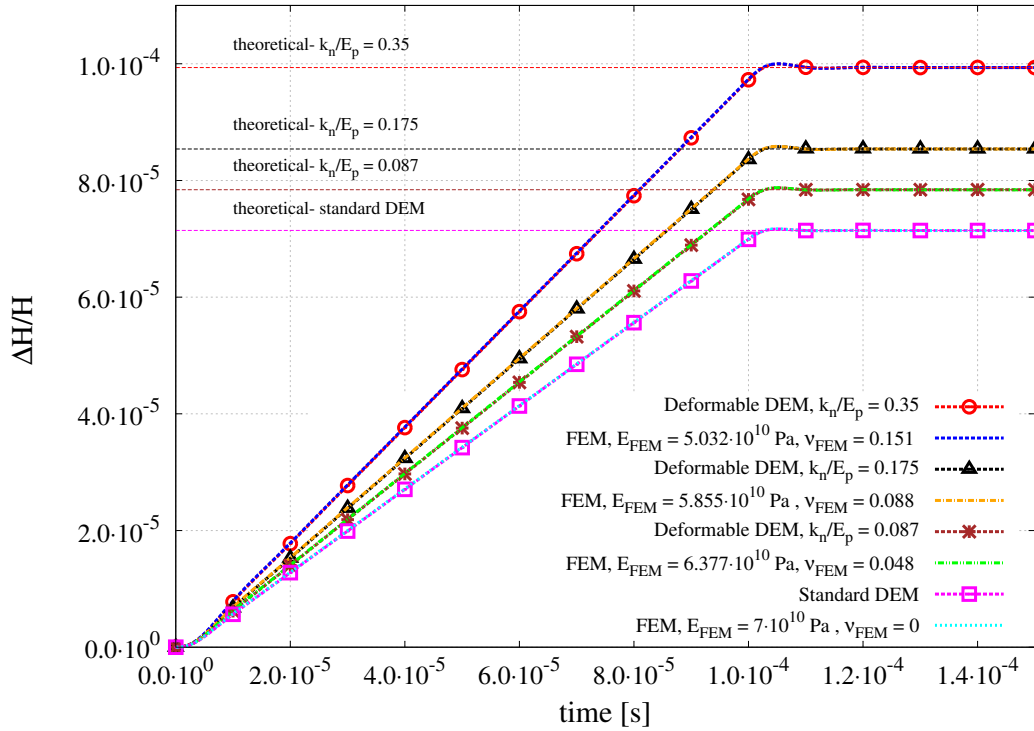


**Figure 4.6.** Axial strain as a function of time for different particle Young's modulus. Comparison between standard DEM solution and FEM solution ( $k_n = 7 \cdot 10^{10}$  N/m,  $\nu_p = 0.35$ , damping ratio  $\xi = 5.0$ ).

**Table 4.1.** Effective elastic properties evaluated from DDEM simulations ( $k_n = 7 \cdot 10^{10}$  N/m,  $\nu_p = 0.35$ , damping ratio  $\xi = 5.0$ ).

$k_n/E_p$	$E_{DDEM}$ (Pa)	$\nu_{DDEM}$
0.087	$6.377 \cdot 10^{10}$	0.048
0.175	$5.855 \cdot 10^{10}$	0.088
0.350	$5.032 \cdot 10^{10}$	0.151

The effective elastic properties evaluated from DDEM simulations, given in Table 4.1, have been used in respective equivalent FEM models. The results of the FEM simulations have been presented by the plots in Fig. 4.6. A very good agreement of the DDEM and equivalent FEM solutions confirms a good and expected performance of the new formulation of the DEM.

Figure 4.6 shows the effect of the particle properties on the effective stiffness. The lower the particle Young's modulus  $E_p$  (or equivalently, the higher the ratio  $k_n/E_p$ ) the lower the global stiffness in the DDEM. The dependence of the effective elastic properties on the microscopic parameters obtained by numerical DDEM simulations for different combinations of the particle properties is shown in Fig. 4.7. Figure 4.7a presents the macroscopic Young's modulus in the DDEM normalized with respect to the macroscopic

Young's modulus in the standard DEM as functions of the ratio  $k_n/E_p$  for different values of the particle Poisson's ratio  $\nu_p$ . A similar dependence for the macroscopic Poisson's ratio in the DDEM is shown in Fig. 4.7b. It can be noticed that the influence of the particle Poisson's ratio  $\nu_p$  on macroscopic Poisson's ratio  $\nu_{DDEM}$  is much greater and much more important than its influence on the global stiffness expressed in terms of the Young's modulus  $E_{DDEM}$ . The numerical relationships plotted in Fig. 4.7 have been compared with the analytical solutions obtained on the basis of the theoretical analysis presented in Sec. 2.8. Global Young's modulus  $E_{DDEM}$  is determined by rewriting Eq. 2.65 as,

$$\frac{f}{2RL} = \frac{k}{L} \frac{h}{2R} \quad (4.23)$$

where  $R$  – the particle radius,  $L$  – the depth of the particle ( $L = 1$  m). Recognising the Hooke's law in Eq. (4.23) with the macroscopic stress and strain given by

$$\sigma_{yy} = \frac{f}{2RL} \quad (4.24)$$

$$\varepsilon_{yy} = \frac{h}{2R} \quad (4.25)$$

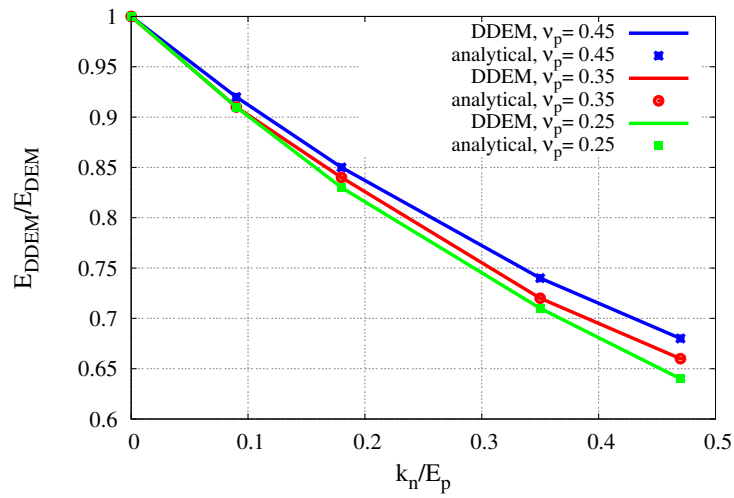
yields,

$$E_{DDEM} = \frac{k}{L} \quad (4.26)$$

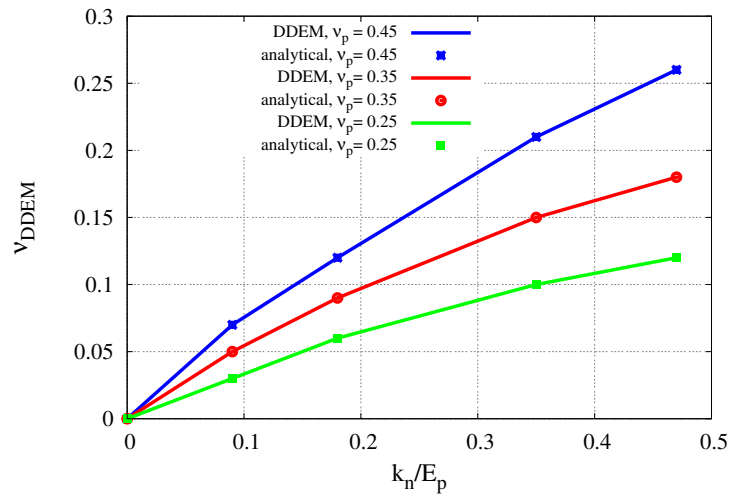
macroscopic Poisson's ratio is given as the negative ratio of the transverse (lateral) and longitudinal (axial) macroscopic strains. Evaluating lateral and axial strains for the given problem corresponding to Eqs. (2.70), (2.74) and using relationships (2.67), (2.69), (2.72), gives following relationship upon algebraic transformation,

$$\nu_{DDEM} = \frac{4\nu_p(1 + \nu_p)k_n}{4(1 - \nu_p^2)k_n + \pi E_p L} \quad (4.27)$$

The analytical and numerical values coincide very well. The analytical results obtained for the particle Poisson's ratio  $\nu_p = 0.35$  and different values of the particle Young's modulus  $E_p$  are also shown in Table 4.2. It can be verified that the analytical values of the effective Young's modulus and the effective Poisson's ration given in Table 4.2 agree very well with numerical estimations of these parameters presented in Table 4.1.



a)



b)

**Figure 4.7.** Macroscopic elastic parameters as a function of the ratio  $k_n/E_p$  for different particle Poisson's ratio – a) ratio of macroscopic Young's moduli in the deformable DEM and standard DEM b) macroscopic Poisson's ratio in deformable DEM.

**Table 4.2.** Analytical evaluation of macroscopic elastic parameters for a fixed particle Poisson's ratio  $\nu_p = 0.35$  and normal contact stiffness,  $k_n = 7.0 \cdot 10^{10}$  N/m.

$k_n/E_p$	$k_p$ (N/m)	$\Delta H^{theo}$ (m)	$\Delta H^{sim}$ (m)	$\nu_{DDEM}$	$E_{DDEM}$ (GPa)	$E_{DDEM}/E_{DEM}$
0.087	$1.432 \cdot 10^{12}$	$2.9796 \cdot 10^{-6}$	$2.9796 \cdot 10^{-6}$	0.048	63.77	0.911
0.175	$7.160 \cdot 10^{11}$	$3.2450 \cdot 10^{-6}$	$3.2450 \cdot 10^{-6}$	0.088	58.55	0.836
0.350	$3.580 \cdot 10^{11}$	$3.7757 \cdot 10^{-6}$	$3.7757 \cdot 10^{-6}$	0.151	50.32	0.719

The quasistatic numerical solutions for the cases presented in Tables 4.1 and 4.2 have been taken for approximate estimation of energy balance discussed in Sec. 2.7. Assuming quasistatic conditions, neglecting the kinetic energy and dissipation, the work done by external force  $W_{ext}$  should be equal to the sum of the elastic energy stored in the contacts  $E_{el,c}$  and strain energy of the deformed particles  $E_{el,p}$ .

$$W_{ext} = E_{el,c} + E_{el,p}. \quad (4.28)$$

Total work due to the external force increasing linearly from 0 to  $F$  and inducing the deformation  $\Delta H$  can be calculated as:

$$W_{ext} = \frac{1}{2} f \Delta H \quad (4.29)$$

The calculations have been performed for the final force value  $f = 90$  kN (10 kN in each column) and the final deformation  $\Delta H$  at  $t = 0.15$  ms. The energy stored in the contacts  $E_{el,c}$  has been calculated according to Eq. (2.59) and the strain energy stored in the particles – according to Eq. (2.61). Particle average strains and stresses have been calculated according to Eqs. (2.73) and (2.69), respectively. The contact forces have been evaluated assuming that the forces transmitted through the particles in series are equal and they are in equilibrium with the total external load.

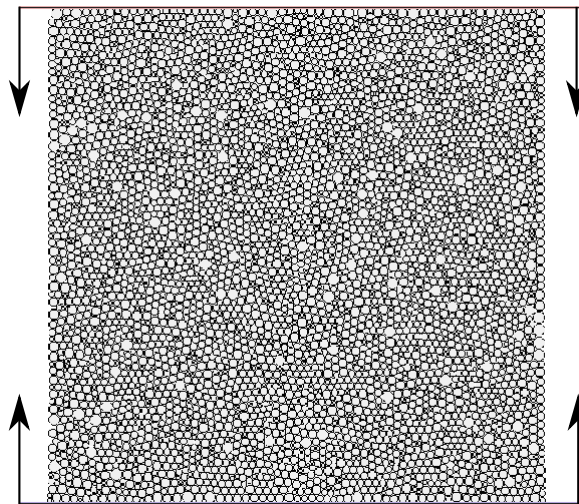
The results of the energy balance estimations have been given in Table 4.3. It can be seen that the condition of energy balance assumed in Eq. (4.28) is quite well satisfied, which is another evidence of the correctness of the DDEM formulation and implemented algorithm. It is worth noticing that the energy stored at the contacts is the same in all the three cases, since the contact forces and contact stiffness are the same. The strain energy due to particle deformation changes – it increases with an increase of the ratio  $k_n/E_p$  (which means an increase of particle compliance). In case of rigid particles ( $k_n/E_p \rightarrow 0$ ) the strain energy in the particles would disappear. The standard DEM (with rigid particles and deformable contact) would be recovered within the DDEM formulation.

**Table 4.3.** Energy balance estimation for fixed particle Poisson's ratio  $\nu_p = 0.35$  and different  $k_n/E_p$  ratios ( $\Delta H$  presented here is taken from the simulations).

$k_n/E_p$	$\Delta H$ (m)	F (kN)	$W_{ext}$ (J)	$E_{el,c}$ (J)	$E_{el,p}$ (J)	$E_{el,c} + E_{el,p}$ (J)
0.087	$2.9796 \cdot 10^{-6}$	90.0	0.1341	0.1221	0.0126	0.1347
0.175	$3.2450 \cdot 10^{-6}$	90.0	0.1460	0.1221	0.0251	0.1472
0.350	$3.7757 \cdot 10^{-6}$	90.0	0.1699	0.1221	0.0503	0.1724

## 4.5 Micro-macro relationships for DDEM model with irregular configuration

A regular configuration of equal particles yields a model with direction dependent properties. The discrete element method when applied to isotropic materials requires irregular configurations of non-uniform size particles. Performance of the deformable discrete element method for such 2D models has been studied here. An unconfined uniaxial compression of a square sample 50 mm by 50 mm shown in Fig. 4.8 has been analysed. The 2D system comprised 4979 disc shaped discrete elements of nonuniform size with an average radius of 0.370 mm, the maximum and minimum radii being 0.652 mm and 0.218 mm, respectively. The particle assembly has been densely packed with the average coordination number 5.8. The loading has been introduced by the flat plates moving with a constant velocity of 5 mm/s and compressing the specimen through the contact with its top and bottom sides.

**Figure 4.8.** 2D model – irregular configuration of nonuniform size particles.

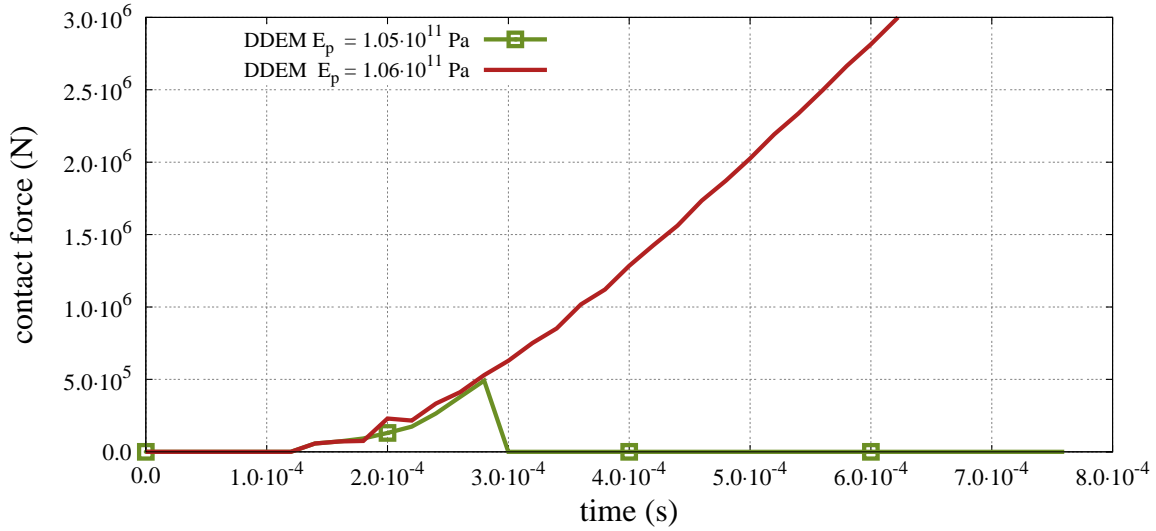


**Figure 4.9.** Contact force vs. time curve for the unconfined uniaxial compression of an irregular specimen using particle Young’s moduli  $E_p = 1.05 \cdot 10^{11}$  Pa ( $k_n/E_p = 0.667$ ) and  $E_p = 1.06 \cdot 10^{11}$  Pa ( $k_n/E_p = 0.660$ ), particle Poisson’s ratio  $\nu_p = 0.45$ .

The microscopic parameters used in these simulations have been the following: particle density  $\rho = 2000$  kg/m<sup>3</sup>, normal contact stiffness  $k_n = 7 \cdot 10^{10}$  N/m. A non-viscous damping defined by Eqs. (2.7) and (2.8) has been used assuming the damping factors  $\alpha^t = \alpha^r = 0.2$ . Firstly, the convergence and stability of the irregular configuration have been examined following the procedure introduced in Ch.3. Subsequently, numerical results are presented with the main objective to determine micro–macro relationships for the model parameters.

Convergence limit and its predictability using analytical relationship given by Eqs. (3.43) and (3.78) has been investigated for irregular configuration cf. Fig.4.8. The effect of the deformability of particles on the time step limit has also been studied similarly as for the regular configurations. In addition to the aforementioned microscopic parameters, the tangential interaction has not been included in the interaction model. Cohesive bonds with very high strength  $\phi_n = 1 \cdot 10^{30}$  N have been imposed on contacting pairs in order to prevent multiple bond breaking during simulation and hence facilitating precise determination of convergence limit.

Stability of the DDEM has been estimated analysing the response of the sample assuming a fixed value of the Poisson’s ratio and changing the Young’s modulus of particles. Comparison of contact force evolution in time has been plotted in Fig. 4.9 for particle Young moduli,  $E_p = 1.05 \cdot 10^{11}$  Pa and  $E_p = 1.06 \cdot 10^{11}$  Pa for a particle Poisson’s ratio  $\nu_p = 0.45$ . It can be deduced from this plot that the particle Young’s modulus  $E_p = 1.06 \cdot 10^{11}$  Pa leads to a stable simulation in contrary to the particle Young’s modulus  $E_p = 1.05 \cdot 10^{11}$  Pa, so  $E_p = 1.06 \cdot 10^{11}$  Pa ( $k_n/E_p = 0.660$ ) can be considered as the stability limit for  $\nu_p = 0.45$ . In the same way, maximum values of the ratio  $k_n/E_p$

ensuring a stable solution have been determined for other values of the particle Poisson's ratio. The results have been presented in Table. 4.4.

**Table 4.4.** Numerical results for the irregular configuration with different particle Poisson's ratio  $\nu_p$  and a constant normal contact stiffness  $k_n = 7 \cdot 10^{10}$  N/m

$\nu_p$	$E_p$ (Pa)	$k_n/E_p$ (numerical)
0.05	$1.32 \cdot 10^{11}$	0.530
0.10	$1.24 \cdot 10^{11}$	0.565
0.15	$1.14 \cdot 10^{11}$	0.614
0.20	$1.05 \cdot 10^{11}$	0.667
0.25	$9.89 \cdot 10^{10}$	0.708
0.30	$9.76 \cdot 10^{10}$	0.717
0.35	$9.92 \cdot 10^{10}$	0.706
0.40	$1.02 \cdot 10^{11}$	0.686
0.45	$1.06 \cdot 10^{11}$	0.660

The numerical stability limit for the irregular configuration has been compared with the convergence limit for the regular HCP configuration given by Eq. (3.78) in Fig. 4.10. It can be observed that the convergence limit of an irregular configuration shows a behaviour similar to that of an HCP configuration. Since the convergence limit for an irregular discrete sample cannot be determined analytically, convergence limit of an HCP sample allows to define an upper bound of the convergence and stability limit for a DDEM model.

The critical time step for irregular configuration has been obtained numerically using the standard DEM (cf. Fig. 4.11) and deformable DEM model (cf. Fig.4.12). The stable evolution of contact force-time curves is obtained for  $\Delta t = 6.0993 \cdot 10^{-8}$  s and  $\Delta t = 6.0141 \cdot 10^{-8}$  s for standard DEM and deformable DEM, respectively, which is a difference of  $\approx 1.42$  %. Therefore, it can be deduced that in this case, the critical time step practically remains the same for both standard DEM and deformable DEM model.

It is convenient to estimate the stable time step in terms of the coefficient  $\alpha$  defined by Eq. (2.19). Taking the critical time step  $\Delta t_{cr} = 6.0993 \cdot 10^{-8}$  s, the minimum mass in the assembly  $m_{min} = 3.0132 \cdot 10^{-4}$  kg for the smallest particle of radius  $r_{min} = 2.1899 \cdot 10^{-4}$  m and the normal contact stiffness  $k_n = 7 \cdot 10^{10}$  N/m,

$$\alpha_{cr} = \Delta t_{cr} / \sqrt{\frac{m_{min}}{k_{max}}} = 6.0993 \cdot 10^{-8} / 6.5609 \cdot 10^{-8} = 0.929 \quad (4.30)$$

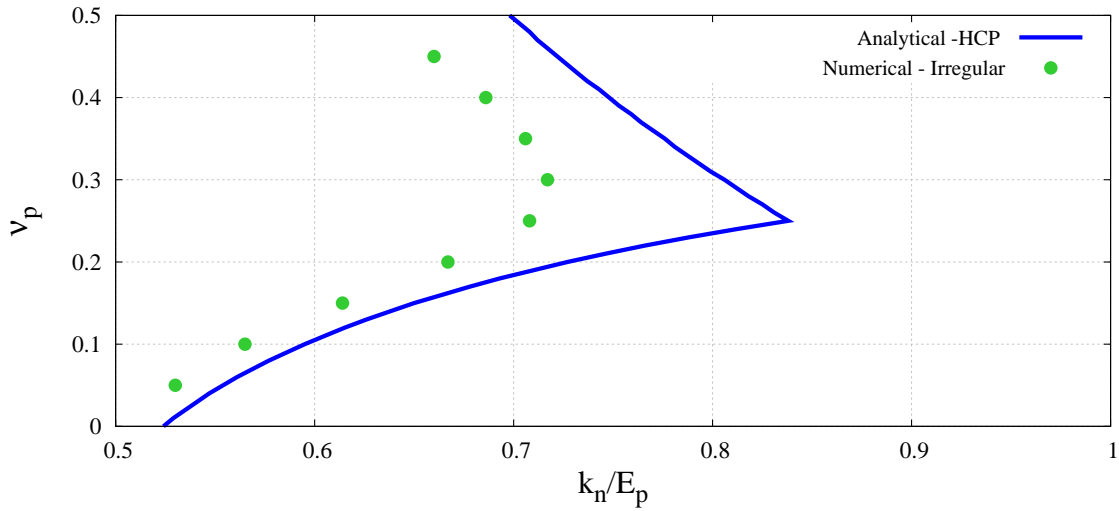


**Figure 4.10.** Comparison of the numerical stability limit for a 2D irregular deformable DEM sample with the analytical convergence limit for HCP configuration ( $k_n = 7 \cdot 10^{10}$  N/m,  $k_t/k_n = 0$ ).

It should be remarked that in practice, the critical time step is estimated with a certain safety factor, therefore a smaller value of the parameter  $\alpha$  should be used in the evaluation of a stable time step.

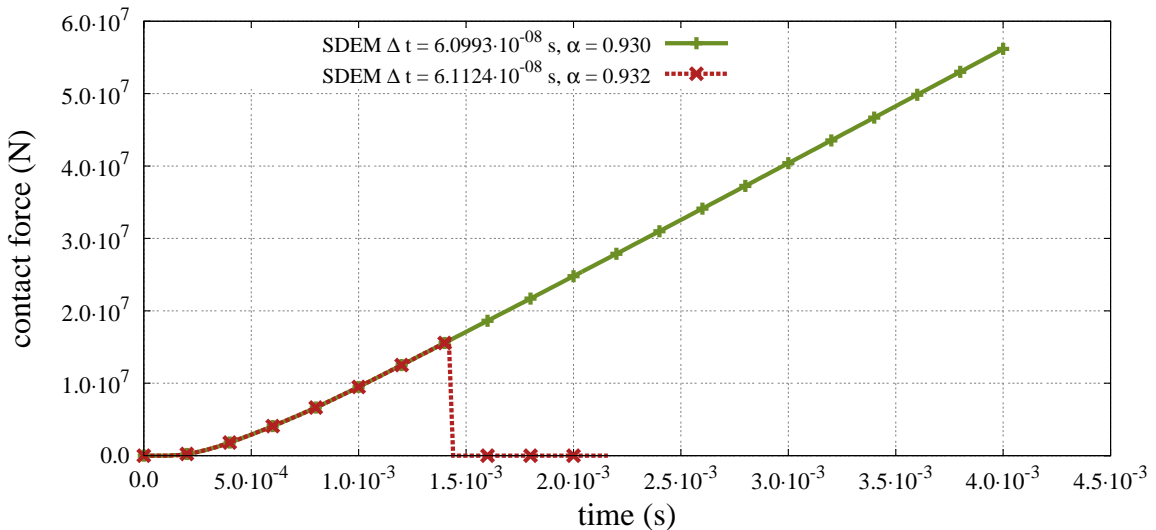


**Figure 4.11.** Contact force vs. time curve for the unconfined uniaxial compression of an irregular sample using time step  $\Delta t = 6.0993 \cdot 10^{-8}$  s and  $6.1124 \cdot 10^{-8}$  s for standard DEM (SDEM) model.

Micro–Macro relationships for irregular configuration has been determined by using the simulation setup described earlier. The microscopic parameters used in these simulations have been the same, except the ratio of tangential to normal contact stiffness,  $k_t/k_n = 0.5$ , interface strength in the normal and tangential direction.  $\phi_n = \phi_t = 2.9 \cdot 10^4$

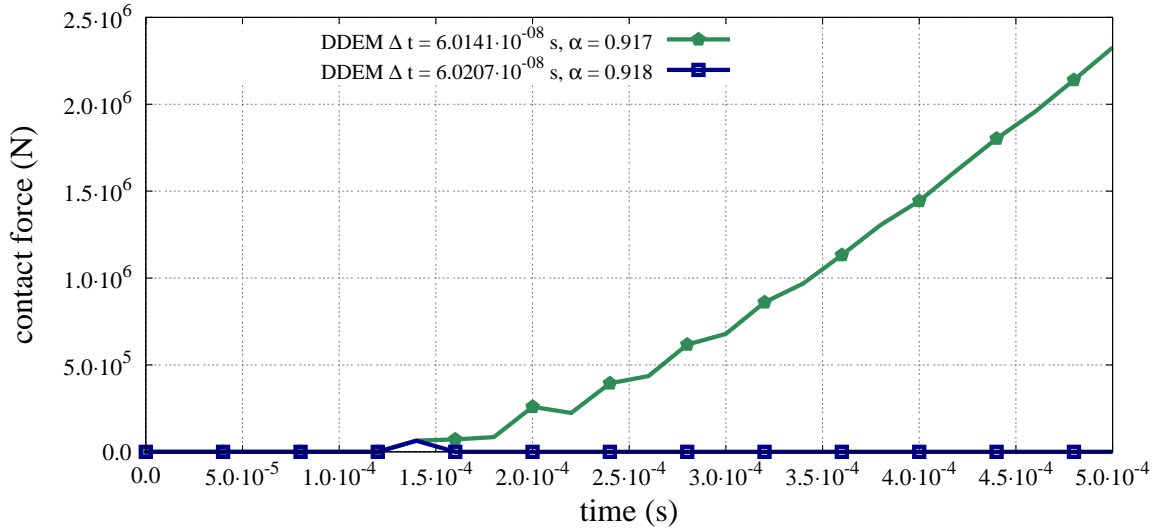


**Figure 4.12.** Contact force-time curve for the unconfined uniaxial compression of an irregular sample using time step  $\Delta t = 6.0141 \cdot 10^{-08}$  s and  $6.0207 \cdot 10^{-08}$  s for deformable DEM (DDEM) model.  $k_n = 7 \cdot 10^{10}$  N/m,  $E_p = 2 \cdot 10^{11}$  Pa and  $k_t/k_n = 0.0$ .

N and Coulomb friction coefficient  $\mu = 0.83$ . Deformable model specific parameters have been: particle Young's modulus  $E_p = 2 \cdot 10^{10}$  Pa, particle Poisson's ratio  $\nu_p = 0.35$ .

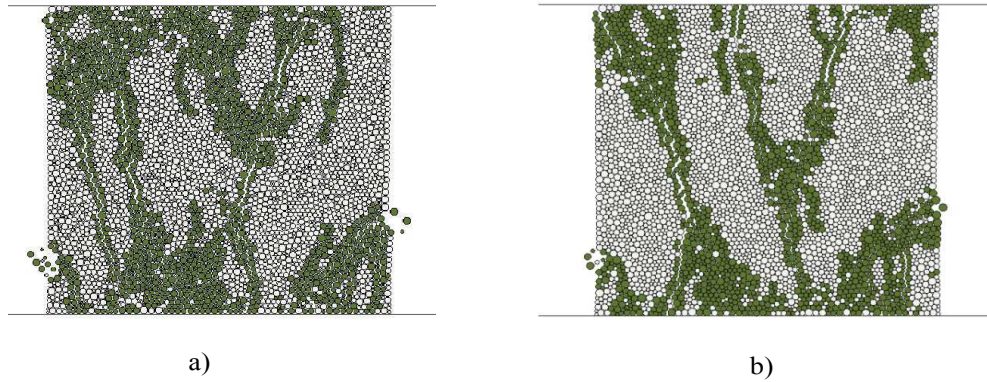


**Figure 4.13.** Failure mode in the simulation of the unconfined uniaxial compression: a) the standard DEM model, b) the deformable DEM model.

Failure modes obtained using the standard and deformable DEM models are shown in Figs. 4.13a) and 4.13b), respectively. The corresponding stress–strain diagrams have been given in Fig. 4.14. The macroscopic stress for this plot has been calculated using Eq. (4.3) and the strain employing the procedure proposed by Bagi [3] and outlined in Sec. 4.1. The mean stresses and strains have been chosen as being suitable to evaluate the elastic moduli. In principle, these measures are not appropriate for the fractured specimens, therefore the stress–strain curves have been constructed in the precritical and small post-critical ranges, and actually, the precritical parts of the curves have been only used in the calculation of the elastic moduli.

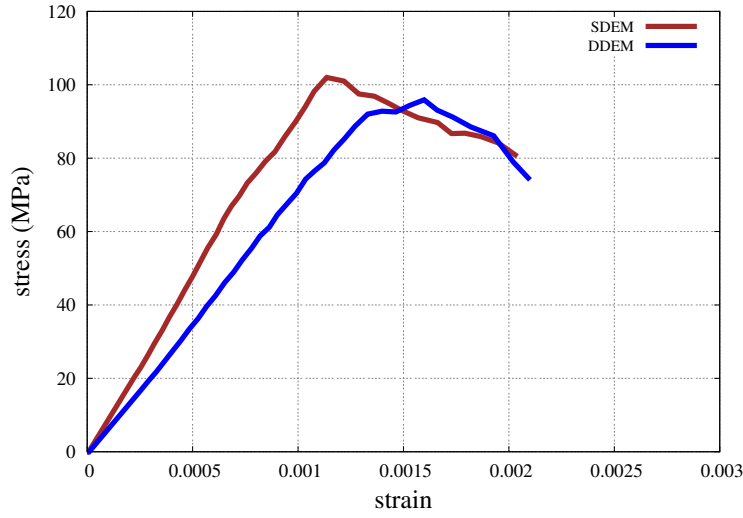


**Figure 4.14.** Comparison of the stress-strain curves for the standard and deformable DEM.

Comparison of the failure modes in Fig. 4.13 and stress–strain diagrams in Fig. 4.14 indicates that the deformable model reproduces a brittle failure, similarly as the standard DEM. The peak value of the stress has changed only slightly. A visible difference between the two curves in Fig. 4.14 is in their slope in the elastic range. This confirms the expected response that the deformability of the particles will allow the modification in the elastic behaviour of the material model. Further on, a detailed investigation of the effect of microscopic model parameters on macroscopic elastic properties will be carried out. Relationships between the macroscopic elastic parameters, Young’s modulus  $E$ , Poisson’s ratio  $\nu$ , and microscopic model parameters will be searched.

The specific form of the relationships (4.9) and (4.10) have been obtained by performing numerical simulations of the unconfined uniaxial compression test defined above for different combinations of the dimensionless parameters:  $k_t/k_n$ ,  $k_n/E_p$ ,  $\nu_p$ . The macroscopic Young’s modulus has been determined from Eq. (4.19) taking the stress range from 0.2 to 0.5 of the maximum stress level in a considered simulation. The macroscopic Poisson’s ratio has been calculated as

$$\nu = -\frac{\Delta\varepsilon_{xx}}{\Delta\varepsilon_{yy}} \quad (4.31)$$

where the increments of the strain components correspond to the range used in the determination of the Young’s modulus. The micro-macro relationships for the deformable DEM have been compared with the relationships (4.7) and (4.8) determined for the standard DEM model.

The simulations have been performed taking the ratio  $k_t/k_n$  in the range from 0 to 1, the particle Poisson’s ratio  $\nu_p$  from 0 to 0.35 and the ratio  $k_n/E_p$  has been assumed in the range from 0 to 0.35. Selected cases have been run additionally for  $\nu_p = 0.45$  and  $k_t/k_n = 1.25$ .

The results of the numerical simulations aiming to determine the micro-macro relationships for the DDEM have been given in Figs. 4.15–4.18. The relationships (4.9) involving the Young’s modulus have been presented in Figs. 4.15 and 4.16. The relationships (4.10) defining the macroscopic Poisson’s ratio have been plotted in Figs. 4.17 and 4.18.

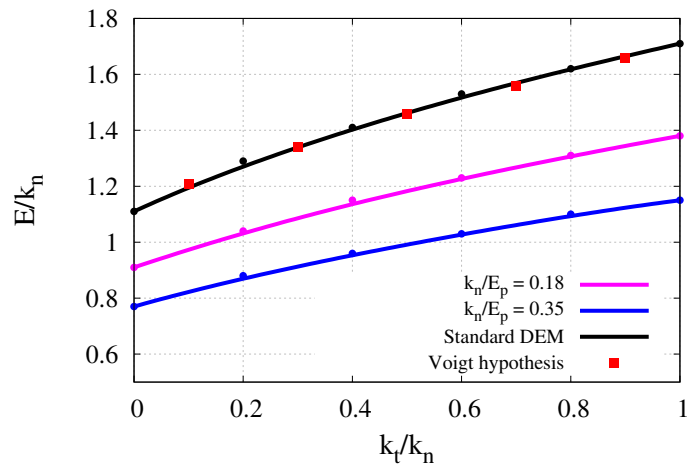
The results of the DDEM have been confronted with the predictions of the standard DEM, and these, in turn, have been compared with the analytical estimations given by Eqs. (4.15) and (4.16) based on the Voigt hypothesis. Evaluation of the Young’s modulus according to Eq. (4.15) using the following parameters characterizing the particle assembly: number of interparticle contacts  $N_c = 14435$ , volume of the sample (RVE)  $V = 0.05 \text{ m} \times 0.05 \text{ m} \times 1 \text{ m}$ , normal contact stiffness  $k_n = 7 \cdot 10^{10} \text{ N/m}$ , average square radius

$$R^2 = \frac{1}{N_p} \sum_{i=1}^{N_p} R_i^2 = 1.49 \cdot 10^{-7} \text{ m}^2 \quad (4.32)$$

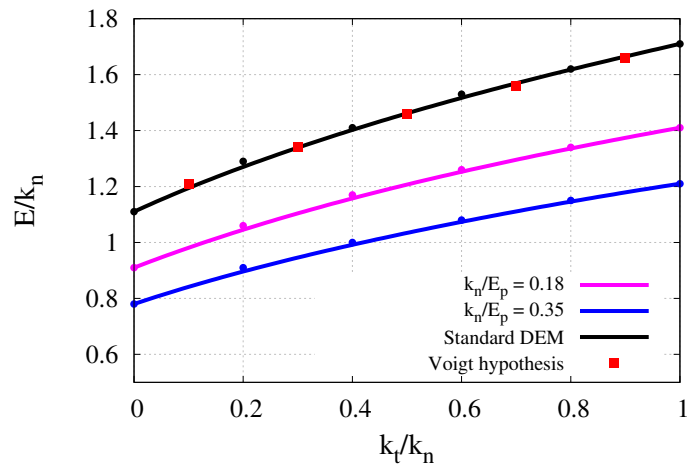
where the number of particles  $N_p = 4979$ . Figures 4.15–4.18 demonstrate a very good agreement of the numerical results obtained with the DEM models and analytical predictions based on the Voigt hypothesis, which confirms a correct performance of the models and DEM implementation.

The macroscopic Young’s modulus  $E$  normalized with respect to the contact stiffness  $k_n$  has been plotted as a function of the stiffness ratio  $k_t/k_n$  for different  $k_n/E_p$  and for fixed values of the particle Poisson’s ratio  $\nu_p$  in Fig. 4.15, and as a function of the stiffness ratio  $k_t/k_n$  and the particle Poisson’s ratio  $\nu_p$  for fixed values of the ratio  $k_n/E_p$  in Fig. 4.16. Figures 4.15 and 4.16 allow to analyse the effect of the microscopic parameters on the macroscopic stiffness. The conclusions which can be drawn are in principle similar to the observations made in the previous section for the regular configuration of discrete elements. The macroscopic stiffness in the DDEM is lower than in the standard DEM. The lower the particle Young’s modulus  $E_p$  (the higher the ratio  $k_n/E_p$ ) is the lower the macroscopic stiffness represented by the dimensionless parameter  $E/k_n$ . The influence of the particle Poisson’s ratio  $\nu_p$  on the macroscopic stiffness is smaller than that of the particle Young’s modulus  $E_p$ . If the ratio  $k_n/E_p$  is close to zero the DDEM solution gets close to the standard DEM solution.

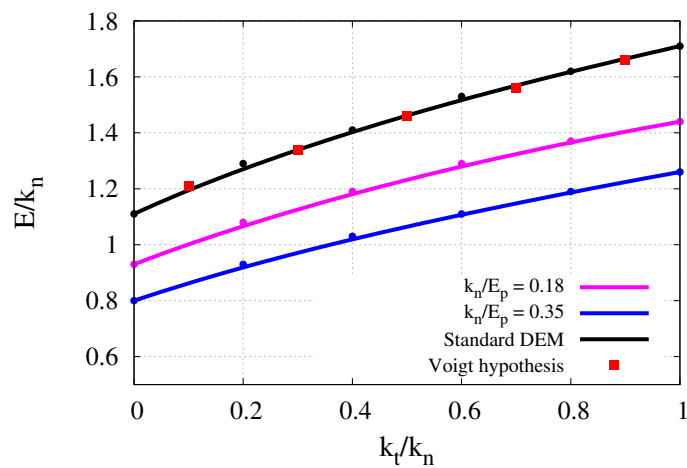
The macroscopic Poisson’s ratio as a function of the stiffness ratios  $k_t/k_n$  for different values of the particle Poisson’s ratio  $\nu_p$  for the fixed ratio  $k_n/E_p = 0.35$  has been plotted in Fig. 4.17. Figure 4.18 gives the macroscopic Poisson’s ratio as a function of the stiffness ratio  $k_t/k_n$  for different ratios  $k_n/E_p$  and fixed values of the particle Poisson’s ratio  $\nu_p$ . For comparison, the numerical results obtained with the standard DEM and analytical predictions based on the Voigt hypothesis according to Eq. (4.16) are given in Figs. 4.17 and 4.18.



a)



b)



c)

**Figure 4.15.** Micro-macro relationships between ratio  $E/k_n$  and stiffness ratio  $k_t/k_n$  for different  $k_n/E_p$  and fixed  $\nu_p$ : a)  $\nu_p = 0.05$ , b)  $\nu_p = 0.25$ , c)  $\nu_p = 0.35$ .

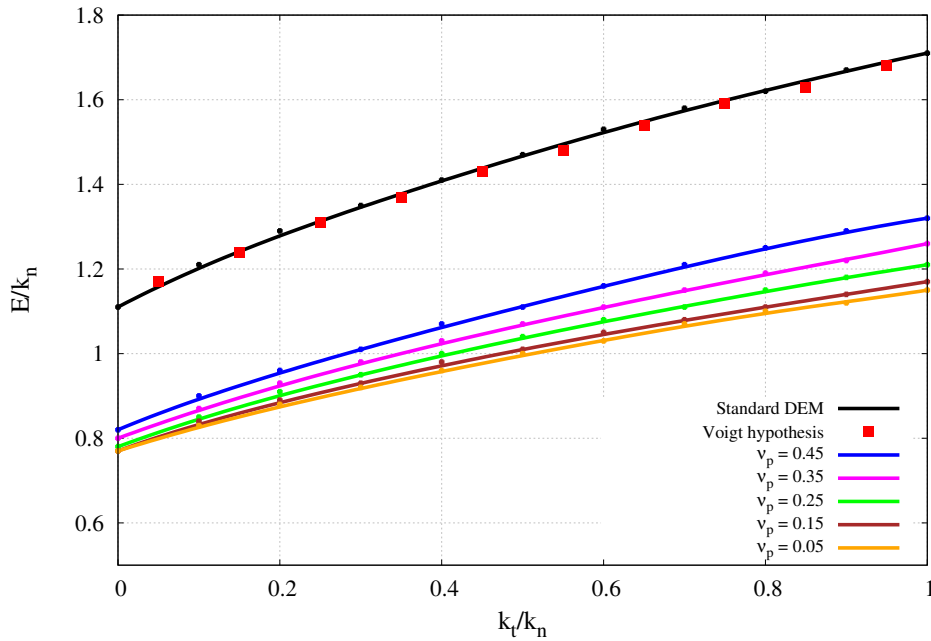


**Figure 4.16.** Micro-macro relationships between the ratio  $E/k_n$  and the stiffness ratio  $k_t/k_n$  for different  $\nu_p$  and the constant ratio  $k_n/E_p = 0.35$ .

When the tangential stiffness is greater than the normal stiffness ( $k_t/k_n > 1$ ) Eq. (4.16) predicts a negative Poisson's ratio [9]. In order to check this effect numerically the range of the ratio  $k_t/k_n$  has been extended to 1.25 for the case shown in Fig. 4.17 ( $k_n/E_p = 0.35$ ). It can be observed in Fig. 4.17 that the Poisson's ratio obtained using the standard DEM model coincides very well with the theoretical prediction including the range  $k_t/k_n > 1$  with the negative value of the Poisson's ratio.

The plots in Figs. 4.17 and 4.18 demonstrate that the DDEM model allows to modify the effective macroscopic Poisson's ratio with respect to the value obtained with the standard DEM. The curves representing the results from the DDEM simulations are off set with respect to the curve obtained with the standard DEM. It can also be noticed that the DDEM can give either a higher or lower value of the Poisson's ratio than that obtained with the standard DEM. The curves corresponding to  $\nu_p > 0.25$  lie above the DEM curve, while those corresponding to  $\nu_p < 0.25$  below. The DDEM model with  $\nu_p = 0.25$  gives the Poisson's ratio practically the same as the standard DEM, cf. Fig. 4.18b. Such variation of the effective macroscopic Poisson's ratio with a change of the particle Poisson's ratio can be explained as follows. The DDEM model introduces two contradictory effects as far as the Poisson's ratio is concerned. On one side, the deformability of the particles with their Poisson's ratio should increase the overall Poisson's ratio. On the other side, the particle deformability decreases the resultant stiffness in the normal direction, cf. Eq. (2.67), thus increasing the ratio of the tangential and normal contact stiffness. With the increase of this ratio the global Poisson's ratio decreases. If the particle Poisson's ratio

is small ( $\nu_p < 0.25$ ), the latter effect dominates, and the macroscopic Poisson's ratio is smaller than that from the standard DEM. With the increase of the particle Poisson's ratio above 0.25 the former effect dominates and it yields an increase of the macroscopic Poisson's ratio.

The level of the macroscopic Poisson's ratio change also depends on the ratio  $k_n/E_p$  which is shown in Fig. 4.18. Given a fixed value of the particle Poisson's ratio  $\nu_p$ , the higher the ratio  $k_n/E_p$ , the larger is the change of the macroscopic Poisson's ratio with respect to that obtained in the standard DEM, cf. Figs. 4.18a and 4.18c.

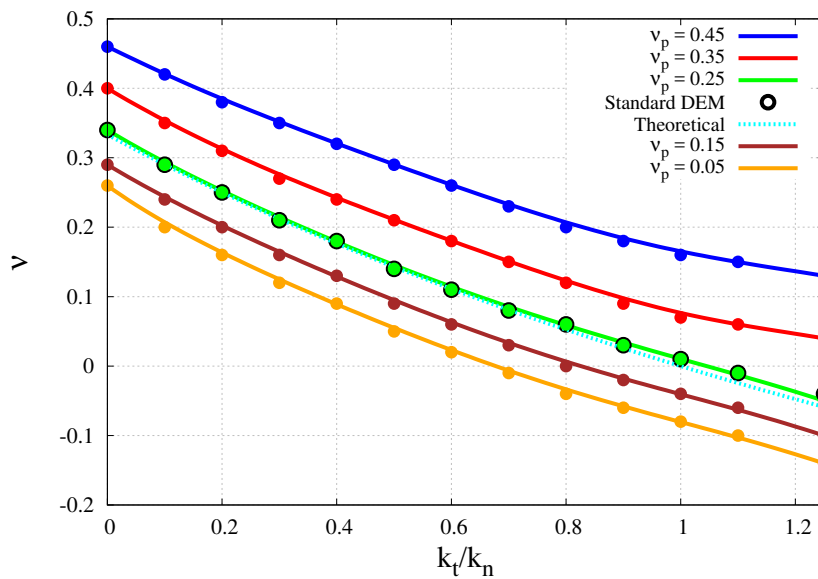
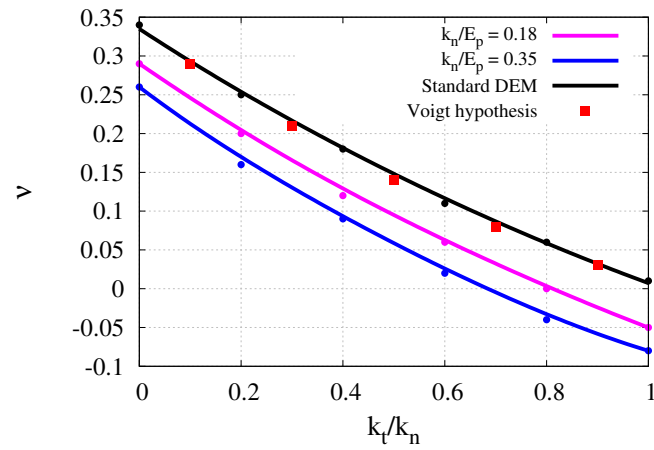


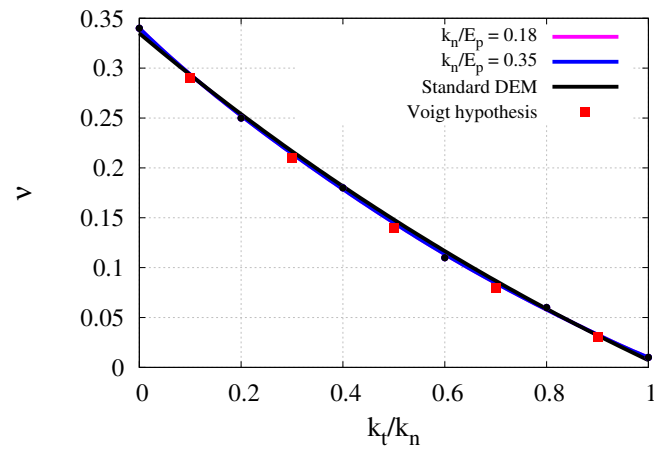
**Figure 4.17.** Micro-macro relationships between the macroscopic Poisson's ratio  $\nu$  and the stiffness ratio  $k_t/k_n$  for different values of the particle Poisson's ratio  $\nu_p$  for the fixed ratio  $k_n/E_p = 0.35$ .

Deformation of the specimen at the uniaxial compression test can be decomposed into two pure deformation modes – an isotropic compression mode and a pure deviatoric (volume conserving) mode. A superposition of the isotropic compression and pure deviatoric deformation modes in granular materials in case of large strains is associated with a development of anisotropy [87]. In this work, a relatively small strain of cohesive granular sample is considered, so an isotropic behaviour is assumed. In order to verify if the pure deformation modes can be extracted properly from the unconfined uniaxial compression additional simulations have been performed.

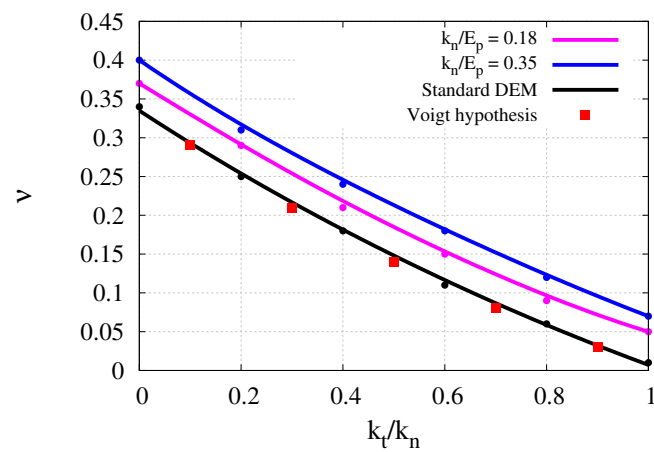
For the specimen with irregular configuration of particles considered above, additional simulations of the isotropic biaxial compression and pure shear tests have been performed in order to determine the bulk modulus  $K$  and shear modulus  $G$ , respectively. Afterwards the obtained values are compared with the respective moduli, determined from the uncon-



a)



b)



c)

**Figure 4.18.** Micro-macro relationships between the macroscopic Poisson's ratio  $\nu$  and the stiffness ratio  $k_t/k_n$  for different ratios  $k_n/E_p$  and fixed  $\nu_p$ : a)  $\nu_p = 0.05$ , b)  $\nu_p = 0.25$ , c)  $\nu_p = 0.35$ .

finned uniaxial compression test. The DEM and DDEM simulations have been performed for different ratios  $k_t/k_n$ . Only one case of the deformable DEM model using particle Young's modulus  $E_p = 2 \cdot 10^{11}$  ( $k_n/E_p = 0.35$ ) and particle Poisson's ratio  $\nu_p = 0.35$  has been investigated.

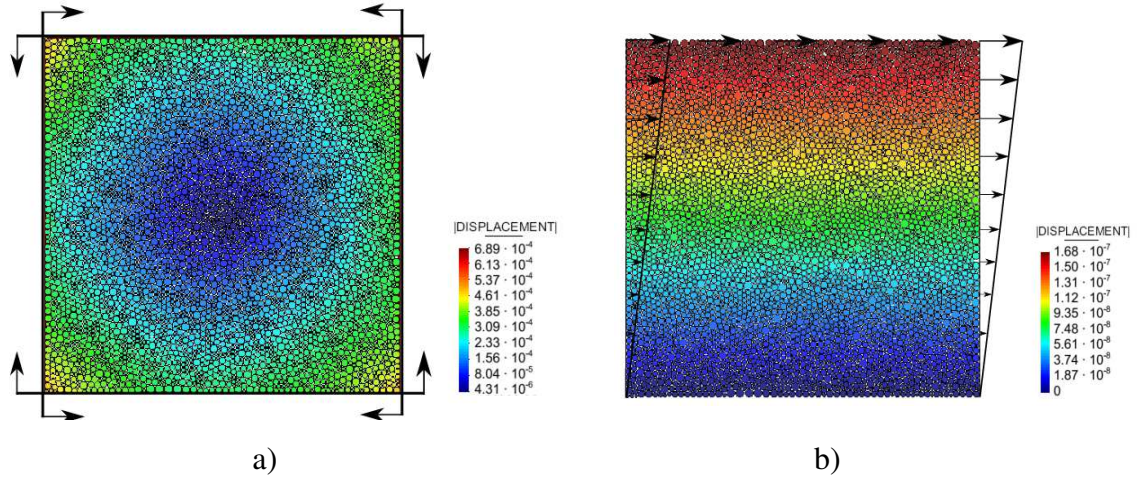


**Figure 4.19.** Displacement contours for irregular configuration: a) under isotropic mode b) under deviatoric mode.

Figure 4.19 shows the displacement contours for the biaxial isotropic compression and pure shear test. The isotropic compression (Figure 4.19a) has been introduced by 4 rigid plates being in contact with the sample and compressing the sample biaxially with prescribed velocity. The pure shear deformation has been obtained by the appropriate kinematic constraints applied to the boundary particles: the particles at the bottom have been fixed, a certain horizontal velocity has been prescribed to the particles at the top side, the particles at the left and right sides have been prescribed the horizontal velocity with the value varying linearly along the sides from zero at the bottom to the value prescribed at the top (as it is presented schematically in Figure 4.19b). The zero vertical velocity for all the boundary nodes has been imposed. The rotations of the boundary particles have not been constrained.

The bulk and shear moduli have been evaluated using the macroscopic stresses calculated according to Eq. (4.3) and the strain evaluated employing the procedure proposed by Bagi presented in Sec. 4.1. The bulk modulus  $K$  has been evaluated from the following relationship:

$$K = \frac{\Delta\sigma_h}{\Delta\varepsilon_{vol}}, \quad (4.33)$$

where  $\sigma_h$  is the hydrostatic stress

$$\sigma_h = \frac{\sigma_{xx} + \sigma_{yy}}{2} \quad (4.34)$$

and  $\varepsilon_{vol}$  is the volumetric strain

$$\varepsilon_{vol} = \varepsilon_{xx} + \varepsilon_{yy}. \quad (4.35)$$

The shear modulus  $G$  has been calculated from the following relationship:

$$G = \frac{\Delta\sigma_{xy}}{2\Delta\varepsilon_{xy}}. \quad (4.36)$$

The results for the bulk and shear moduli,  $K$  and  $G$  have been presented in the form of dimensionless relationships  $K/k_n$  vs.  $k_t/k_n$  and  $G/k_n$  vs.  $k_t/k_n$  in Figures 4.20a) and 4.20b), respectively.

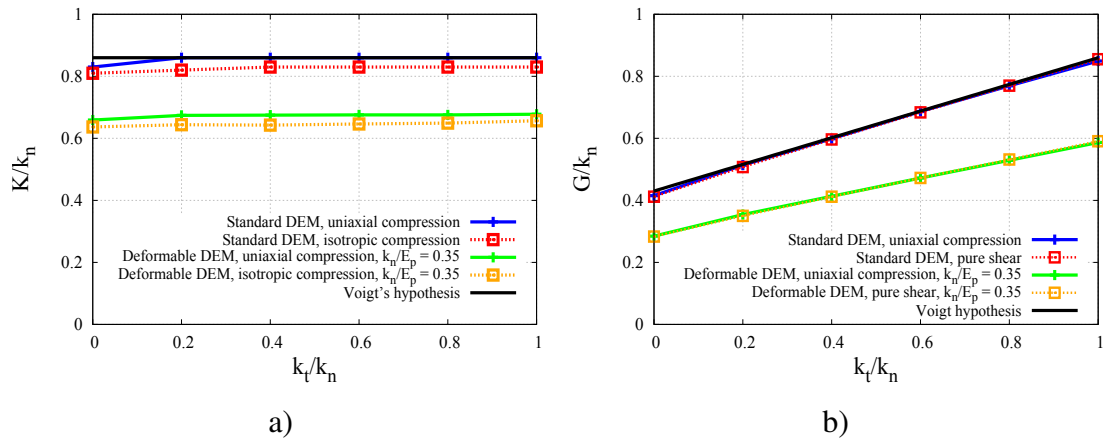


**Figure 4.20.** Normal contact stiffness normalized macroscopic elastic properties as a function of ratio  $k_t/k_n$  : a) bulk modulus b) shear modulus.

The dimensionless relationships from the biaxial isotropic compression and pure shear tests have been compared with the results obtained from the unconfined uniaxial compression tests. The Young's modulus  $E$  and Poisson's ratio  $\nu$  from the unconfined uniaxial compression tests have been used to calculate the bulk and shear moduli by means of Eqs. (4.12) and (4.11). Figures 4.20a) and 4.20b) show that the bulk and shear moduli determined in different ways agree very well. Additionally, for the standard DEM, a comparison with the theoretical predictions according to Eqs. (4.17) and (4.18) based on the Voigt's kinematic hypothesis is provided in both the cases. Again, a very good agreement of the DEM results with Voigt's hypothesis can be observed. Similarly, as for the Young's modulus and Poisson's ratio the volume averaged square radius given by Eq. (4.32) has been used in Eqs. (4.17) and (4.18).

The main result of these comparisons is the demonstration that the isotropic compression and pure shear modes can be extracted from the unconfined uniaxial compression tests. Nevertheless, the fact that the uniaxial compression case actually comprises the other two compression modes viz. isotropic (ISO) and deviatoric (DEV), has been verified for the model by comparing bulk modulus and shear modulus of an unconfined uniaxial case with that of isotropic (ISO) compression and deviatoric (DEV) compression respectively.

## Summary

The theoretical basis for the constitutive relationship between microscopic and macroscopic elastic parameters has been discussed. A dimensionless framework for the constitutive relationships developed here has been used to compare the DDEM model with standard DEM model. It has been confirmed in numerical tests that DDEM algorithm shows a good performance. The finite element simulations employing equivalent FEM models as well as available analytical solutions have been used to verify the algorithm. A quantitative investigation of the relationship between the DDEM model and the FEM solution has shown that the DDEM model with appropriate parameters can produce a response equivalent to that obtained in a detailed FEM analysis of deformable particles.

Enhanced modelling capabilities of the DDEM in comparison to the standard DEM are illustrated through conducted numerical studies. Numerical tests have demonstrated the ability of the DDEM to broaden the range of the macroscopic Poisson's ratio in comparison to the values achievable in the standard DEM. The induced nonlocal contact interactions due to the change of the shape (global deformation) of the discrete particles produce the Poisson's effect even in such configurations when the standard DEM fails to capture the Poisson's effect.

The capability to obtain an appropriate Poisson's ratio is important in different applications, for instance, in problems of wave propagation. The Poisson's ratio influences the ratio of compressional to shear wave speed, which is very important, for instance in geological applications. The DDEM formulation also affects the elastic Young's modulus. The macroscopic elastic stiffness is decreased with respect to the standard DEM. The relationships between the macroscopic effective elastic moduli and microscopic parameters of the new DEM model determined from a series of numerical simulations can be used in the calibration of the DDEM model for given macroscopic properties of a material in real applications of the new model.

The failure and post-failure behaviour has not been analysed here in details, however, stress-strain curves and fractured specimens do show that the new formulation can reproduce a brittle failure. In the present work, attention is limited to the elastic range only in which decohesion does not occur. The 2D formulation of the DDEM, which has investigated in this thesis, can be easily extended to 3D problems.

# Chapter 5

## Simulation of wave propagation using DDEM model

### Introduction

The wave propagation characteristics such as wave velocity, which is particularly important in areas of DEM applications such as geotechnical engineering, are studied in this chapter for the DDEM model. Underlying relationships between wave velocities and the elastic parameters of a solid body are outlined first. Subsequently, the current state of the research on DEM modelling of wave propagation phenomena and its limitation has been presented. A numerical example has been used in order to examine the wave propagation properties of DDEM model w.r.t. standard DEM algorithm. A solid elastic bar shaped sample, discretized with bonded irregular sized disc elements has been used to simulate propagation of longitudinal and shear waves using standard DEM and DDEM models. By using selected combinations of microscopic elastic properties, the ratio of longitudinal to shear velocity, which is the direct measure of macroscopic Poisson's ratio, has been compared for the standard DEM and DDEM models.

### 5.1 Fundamentals of wave propagation modelling

Elastic wave propagation is a fundamental phenomenon experienced commonly in various natural processes such as earthquakes, and engineering problems such as impact loading of civil structures. In a solid body, elastic waves can propagate in two modes, in the longitudinal mode where material points move in the direction of propagation and shear mode where material points move in a plane perpendicular to the direction of propagation. The wave propagation velocities of longitudinal and shear waves in elastic solids,

$c_l$  and  $c_s$ , respectively, depend upon material properties and are given as:

$$c_l = \sqrt{\frac{E}{\rho}} \quad (5.1)$$

$$c_s = \sqrt{\frac{G}{\rho}} \quad (5.2)$$

where  $E$  is Young's modulus,  $G$  is shear modulus and  $\rho$  is bulk density. It must be noted that longitudinal velocity given by Eq. (5.1) is valid for a bar, which is considered in this research. The shear modulus can be defined in terms of Young's modulus  $E$  and Poisson's ratio  $\nu$  using the following relationship:

$$G = \frac{E}{2(1 + \nu)} \quad (5.3)$$

The ratio of longitudinal to shear wave velocity,  $c_l/c_s$  is one of the prime parameters used in characterizing waves, which upon dividing Eq. (5.1) by Eq. (5.2) and using Eq. (5.3) is given as:

$$\frac{c_l}{c_s} = \sqrt{2(1 + \nu)} \quad (5.4)$$

The numerical methods such as the discrete element method (DEM) are commonly used for analysis of different problems of geomechanics or civil engineering involving wave propagation. However, not so many published research focus in detail on the relationship between wave velocities and local contact stiffness between the particles. In [132], Sadd et al. studied the effects of contact laws on wave attenuation and dispersion behaviour of granular material, whereas in [131] Sadd et al. mainly focused on studying the influence of material microstructure on wave propagation behaviour. Mouraille and Luding [98] investigated dispersion and frequency dependence of wave propagation properties of a regular granular media by exploiting "micro-macro" transition [82] between particle level interactions and global behaviour. In [108], O'Donovan and O'Sullivan presented the detailed study of the wave velocities and inter-particle contact stiffness, however, used an ideal and relatively simple hexagonal assembly of uniform sized particles only with a stiffness ratio  $k_t/k_n = 1$ . O'Donovan et al. compared experimental results on a model cubical cell of soil with DEM and continuum analysis in [107] and hence was limited only for the particular material properties. The more realistic and practical application of DEM in wave propagation for the problems of geomechanics and civil engineering would require an investigation of a continuous system discretized with non-uniform discrete elements. Additionally, it would be necessary to determine the relationship between microscopic particle interactions and macroscopic wave propagation

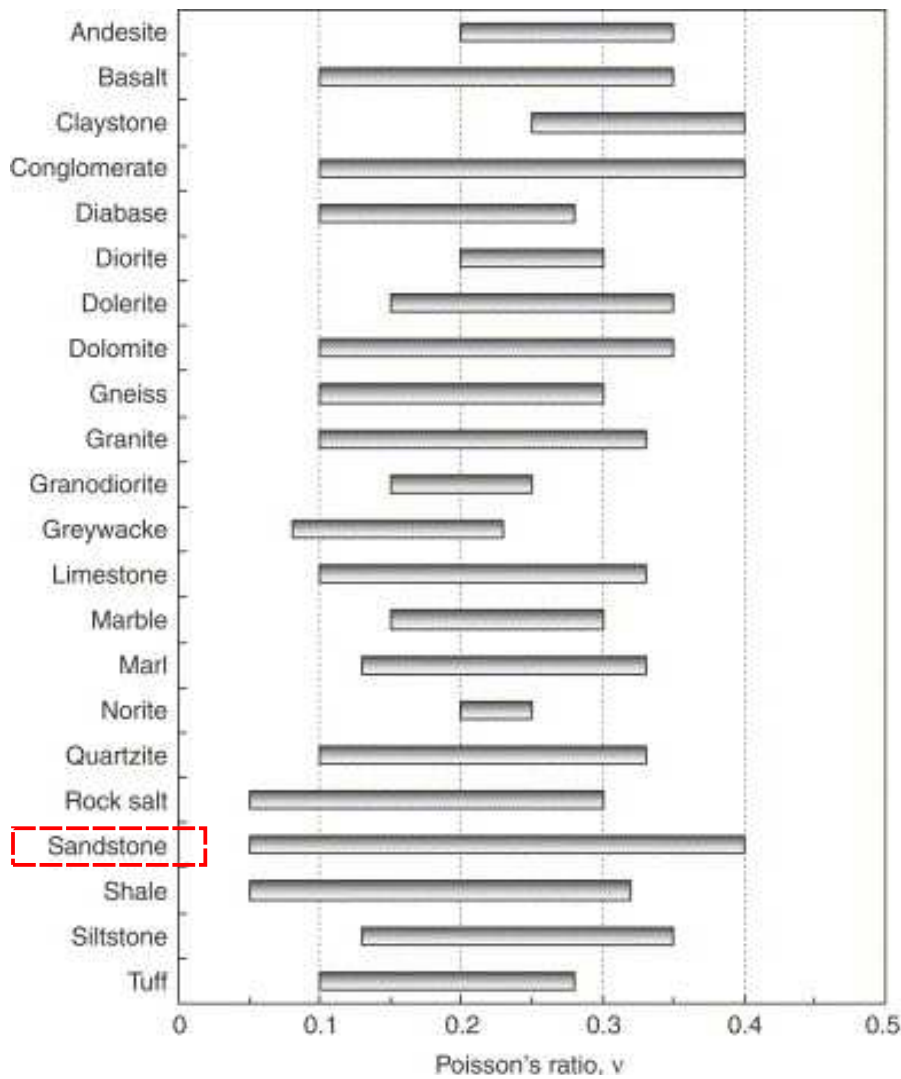


**Figure 5.1.** Typical ranges of values of Poisson's ratio for some rock types [41].

characteristics for the entire range of stiffness ratio  $k_t/k_n$  in order to establish the suitability of DEM for a wider spectrum of problems. However, due to limitations of DEM in its current form as described previously, it can not be used to simulate wave propagation phenomena in materials where maximum Poisson's ratio can reach unto 0.40, e.g. in sandstone (cf. Fig.5.1) and even up to 0.45 in Neagha rock formation.

The present chapter investigates the capability of the DDEM model to properly model the wave propagation phenomenon in solid materials especially in the range of elastic properties beyond the limitations of standard formulation of DEM and for the entire scope of the ratio  $k_t/k_n$  from 0 to 1.0. A numerical example has been presented in order to illustrate the wave propagation phenomenon in an elastic solid discretized with discs (2D discrete elements). The ratio of longitudinal to shear wave velocity,  $c_l/c_s$  which is related to the sample's Poisson ratio through Eq. (5.4) has been evaluated for DDEM model and compared with that for the standard DEM model.

## 5.2 Numerical example

Wave propagation phenomenon has been simulated using a rectangular sample (cf. Fig. 5.2) discretized with 682 bonded disc elements with parameters shown in Table 5.1. Simulations are performed for the ratio  $k_t/k_n$  ranging between 0.0 to 1.0. Waves in DEM sample have been triggered by defining initial displacements of the particles in  $x$  and  $y$  directions to generate longitudinal and shear waves respectively using the following function:

$$u_x^0, u_y^0 = A \cos\left(\frac{2\pi x}{L} + 1\right) \quad (5.5)$$

where position of the particles in  $x$ -direction is bounded within,  $0 \leq x \leq L/2$  in reference to the left edge of the sample. An amplitude  $A = 0.01$  mm and wavelength  $L = 10$  mm is assumed. In case of the longitudinal wave, particles at the top and bottom edge are unconstrained in  $x$  and  $y$  directions which allows to treat particle assembly as a bar. Periodic boundary conditions are applied in case of the shear wave on top and bottom edges. Particles on the right edge are fixed in  $x$  - direction.

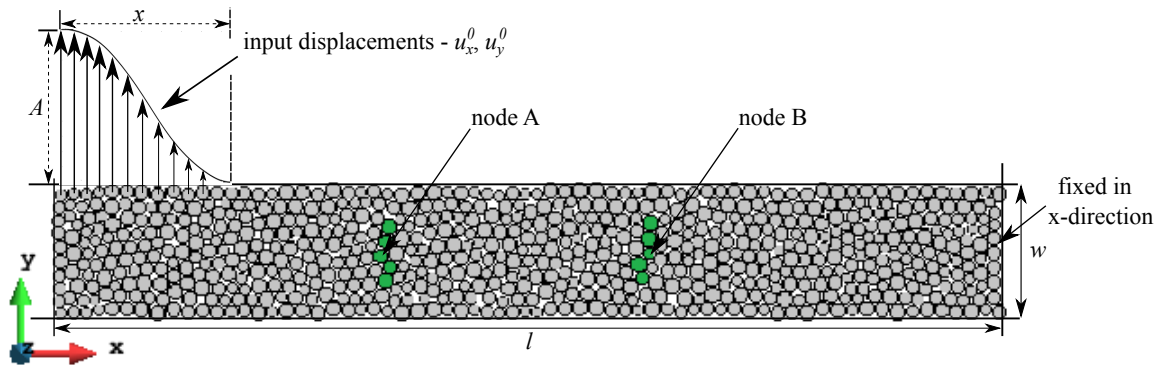


**Figure 5.2.** A 2D elastic solid discretized with disc elements used to simulate wave propagation characteristics of DDEM model.

**Table 5.1.** Parameters of DEM sample used in numerical studies (cf. Fig.5.2).

symbol	parameter	value	units
$N_p$	no. of particles	682	-
$R_{max.}$	max. radius	0.145	mm
$R_{min.}$	min. radius	0.1	mm
$l$	sample length	16.54	mm
$w$	sample width	2.3	mm
$e$	porosity	0.11	-
$\rho_p$	particle density	2000.0	kg/m <sup>3</sup>
$\rho_{avg.}$	sample average density	1784.26	kg/m <sup>3</sup>
$k_n$	normal contact stiffness	$1 \cdot 10^{10}$	N/m

Figure 5.3 illustrates the longitudinal wave propagation through the DEM sample in terms of  $x$  displacement vectors of particles at different time steps. Peak to peak method is used on the displacement-time curve to evaluate velocity of the wave between two nodes with known longitudinal distance between them. For instance, time evolution of  $x$  displacements for two nodes viz. node A and node B (cf. Fig. 5.2) is shown in Fig. 5.4 for standard DEM and DDEM model. Time between peak to peak of displacement time curve for these nodes is evaluated as,  $\Delta t = 2.021 \cdot 10^{-6}$  s and  $\Delta t = 2.283 \cdot 10^{-6}$  s for standard DEM and DDEM respectively.

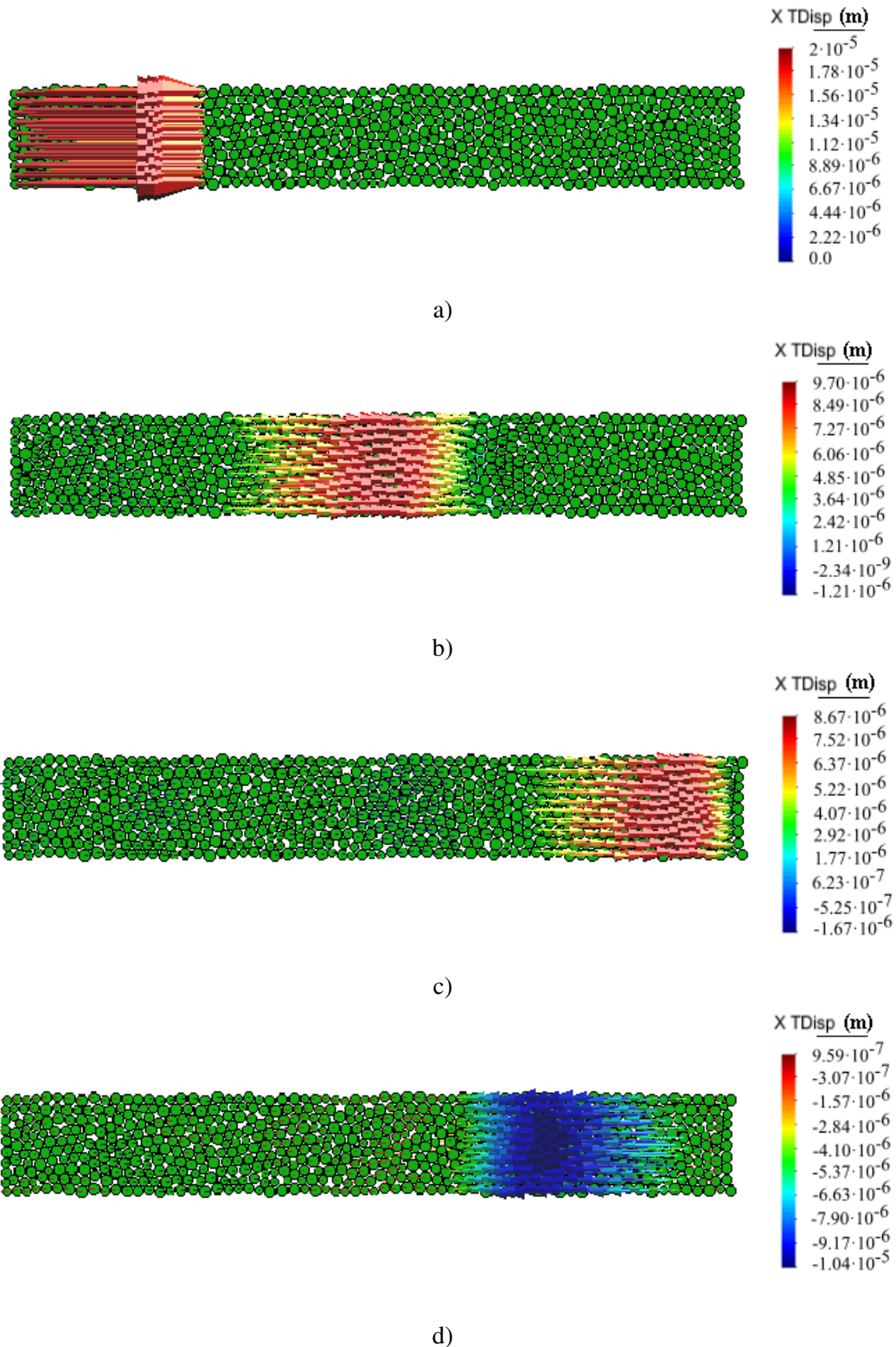


**Figure 5.3.** Longitudinal wave propagation through DEM sample. Snapshots of particle displacement vectors in  $x$ -direction have been captured at time – a)  $t = 0$  s, b)  $t = 3.305 \cdot 10^{-6}$  s, c)  $t = 6.397 \cdot 10^{-6}$  s, d)  $t = 8.822 \cdot 10^{-6}$  s. DDEM parameters –  $k_n/E_p = 0.18$ ,  $\nu_p = 0.45$ .

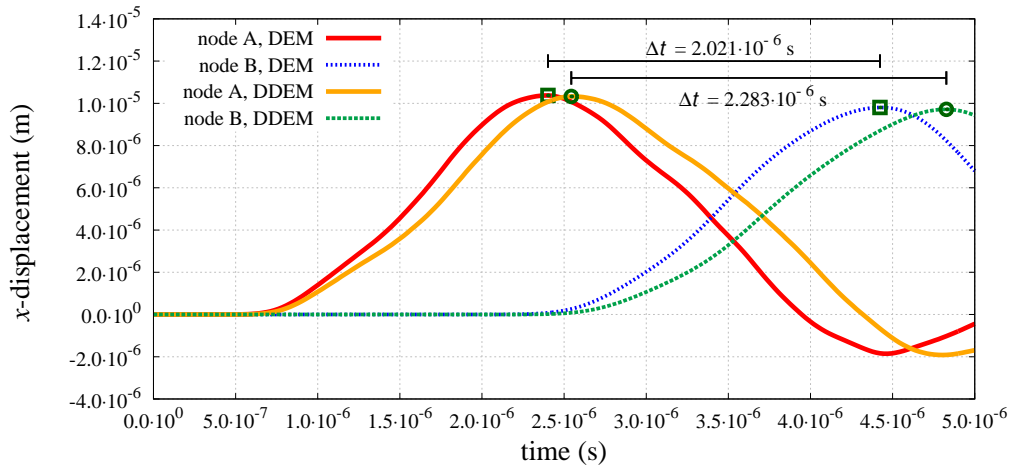


**Figure 5.4.** Time evolution of  $x$ -displacement for node A and node B (cf. Fig. 5.2) with longitudinal wave propagation – the time  $\Delta t$  taken by wave to travel between chosen nodes using standard DEM model and deformable DEM is also shown.

Similarly, the shear wave propagation through DEM bar is shown in Fig. 5.5 and in terms of  $y$  displacement vectors of elements. Time evolution of  $y$  displacements for the nodes A and B is presented in Fig. 5.6 for standard DEM and DDEM model, where a peak to peak time difference,  $\Delta t = 3.543 \cdot 10^{-6}$  s and  $\Delta t = 3.591 \cdot 10^{-6}$  s is obtained respectively. Wave velocity for a given  $k_t/k_n$  ratio is determined as an average of wave velocities obtained through displacement-time curve for 5 pairs of node highlighted (in green colour) in Fig. 5.2.

Likewise, the averaged longitudinal and shear wave velocity is determined numerically for discrete samples with different  $k_t/k_n$  ratio varying between 0 and 1.0 using standard DEM and DDEM models. For DDEM model, selected combinations of microscopic parameters are chosen to examine their influence on the wave velocities and consequently on their ratio,  $c_l/c_s$ . In consistency with the dimensionless framework for elastic parameters described in Sec. 4.2, two values of ratio  $k_n/E_p = 0.18, 0.35$  for a constant value of particle Poisson's ratio,  $\nu_p = 0.45$ , are combined, resulting in two cases which have been investigated, compared and shown in Figs. 5.7 and 5.8. The analytical relationship between the ratios  $c_l/c_s$  and  $k_t/k_n$  for standard DEM is obtained by substituting Eq. (4.16) in Eq. (5.4).

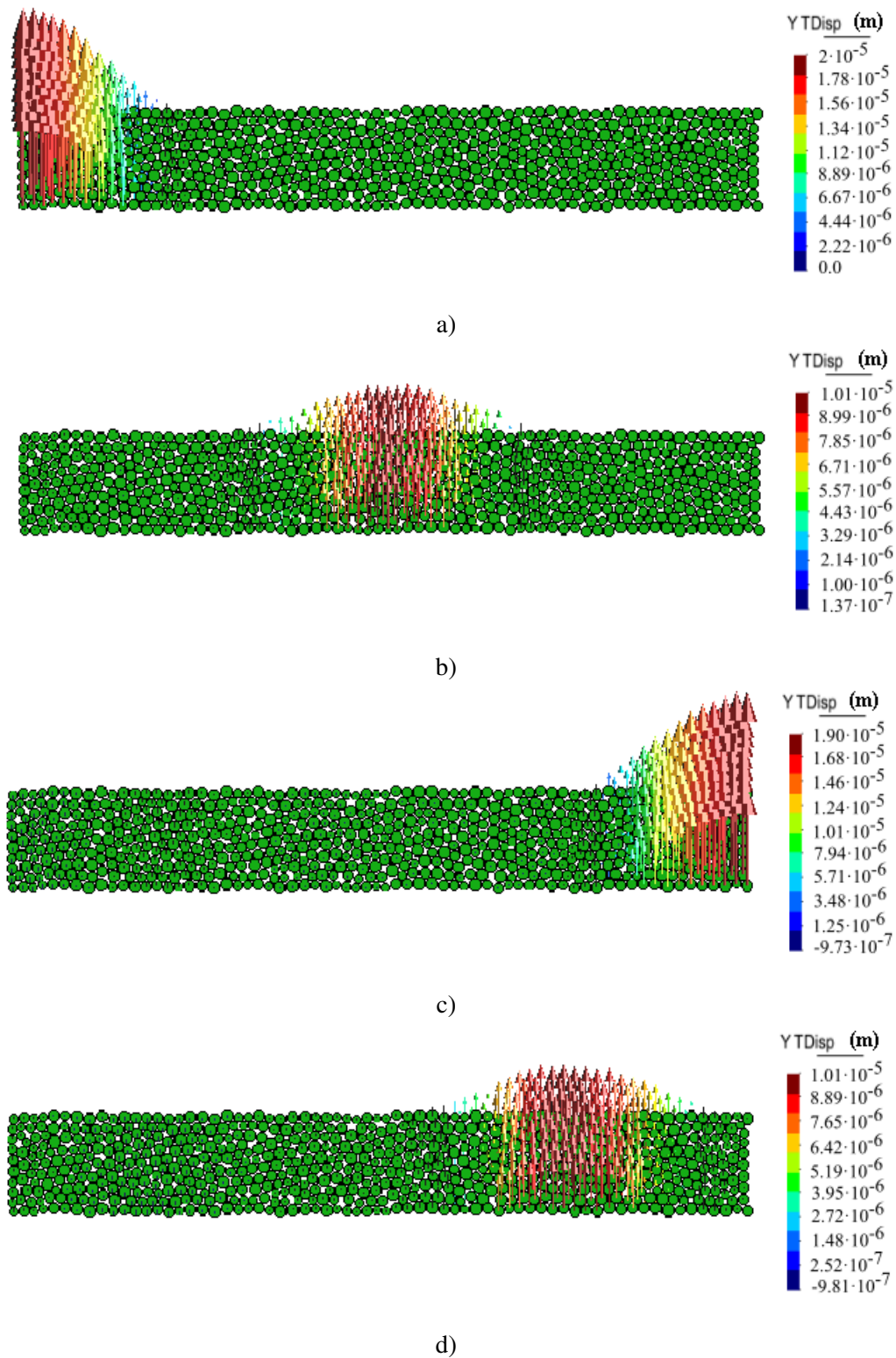


**Figure 5.5.** Shear wave propagation through DEM sample. Snapshots of particle displacement vectors in  $y$ -direction have been captured at time – a)  $t = 0$  s, b)  $t = 6.635 \cdot 10^{-6}$  s, c)  $t = 1.329 \cdot 10^{-5}$  s, d)  $t = 1.615 \cdot 10^{-5}$  s. DDEM parameters –  $k_n/E_p = 0.18$ ,  $\nu_p = 0.45$ .

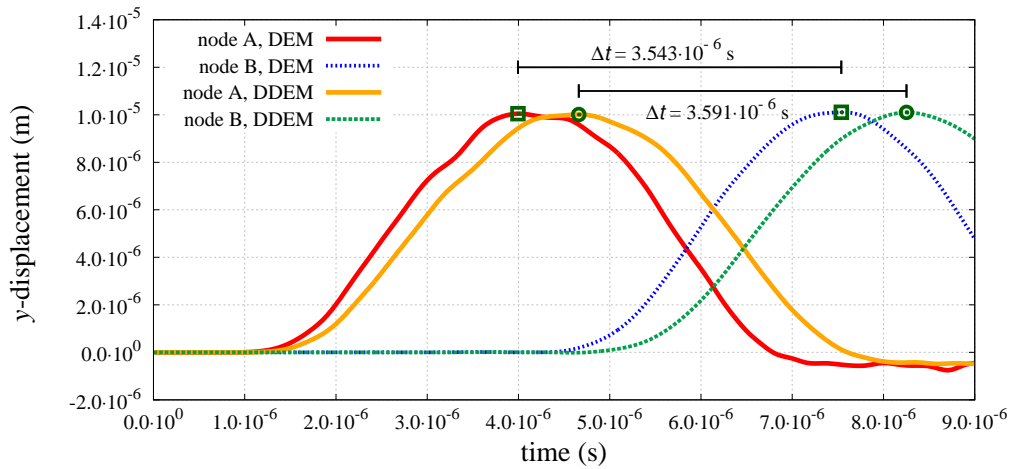
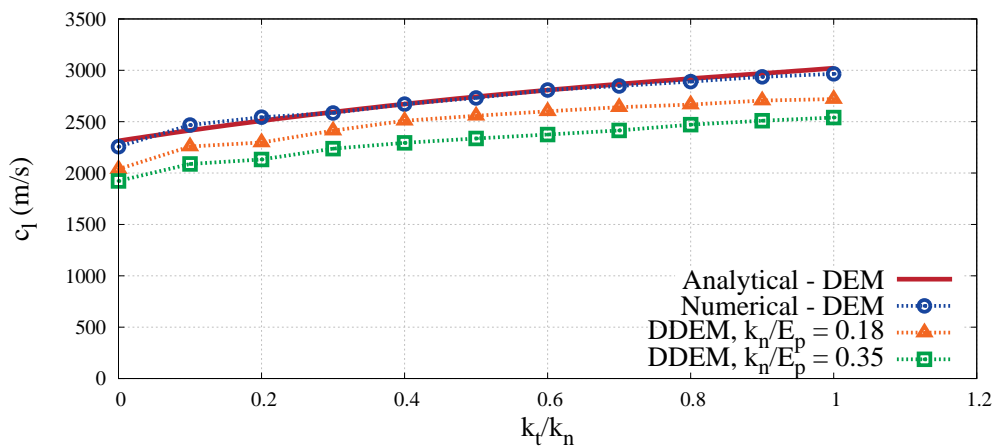
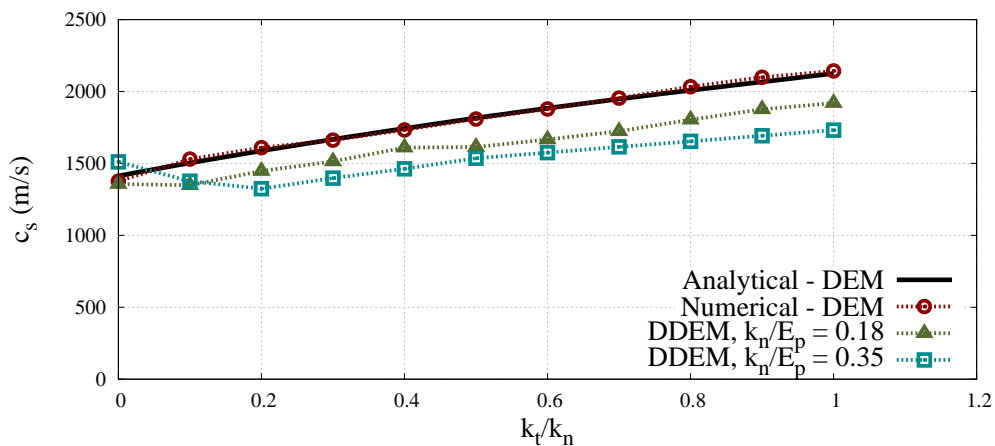


**Figure 5.6.** Time evolution of  $y$ -displacement for node A and node B (cf. Fig.5.2) with shear wave propagation – the time  $\Delta t$  taken by wave to travel between chosen nodes using standard DEM model and deformable DEM is shown.

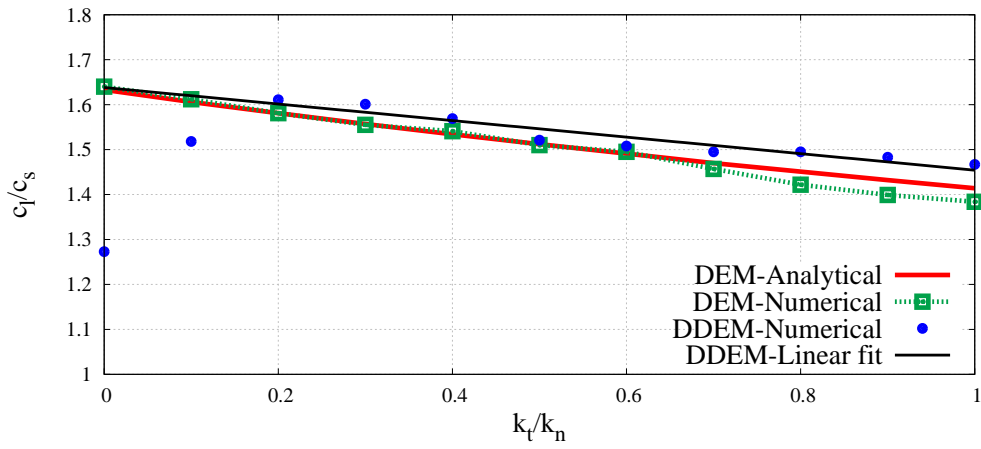


a)

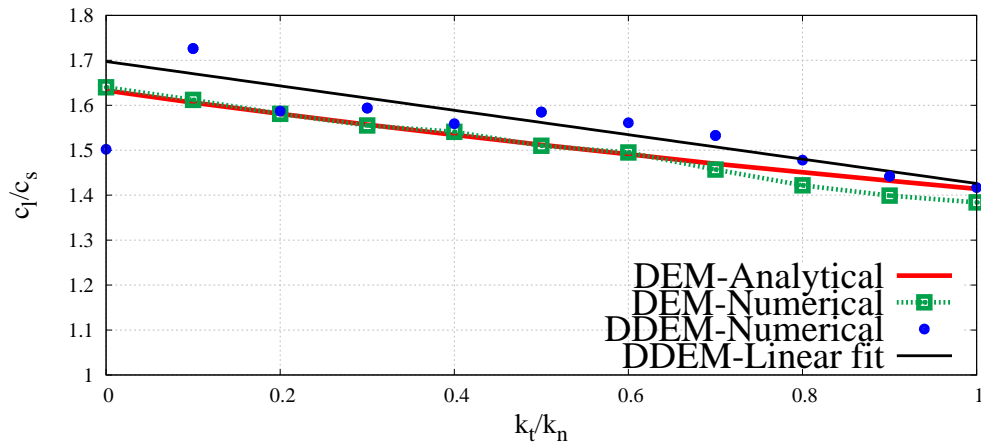


b)

**Figure 5.7.** Shear wave velocity as a function of ratio  $k_t/k_n$  – comparison between standard DEM and DDEM models. Poisson's ratio of particles in DDEM model,  $\nu_p = 0.45$ .



a)



b)

**Figure 5.8.** Comparison of longitudinal to shear wave velocity ratio,  $c_l/c_s$  for standard DEM and DDEM model as a function of ratio  $k_t/k_n$ . Different combinations of microscopic parameters are used for DDEM model: a)  $2.857 \cdot 10^{10}$  Pa ( $k_n/E_p = 0.35$ ), b)  $5.556 \cdot 10^{10}$  Pa ( $k_n/E_p = 0.18$ ). Poisson's ratio of particle,  $\nu_p = 0.45$  is used.

It can be deduced clearly from the results that the wave propagation behaviour of the DDEM model can greatly depend upon the chosen microscopic parameters. It introduces a flexibility in tuning the wave propagation behaviour of the discrete assembly by choosing appropriate microscopic parameters. Consequently, DDEM formulation invokes a capability to address a wider range of practical problems involving wave propagation using the discrete element framework.

However, the unexpected values of  $c_l/c_s$  in each of the two combinations studied here, especially for the initial values of  $k_t/k_n = 0.0, 0.1$  are mainly introduced by the anomalies in shear wave velocities for these two values of  $k_t/k_n$ , cf. Fig. 5.7b and may be attributed to the relatively smaller length of the discrete sample used in this study. Additionally, it must be mentioned that wave propagation in discrete media is also dependent on other characteristics of discrete assembly such as microstructure or fabric and wavelength of the input signal. Evidently, a detailed research is required to address these aspects and may be taken as future work on DDEM. The linear fit indicated on the plots is used to facilitate the comparison between all the cases and is derived on the basis of data points except  $k_t/k_n = 0.0, 0.1$  for each case.

## Summary

The wave propagation characteristics of the DDEM model has been illustrated, which extends its modelling capabilities to the problems related to dynamic processes such as earthquake or impact loading of civil structures. The non-locality of the contact model in DDEM formulation manifests its influence in the dynamic problems as well and provides enhanced flexibility in tuning the DEM model beyond its current limitations. Peak to peak method on displacement time curves seems to present an appropriate method to determine wave velocities numerically. An in-depth study can be foreseen to investigate the shear wave propagation phenomena in the lower values of  $k_t/k_n$  ratio.

# Chapter 6

## Concluding remarks

### 6.1 Summary

Proposed thesis has presented a numerical and analytical investigation on the possibility to alleviate the limitations of standard DEM formulation by appropriately including the deformability of discrete elements in such a manner that its efficiency remains preserved. A summary of the main results and achievements of this thesis is presented as follows:

- A new original formulation of the discrete element method with deformable cylindrical particles, called DDEM (deformable discrete element method) has been studied in this work. Basic idea of DDEM and an outline of its formulation has been presented. In DDEM, the deformability of the particles has been considered in a simple way by introducing the concept of the so-called global deformation mode of the particle. Uniform strains are obtained using the inverse constitutive relationship from the volume averaged stress expressed in terms of the contact forces acting on the particle assuming that the deformation of the particles is induced by a uniform stress field. The contact forces are evaluated as functions of the particle overlap representing the local deformation mode. The global deformation mode is taken into account in determination of the particle overlap, and consequently, in evaluation of contact forces. In this way, due to deformation of the particles the contact in one point influences the contact interaction at other points, which is a feature of a nonlocal contact model. This marks the difference with respect to the standard DEM in which the contacts are independent and do not influence one another.
- An accurate computation of the contact forces in the DDEM formulation requires an iterative solution of the implicit relationship between the contact forces and particle displacements. For preserving the efficiency of discrete element methodology,

the new formulation has been adapted to the explicit time integration since employing iterative solution of an implicit relationship within explicit DEM scheme would spoil its major advantage of efficient solution at a single time step. A rigorous analysis of the convergence and stability of the DDEM formulation has been conducted. A numerical framework for proper selection of microscopic elastic parameters leading to stable solution for a DDEM model has been established. It has been shown that in fact DDEM is robust and stable given that obtained limits are respected.

- A good performance of the new algorithm has been confirmed in numerical tests. The algorithm has been verified by comparison with the finite element simulations employing equivalent FEM models as well as available analytical solutions. A quantitative investigation of the relationship between the DDEM model and the FEM solution has shown that the DDEM model with appropriate parameters can produce a response equivalent to that obtained in a detailed FEM analysis of deformable particles.
- Conducted numerical studies have shown enhanced modelling capabilities of the DDEM in comparison to the standard DEM. Numerical tests have demonstrated the ability of the DDEM to broaden the range of the macroscopic Poisson's ratio in comparison to the values achievable in the standard DEM. The induced nonlocal contact interactions due to the change of the shape (global deformation) of the discrete particles produce the Poisson's effect even in such configurations when the standard DEM fails to capture the Poisson's effect.
- The DDEM formulation also affects the elastic Young's modulus. The macroscopic elastic stiffness is decreased with respect to the standard DEM. The relationships between the macroscopic effective elastic moduli and microscopic parameters of the DDEM model determined from a series of numerical simulations can be used in its calibration of for given macroscopic properties of a material in real applications.
- In discrete element framework, the capability to obtain a complete representation of Poisson's ratio is important in different applications, for instance, in problems of wave propagation. The Poisson's ratio influences the ratio of longitudinal to shear wave speed, which is very important, for instance in geotechnical and civil engineering. Wave propagation phenomena has been simulated and it has been shown that the DDEM model expands the range of cases for a given practical problem that can be simulated using DEM.

## 6.2 Original contributions of the thesis

The original contributions of the presented study on the background of the current state of the art presented in Ch.1, are as follows:

- Micro-macro constitutive relationships for discrete element framework with deformable particles. Contrary to the other discrete element methods with deformable elements, in presented thesis a dimensionless scheme has been used to investigate the significance of particle deformability on macroscopic response of the discrete system. The dimensionless framework used in this work provides a flexibility and ease in calibrating the numerical model with experimental results whereas some experimental data is a pre-requisite in other methods in order to obtain the numerical results.
- Extent of the validity of DEM model with deformable elements. Unlike other discrete element models, presented work addresses the model validity for a much wider range of material parameters rather than experiment specific parameters. In addition to simple configurations with uniform particle size distribution, the model in this work has also been verified for a close to realistic discrete sample with non-uniform particle size distribution. Thus, the validity of the model is examined in a more general sense in this work as compared to others.
- Convergence and stability analysis of the investigated discrete model. In contrast to the models found in literature, a rigorous analysis on convergence and stability of the studied model has been presented in this thesis. A very good estimation on convergence and stability of the model can be drawn using this analysis, even prior to simulating a problem using DDEM model. Whereas other models such as presented in [48], would require considerable simulation experience in order to evaluate the appropriate parameters leading to converged solution, specially for a broader particle size distribution.
- Wave propagation characteristics for a discrete particle assembly with non-uniform sized deformable elements. In presented work the wave propagation phenomenon is examined for the entire spectrum of normal to tangential contact stiffness ratio. Both the modes of wave propagation i.e. longitudinal and shear mode have been studied. Simulation results are obtained in the form of the wave velocity ratio  $c_l/c_s$ , which is the parameter primarily used in the experimental studies for the problems of geomechanics. Whereas, in [64] wave propagation has been studied only in the longitudinal mode using a regular configuration with same sized elements of a particular material.

## 6.3 Suggested future work

Based on the results obtained in the presented thesis, the suggested future research may include:

- Extension of the DDEM algorithm in 3D domain with elastic spheres. Extension of the DDEM formulation to the spherical elements would present a natural next step after having obtained a profound confidence in capabilities of DDEM formulation using disc elements. For validating the DDEM model using experimental results, the verification and theoretical validation of 3D DDEM would be pre-requisite. Benchmark uniaxial compression tests can be used for this purpose in a manner similar to the 2D case. Micro-macro constitutive relationships for the DDEM model in the elastic range must be determined. Additionally, the convergence and stability analysis would also be needed.
- Experimental validation of the DDEM. Validation of the DDEM model could be possibly performed by checking its performance in the problem of powder compaction and elastic wave propagation for instance in the sintered porous material. The experimental data obtained can then be used to validate performance of the DDEM model. A series of simulations would be required to compare the numerical results with experimental ones.
- Adaptation of DDEM formulation for the use of plastic discrete elements. Further adaptation of DDEM to model discrete assembly of plastic particles can be used to address problems in the area of powder metallurgy. Suggested path to follow would be on similar lines as taken in this thesis and previous two points. First, addressing formulation, implementation and verification using 2D elements and subsequently using 3D elements and validating the model using laboratory tests.

# Bibliography

- [1] K.E. Atkinson. *An Introduction to Numerical Analysis*. 2nd edn John Wiley & Sons, 1989.
- [2] K. Bagi. An algorithm to generate random dense arrangements for discrete element simulations of granular assemblies. *Granular Matter*, 7(1):31–43, 2005.
- [3] K. Bagi. Analysis of microstructural strain tensors for granular assemblies. *Int. J. Solids and Structures*, 43:3166–3184, 2006.
- [4] R. Balevičius, I. Sielamowicz, Z. Mróz, and R. Kačianauskas. Effect of rolling friction on wall pressure, discharge velocity and outflow of granular material from a flat-bottomed bin. *Particuology*, 10:672–682, 2012.
- [5] J.P. Bardet and J. Proubet. A numerical investigation of the structure of persistent shear bands in granular media. *Geotechnique*, 41:599–613, 1991.
- [6] R. J. Bathurst and L. Rothenburg. Observations on stress-force-fabric relationships in idealized granular materials. *Mechanics of Materials*, 9(1):65 – 80, 1990.
- [7] R. J. Bathurst and L. Rothenburg. Investigation of micromechanical features of idealized granular assemblies using dem. *Engineering Computations*, 9(2):199–210, 1992.
- [8] R.J. Bathurst and L. Rothenburg. Micromechanical aspects of isotropic granular assemblies with linear contact interactions. *ASME Journal of Applied Mechanics*, 55:17–23, 1988.
- [9] R.J. Bathurst and L. Rothenburg. Note on a random isotropic granular material with negative Poisson’s ratio. *Int. J. Engng Sci.*, 26:373–383, 1988.
- [10] Burman B.C. *A mechanical approach to the mechanics of discontinua*. PhD thesis, James Cook University of North Queensland, Townsville, Australia, 1971.

- [11] T. Belytschko, P. Smolinski, and W.K. Liu. Stability of multi-time step partitioned integrators for the first order finite element systems. *Comput. Meth. Appl. Mech. Eng.*, 49:281–297, 1985.
- [12] V.F. Bondareva. On the effect of an axisymmetric normal loading on an elastic sphere. *Journal of Applied Mathematics and Mechanics*, 33(6):1001 – 1005, 1969.
- [13] Allan F. Bower. *Applied Mechanics of Solids*. Taylor & Francis, Boca Raton, FL, 2009.
- [14] N. Brodu, J. A. Dijksman, and R. P. Behringer. Multiple-contact discrete-element model for simulating dense granular media. *Phys. Rev. E*, 91:032201, Mar 2015.
- [15] Y.F. Cheng, S.J. Guo, and H.Y. Lai. Dynamic simulation of random packing of spherical particles. *Powder Technology*, 107(1):123 – 130, 2000.
- [16] N. Cho, C.D. Martin, and D.C. Segol. A clumped particle model for rock. *International Journal of Rock Mechanics and Mining Sciences*, 44(7):997 – 1010, 2007.
- [17] P. W. Cleary and M. L. Sawley. DEM modelling of industrial granular flows: 3D case studies and the effect of particle shape on hopper discharge. *Applied Mathematical Modelling*, 26(2):89 – 111, 2002.
- [18] P.A. Cundall. A Computer Model for Simulating Progressive Large Scale Movements in Blocky Rock Systems. In *Proc. Int. Symp. Rock Fracture, ISRM*, pages 2–8, Nancy, France, 1971.
- [19] P.A. Cundall. A computer model for simulating progressive large scale movements in blocky rock systems. In: *Proceedings of the Symposium of International Society of Rock Mechanics. Paper No. II-8*, 1, 1971.
- [20] P.A. Cundall. *UDEC: a generalized distinct element program for modeling jointed rock*. Report PCAR-1-80, US Army, European Research Office, London, 1980.
- [21] P.A. Cundall. Distinct element models of rock and soil structure. In *Analytical and computational models in engineering and rock mechanics*. Allen&Unwin, London, 1987.
- [22] P.A. Cundall. Formulation of a three-dimensional distinct element method – Part I: A scheme to detect and represent contacts in a system composed of many polyhedral blocks. *Int. J. Rock Mech. Min. Sci.*, 25:107–116, 1988.

- [23] P.A. Cundall. Formulation of a Three Dimensional Distinct Element Model — Part I. A Scheme to Detect and Represent Contacts in a System of Many Polyhedral Blocks. *Int. J. Rock Mech., Min. Sci. & Geomech. Abstr.*, 25(3):107–116, 1988.
- [24] P.A. Cundall and R. Hart. Numerical modeling of discontinua. *J. Eng. Comp.*, 9:101–113, 1992.
- [25] P.A. Cundall, T. Maini, J. Marti, P.J. Beresford, N.C. Last, and M.I. Asgian. *Computer Modeling of Jointed Rock Masses*. U.S. Army Engineers Waterways Experiment Station, Technical Report N-78-4, 1978.
- [26] P.A. Cundall and O.D.L. Strack. The development of constitutive laws for soil using the distinct element method. In W. Wittke, editor, *Numerical methods in geomechanics*, pages 289–298, Rotterdam, 1979. Balkema.
- [27] P.A. Cundall and O.D.L. Strack. A discrete numerical method for granular assemblies. *Geotechnique*, 29:47–65, 1979.
- [28] P.A. Cundall and O.D.L. Strack. The title of the work. Technical report, The distinct element method as a tool for research. Report to NSF concerning grant ENG76-20711, Department of Civil and Mineral Engineering, University of Minnesota, Minneapolis, USA, 1979.
- [29] P.A. Cundall and O.D.L. Strack. The title of the work. Technical report, The distinct element method as a tool for research in Granular media. Report to NSF concerning grant ENG76-20711, Part 2, Department of Civil and Mineral Engineering, University of Minnesota, Minneapolis, USA, 1979.
- [30] P.A. Cundall and O.D.L. Strack. Modeling of microscopic mechanics in granular material. *Mechanics of Granular Materials: New Models and Constitutive Relations*. Elsevier, Jenkins J.T., Satake M. (Eds.), pages 113—149, Amsterdam, 1982.
- [31] Rocky DEM. *Rocky version 4*. Engineering Simulation and Scientific Software, Houston, USA, 2019.
- [32] DEMpack. Discrete/finite element simulation software, CIMNE, Barcelona, Spain.
- [33] M. Dosta, C. Costa, and H. Al-Qureshi. Numerical investigation of compaction of deformable particles with bonded-particle model. *EPJ Web Conf.*, 140:15021, 2017.
- [34] EDEM. *EDEM 2019 release*. DEM Solutions Ltd., Edinburgh, UK, 2019.

- [35] A. Fakhimi and T. Villegas. Application of dimensional analysis in calibration of a discrete element model for rock deformation and fracture. *Rock Mechanics and Rock Engng.*, 40(2):193–211, 2007.
- [36] Y.T. Feng, K. Han, and D.R.J. Owen. Discrete thermal element modelling of heat conduction in particle systems: Pipe-network model and transient analysis. *Powder Technology*, 193:248–256, 2009.
- [37] Y.T. Feng and D.R.J. Owen. A 2d polygon/polygon contact model: algorithmic aspects. *Engineering Computations*, 21(2/3/4):265–277, 2004.
- [38] F. Fleissner, T. Gaugele, and P. Eberhard. Applications of the discrete element method in mechanical engineering. *Multibody Syst. Dyn.*, 18:81–94, 2007.
- [39] J. Fortin, O. Millet, and G. de Saxcé. Numerical simulation of granular materials by an improved discrete element method. *Int. J. Num. Meth. Eng.*, 62:639–663, 2004.
- [40] S. Geer, M. L. Bernhardt-Barry, E. J. Garboczi, J. Whiting, and A. Donmez. A more efficient method for calibrating discrete element method parameters for simulations of metallic powder used in additive manufacturing. *Granular Matter*, 20(4):77, Oct 2018.
- [41] H. Gercek. Poisson’s ratio values for rocks. *International Journal of Rock Mechanics and Mining Sciences*, 44(1):1 – 13, 2007.
- [42] D.T. Gethin, R.W. Lewis, and R.S. Ransing. A discrete deformable element approach for the compaction of powder systems. *Modelling and Simulation in Materials Science and Engineering*, 11:101–114, 2003.
- [43] J. Ghaboussi and R. Barbosa. Three-dimensional discrete element method for granular materials. *International Journal for Numerical and Analytical Methods in Geomechanics*, 14(7):451–472, 1990.
- [44] M. Gonzalez and A. M. Cuitino. A nonlocal contact formulation for confined granular systems. *Journal of the Mechanics and Physics of Solids*, 60(2):333 – 350, 2012.
- [45] P.K. Haff and B.T. Werner. Collisional interaction of a small number of confined inelastic grains. In T. Ariman and T. N. Veziroglu, editors, *Colloidal and Interfacial Phenomena*, pages 483–501. Hemisphere Publishing, 1987.

- [46] R. Hart, P.A. Cundall, and J. Lemos. Formulation of a three-dimensional distinct element method – Part II: Mechanical calculations for motion and interaction of a system composed of many polyhedral blocks. *Int. J. Rock Mech. Min. Sci.*, 25:117–126, 1988.
- [47] B. Harthong, J.-F. J erier, P. Dor emus, D. Imbault, and F.-V. Donz e. Modeling of high-density compaction of granular materials by the Discrete Element Method. *Int. J. Solids and Structures*, 46:3357–3364, 2009.
- [48] M. Haustein, A. Gladkyy, and R. Schwarze. Discrete element modeling of deformable particles in yade. *SoftwareX*, 6:118 – 123, 2017.
- [49] C. Hogue. Shape representation and contact detection for discrete element simulations of arbitrary geometries. *Engineering Computations*, 15(3):374–390, 1998.
- [50] D.C. Hong and J.A. McLennan. Molecular dynamics simulations of hard sphere granular particles. *Phys. A: Stat. Mech. Applicat.*, 187:159–171, 1992.
- [51] J. Horabik, P. Parafiniuk, and M. Molenda. Stress profile in bulk of seeds in a shallow model silo as influenced by mobilisation of particle-particle and particle-wall friction: Experiments and dem simulations. *Powder Technology*, 327:320 – 334, 2018.
- [52] X. Hou, T. Ding, T. Chen, Y. Liu, M. Li, and Z. Deng. Constitutive properties of irregularly shaped lunar soil simulant particles. *Powder Technology*, 346:137 – 149, 2019.
- [53] H. Huang. *Discrete Element Modeling of Tool-Rock Interaction*. PhD thesis, University of Minnesota, 1999.
- [54] J. A. Issa and R. B. Nelson. Numerical analysis of micromechanical behaviour of granular materials. *Engineering Computations*, 9(2):211–223, 1992.
- [55] Itasca. *PFC version 6.0, General Purpose Distinct-Element Modeling Framework*. Itasca Consulting Group, Minneapolis, Minnesota, 2019.
- [56] R. P. Jensen, P. J. Bosscher, M. E. Plesha, and T. B. Edil. Dem simulation of granular media—structure interface: effects of surface roughness and particle shape. *International Journal for Numerical and Analytical Methods in Geomechanics*, 23(6):531–547, 1999.
- [57] J. Jerier, D. Imbault, F. Donze, and P. Doremus. A geometric algorithm based on tetrahedral meshes to generate a dense polydisperse sphere packing. *Granular Matter*, 11(1):43–52, 2009.

- [58] S. Ji. Discrete element modeling of ice loads on ship and offshore structures. In X. Li, Y. Feng, and G. Mustoe, editors, *Proceedings of the 7th International Conference on Discrete Element Methods*, pages 45–54, Singapore, 2017. Springer.
- [59] X. Jia and R.A. Williams. A packing algorithm for particles of arbitrary shapes. *Powder Technology*, 120(3):175 – 186, 2001.
- [60] F. Jin, Ch. Zhang, W. Hu, and J. Wang. 3D mode discrete element method: Elastic model. *International Journal of Rock Mechanics and Mining Sciences*, 48:59–66, 2011.
- [61] L. Jing. A review of techniques, advances and outstanding issues in numerical modelling for rock mechanics and rock engineering. *International Journal of Rock Mechanics and Mining Sciences*, 40(3):283 – 353, 2003.
- [62] W. S. Jodrey and E. M. Tory. Computer simulation of close random packing of equal spheres. *Phys. Rev. A*, 32:2347–2351, 1985.
- [63] N. Karajan, Z. Han, H. Teng, and J. Wang. On the Parameter Estimation for the Discrete-Element Method in LS-DYNA. In *Proceedings of the 13th International LS-DYNA Users Conference*, 2014.
- [64] N. Karanjgaokar. Evaluation of energy contributions using inter-particle forces in granular materials under impact loading. *Granular Matter*, 19(2):36, Apr 2017.
- [65] R. Kačianauskas, A. Maknickas, A. Kačeniauskas, D. Markauskas, and R. Balevičius. Parallel discrete element simulation of poly-dispersed granular material. *Advances in Engineering Software*, 41:52–63, 2010.
- [66] C.T. Kelly. *Iterative Methods for Linear and Nonlinear Equations*. SIAM, Philadelphia, 1995.
- [67] W. R. Ketterhagen, M. T. am Ende, and B. C. Hancock. Process modeling in the pharmaceutical industry using the discrete element method. *Journal of Pharmaceutical Sciences*, 98(2):442 – 470, 2009.
- [68] R. Kobyłka, M. Molenda, and J. Horabik. Loads on grain silo insert discs, cones, and cylinders: Experiment and dem analysis. *Powder Technology*, 343:521 – 532, 2019.
- [69] M. Kodam, J. Curtis, B. Hancock, and C. Wassgren. Discrete element method modeling of bi-convex pharmaceutical tablets: Contact detection algorithms and validation. *Chemical Engineering Science*, 69(1):587 – 601, 2012.

- [70] J. Kozicki, J. Tejchman, and Z. Mróz. Effect of grain roughness on strength, volume changes, elastic and dissipated energies during quasi-static homogeneous triaxial compression using DEM. *Granular Matter*, 14:457–468, 2012.
- [71] H. Kruggel-Emden, E. Simsek, S. Rickelt, S. Wirtz, and V. Scherer. Review and extension of normal force models for the discrete element method. *Powder Technology*, 171:157–173, 2007.
- [72] H. Kruggel-Emden, S. Wirtz, and V. Scherer. A study on tangential force laws applicable to the discrete element method (DEM) for materials with viscoelastic or plastic behavior. *Chemical Engineering Science*, 63:1523–1541, 2008.
- [73] N.P. Kruyt and L. Rothenburg. Micromechanical definition of strain tensor for granular materials. *ASME Journal of Applied Mechanics*, 118:706–711, 1996.
- [74] A. K. Kulchitsky, J. B. Johnson, D. M. Reeves, and A. Wilkinson. Discrete element method simulation of a boulder extraction from an asteroid. In *14th ASCE International Conference on Engineering, Science, Construction and Operations in Challenging Environments; 27-29 Oct. 2014; St. Louis, MO; United States*, 2014.
- [75] N. Kumar, S. Luding, and V. Magnanimo. Macroscopic model with anisotropy based on micro–macro information. *Acta Mechanica*, 225(8):2319–2343, 2014.
- [76] F. Kun and H.J. Herrmann. A study of fragmentation processes using a discrete element method. *Comput. Meth. Appl. Mech. Eng.*, 138:3–18, 1996.
- [77] S. Kuraoka and Bosscher P. Parallelization of the distinct element method. In J. Yan, editor, *Proc. 9th Int. Conf. on Computer Methods and Advances in Geomechanics*, pages 501–506, Rotterdam, 1997. Balkema.
- [78] C. Labra. Advances in the development of the discrete element method for excavation processes. *PhD thesis, Polytechnic University of Catalonia, Spain.*, 2012.
- [79] C.L. Liao, T.P. Chang, and D.H. Young. Stress-strain relationship for granular materials based on the hypothesis of best fit. *International Journal of Solids and Structures*, 34:4087–4100, 1997.
- [80] X. Lin and T.-T. Ng. A three-dimensional discrete element model using arrays of ellipsoids. *Géotechnique*, 47(2):319–329, 1997.
- [81] B. D. Lubachevsky and Frank H. Stillinger. Geometric properties of random disk packings. *Journal of Statistical Physics*, 60(5):561–583, 1990.

- [82] S. Luding. Micro-macro transition for anisotropic, frictional granular packings. *International Journal of Solids and Structures*, 41(21):5821–5836, 2004.
- [83] S. Luding. Contact models for very loose granular materials. In *Proc. IUTAM Symp. on Multiscale Problems in Multibody System Contacts*, pages 135–150, Stuttgart, February 20-23, 2006, 2007.
- [84] S. Luding. Cohesive, frictional powders: contact models for tension. *Granular Matter*, 10:235–246, 2008.
- [85] S. Luding, M. Latzel, W. Volk, S. Diebels, and H.J. Herrmann. From discrete element simulation to a continuum model. *Comput. Meth. Appl. Mech. Engrg.*, 191:21–28, 2001.
- [86] S. Luding, K. Manetsberger, and J. Müllers. A discrete model for long time sintering. *Journal of Mechanics and Physics of solids*, 53:455–491, 2005.
- [87] S. Luding and E. Perdahcıođlu. A local constitutive model with anisotropy for various homogeneous 2d biaxial deformation modes. *Chemie Ingenieur Technik*, 83(5):672–688, 2011.
- [88] N. Madan, J. Rojek, and S. Nosewicz. Convergence and stability analysis of the deformable discrete element method. *International Journal for Numerical Methods in Engineering*, 118(6):320–344.
- [89] B. Majidi. *Discrete Element Method Simulation of Packing and Rheological Properties of Coke and Coke/Pitch Mixtures*. PhD thesis, Université Laval, Québec, Canada, 2018.
- [90] C.L. Martin, D. Bouvard, and S. Shima. Study of particle rearrangement during powder compaction by the Discrete Element Method. *J. Mech. Phys. Solids*, 51:667–693, 2003.
- [91] C.L. Martin, L.C.R. Schneider, L. Olmos, and D. Bouvard. Discrete element modeling of metallic powder sintering. *Scripta Materialia*, 55:425–428, 2006.
- [92] J.C. Mathews and W. Wu. Model tests of silo discharge in a geotechnical centrifuge. *Powder Technology*, 293:3 – 14, 2016. Particle Modelling with the Discrete Element Method A success story of PARDEM ([www.pardem.eu](http://www.pardem.eu)).
- [93] H.G. Matuttis, S. Luding, and H.J. Herrmann. Discrete element simulations of dense packings and heaps made of spherical and non-spherical particles. *Powder Technology*, 109:278–292, 2000.

- [94] MercuryDPM. *version 0.11: Fast, flexible particle simulations*. University of Twente, Netherlands, 2019.
- [95] A. A. Mirghasemi, L. Rothenburg, and E. L. Matyas. Numerical simulations of assemblies of two-dimensional polygon-shaped particles and effects of confining pressure on shear strength. *Soils and Foundations*, 37(3):43–52, 1997.
- [96] M. Miyata, M. Nakagawa, and G. G. W. Mustoe. Finite elements. chapter Design Considerations of Rubble Rock Foundations Based on a Discrete Superquadric Particle Simulation Method, pages 213–218. Civil-Comp press, Edinburgh, UK, 2000.
- [97] J.J. Moreau. Some numerical methods in multibody dynamics: application to granular materials. *European Journal of Mechanics A/Solids*, 13:93–114, 1994.
- [98] O. Mouraille and S. Luding. Sound wave propagation in weakly polydisperse granular materials. *Ultrasonics*, 48(6):498 – 505, 2008. Selected Papers from ICU 2007.
- [99] A. Munjiza. *The Combined Finite–Discrete Element Method*. Wiley, 2004.
- [100] G.G.W. Mustoe. A generalized formation of the discrete element method. *Engineering Computations*, 9(2):181–190, 1992.
- [101] S. Nezamabadi, T. H. Nguyen, J. Delenne, and F. Radjai. Modeling soft granular materials. *Granular Matter*, 19(1):8, Nov 2016.
- [102] T. Ng. *Numerical simulation of granular soil under monotonic and cyclic loading: a particulate mechanics approach*. PhD thesis, Department of Civil Engineering, Rensselaer Polytechnic Institute, Troy, New York, 1989.
- [103] T.-T. Ng. Numerical simulations of granular soil using elliptical particles. *Computers and Geotechnics*, 16:153–169, 1994.
- [104] Z. Ning, R. Boerefijn, M. Ghadiri, and C. Thornton. Distinct element simulation of impact breakage of lactose agglomerates. *Advanced Powder Technology*, 8(1):15 – 37, 1997.
- [105] S. Nosewicz. *Discrete element modeling of powder metallurgy processes*. PhD thesis, Institute of Fundamental Technological Research, Polish Academy of Sciences, Warsaw, Poland, 2015.
- [106] S. Nosewicz, J. Rojek, K. Pietrzak, and M. Chmielewski. Viscoelastic discrete element model of powder sintering. *Powder Technology*, 246:157–168, 2013.

- [107] J. O’Donovan, E. Ibraim, C. O’Sullivan, S. Hamlin, D. Muir Wood, and G. Marketos. Micromechanics of seismic wave propagation in granular materials. *Granular Matter*, 18(3):56, Jun 2016.
- [108] J. O’Donovan, C. O’Sullivan, and G. Marketos. Two-dimensional discrete element modelling of bender element tests on an idealised granular material. *Granular Matter*, 14(6):733–747, Nov 2012.
- [109] C. O’Sullivan. *Particulate Discrete Element Modelling: A Geomechanics Perspective*. Taylor & Francis, 2011.
- [110] C. O’Sullivan and J.D. Bray. Selecting a suitable time step for discrete element simulations that use the central difference time integration scheme. *Engineering Computations*, 21:278–303, 2004.
- [111] C. O’Sullivan, J.D. Bray, and L. Cui. Experimental validation of particle-based discrete element methods. In *Proceedings of the GeoCongress, Georgia, Atlanta*, 2006.
- [112] M. Otsubo, C. O’Sullivan, and T. Shire. Empirical assessment of the critical time increment in explicit particulate discrete element method simulations. *Computers and Geotechnics*, 86:67–79, 2017.
- [113] J.P. Plassiard, N. Belheine, and F.V. Donze. A spherical discrete element model: calibration procedure and incremental response. *Granular Matter*, 11:293–306, 2009.
- [114] A. Podlozhnyuk, S. Pirker, and C. Kloss. Efficient implementation of superquadric particles in discrete element method within an open-source framework. *Computational Particle Mechanics*, 4(1):101–118, 2017.
- [115] D.O. Potyondy and P.A. Cundall. A bonded-particle model for rock. *Int. J. Rock Mech. Min. Sci.*, 41:1329–1364, 2004.
- [116] CFDEM Project. *LIGGGHTS v3.8.0: Open Source Discrete Element Method Particle Simulation Software*. DCS Computing, Linz, Austria, 2017.
- [117] C. Recarey, I. Pérez, R. Roselló, M. Muniz, E. Hernández, R. Giraldo, and E. Oñate. Advances in particle packing algorithms for generating the medium in the discrete element method. *Computer Methods in Applied Mechanics and Engineering*, 345:336 – 362, 2019.

- [118] D.C. Richardson, K.J. Walsh, N. Murdoch, and P. Michel. Numerical simulations of granular dynamics: I. Hard-sphere discrete element method and tests. *Icarus*, 212:427–437, 2011.
- [119] M. Robinson, M. Ramaioli, and S. Luding. Fluid–particle flow simulations using two-way-coupled mesoscale SPH–DEM and validation. *International Journal of Multiphase Flow*, 59:121–134, 2013.
- [120] J. Rojek. *Modelling and simulation of complex problems of nonlinear mechanics using the finite and discrete element methods (in Polish)*. PhD thesis, Institute of Fundamental Technological Research, Polish Academy of Sciences, Warsaw, Poland, 2007.
- [121] J. Rojek. *Contact Modeling in the Discrete Element Method*, pages 177–228. Springer International Publishing, Cham, 2018.
- [122] J. Rojek, G.F. Karlis, L.J. Malinowski, and G. Beer. Setting up virgin stress conditions in discrete element models. *Computers and Geotechnics*, 48:228–248, 2013.
- [123] J. Rojek, C. Labra, O. Su, and E. Oñate. Comparative study of different discrete element models and evaluation of equivalent micromechanical parameters. *Int. J. Solids and Structures*, 49:1497–1517, 2012.
- [124] J. Rojek, S. Nosewicz, K. Jurczak, M. Chmielewski, K. Bochenek, and K. Pietrzak. Discrete element simulation of powder compaction in cold uniaxial pressing with low pressure. *Computational Particle Mechanics*, 3(4):513–524, Nov 2016.
- [125] J. Rojek, E. Oñate, C. Labra, and H. Kargl. Discrete element simulation of rock cutting. *International Journal of Rock Mechanics and Mining Sciences*, 48(6):996–1010, 2011.
- [126] J. Rojek and E. Oñate. Multiscale analysis using a coupled discrete/finite element model. *Interaction and Multiscale Mechanics*, 1:1–31, 2007.
- [127] J. Rojek, A. Zubelewicz, N. Madan, and S. Nosewicz. The discrete element method with deformable particles. *International Journal for Numerical Methods in Engineering*, 114(8):828–860, 2018.
- [128] L. Rothenburg. *Micromechanics of idealized granular systems*. PhD thesis, Carleton University, Carleton, Canadian, 1981.
- [129] L. Rothenburg and R. J. Bathurst. Micromechanical features of granular materials with planar elliptical particles. *Geotechnique*, 42 (1):79–95, 1992.

- [130] R.B. Runk, J.L. Stull, and O.L. Anderson. A laboratory linear analog for lattice dynamics. *American Journal of Physics*, 31:915–921, 1963.
- [131] M. H. Sadd, G. Adhikari, and F. Cardoso. DEM simulation of wave propagation in granular materials. *Powder Technology*, 109(1):222 – 233, 2000.
- [132] M. H. Sadd, Q. Tai, and A. Shukla. Contact law effects on wave propagation in particulate materials using distinct element modeling. *International Journal of Non-Linear Mechanics*, 28(2):251 – 265, 1993.
- [133] C. Salot, P. Gotteland, and P. Villard. Influence of relative density on granular materials behavior: Dem simulations of triaxial tests. *Granular Matter*, 11(4):221–236, 2009.
- [134] S. Saltzer. Numerical modelling of crustal scale faulting using the distinct element method. In *Proceedings of the 2nd International Conference on Discrete Element Methods(DEM)*, pages 511–522. IESL Publications, 1993.
- [135] W.I. Salvat, N.J. Mariani, G.F. Barreto, and O.M. Martínez. An algorithm to simulate packing structure in cylindrical containers. *Catalysis Today*, 107-108:513 – 519, 2005.
- [136] M. L. Sawley and P. W. Cleary. A parallel discrete element method for industrial granular flow simulations. *EPFL Supercomputing Review*, 11:23–29, 1999.
- [137] G.H. Shi. Discontinuous deformation analysis: A new numerical model for the statics and dynamics of deformable block structures. *Eng. Comp.*, 9:157–168, 1992.
- [138] S. Siiriä and J. Yliruusi. Particle packing simulations based on newtonian mechanics. *Powder Technology*, 174(3):82 – 92, 2007.
- [139] P. Stroeven and M. Stroeven. Assessment of packing characteristics by computer simulation. *Cement and Concrete Research*, 29(8):1201 – 1206, 1999.
- [140] H. Tao, W. Zhong, and B. Jin. Flow behavior of non-spherical particle flowing in hopper. *Frontiers in Energy*, 3:315–321, 2014.
- [141] L.E. Taylor and D.S. Preece. Simulation of blasting induced rock motion using spherical element model. *J. Eng. Computer*, 9:243–252, 1992.
- [142] C. Thornton and D. J. Barnes. Computer simulated deformation of compact granular assemblies. *Acta Mechanica*, 64(1):45–61, Dec 1986.

- [143] J.M. Ting. A robust algorithm for ellipse-based discrete elements modelling of granular materials. *Computers and Geotechnics*, 13:175–186, 1992.
- [144] J.M. Ting, M. Khwaja, L.R. Meachum, and J.D. Rowell. An ellipse-based discrete element model for granular materials. *International Journal for Numerical and Analytical Methods in Geomechanics*, 17:603–623, 1993.
- [145] B.C. Trent and L.G. Margolin. A numerical laboratory for granular solids. *Engineering Computations*, 9(2):191–197, 1992.
- [146] V. Vadluga and R. Kačianauskas. Numerical simulation of rupture and energy balance of 1D continuum by using discrete element method. *Mechanika*, 59:5–12, 2006.
- [147] M. J. Vold. The sediment volume in dilute dispersions of spherical particles. *The Journal of Physical Chemistry*, 64(11):1616–1619, 1960.
- [148] V. Šmilauer et al. *Yade Documentation 2nd ed.* The Yade Project, 2015. <http://yade-dem.org/doc/>.
- [149] T. L. Vu, S. Nezamabadi, J. Barés, and S. Mora. Analysis of dense packing of highly deformed grains. *EPJ Web Conf.*, 140:15031, 2017.
- [150] O.R. Walton. Explicit particle dynamics for granular materials. In *Proc. 4th Int. Conf. on Numerical Methods in Geomechanics*, pages 1261–1268, Eldmonton, Canada, 1982.
- [151] O.R. Walton. Particle dynamics calculations of shear flow. In J.T. Jenkins and M. Satake, editors, *Mechanics of Granular Materials: New Models and Constitutive Relations*, pages 327–338. Elsevier, 1983.
- [152] Y. Wang and P. Mora. *The ESyS\_Particle: A New 3-D Discrete Element Model with Single Particle Rotation*, pages 183–228. Springer, Berlin, Heidelberg, 2009.
- [153] L. Widuliński, J. Kozicki, and J. Tejchman. Numerical Simulations of Triaxial Test with Sand Using DEM. *Archives of Hydro-Engineering and Environmental Mechanics*, 56:149–171, 2009.
- [154] J. Wiącek, M. Molenda, and J. Horabik. *Mechanical Properties of granular agro-materials. Continuum and discrete approach.* Acta Agrophysica Rozprawy i Monografie EN, 2011.

- [155] J.R. Williams, G. Hocking, and G.G.W. Mustoe. The theoretical basis of the discrete element method. In *NUMETA 1985, Numerical Methods of Engineering, Theory and Applications*. A.A. Balkema, Rotterdam, 1985.
- [156] J.R. Williams and G.W. Mustoe. Modal methods for the analysis of discrete systems. *Computers and Geotechnics*, 4:1–19, 1987.
- [157] J.R. Williams and R. O’Connor. A linear complexity intersection algorithm for discrete element simulation of arbitrary geometries. *Engineering Computations*, 12(2):185–201, 1995.
- [158] B. Yang, Y. Jiao, and S. Lei. A study on the effects of microparameters on macro-properties for specimens created by bonded particles. *Eng. Comput.*, 23(6):607–631, 2006.
- [159] B. Yao and Q. Chen. Investigation on zero-gravity behavior of particle dampers. *Journal of Vibration and Control*, 21(1):124–133, 2015.
- [160] J. Zhao and T. Shan. Coupled CFD-DEM simulation of fluid-particle interaction in geomechanics. *Powder Technology*, 239:248 – 258, 2013.
- [161] O.I. Zhupanska. Contact problem for elastic spheres: Applicability of the hertz theory to non-small contact areas. *International Journal of Engineering Science*, 49(7):576 – 588, 2011.
- [162] O.C. Zienkiewicz and R.C. Taylor. *The Finite Element Method*. Butterworth-Heinemann, London, fifth edition, 2000.
- [163] A. Zubelewicz. *A certain variant of the finite element method*. PhD thesis, Warsaw University of Technology, Faculty of Civil Engineering, 1980. (in Polish).
- [164] A. Zubelewicz and Z. Mroz. Numerical simulation of rock burst processes treated as problems of dynamic instability. *Rock Mechanics and Rock Engineering*, 16:253–274, 1983.